Dissertation
submitted to the
Combined Faculties for the Natural Sciences and for Mathematics
of the Ruperto-Carola University of Heidelberg, Germany
for the degree of
Doctor of Natural Sciences

Put forward by

Diplom-Physikerin	**Daniela Schmitt**
Born in	**Remagen, Germany**

Oral examination: October 29, 2014

Quantifying intrafraction organ motion and its impact on prostate and lung radiotherapy

Referees: **Prof. Dr. Uwe Oelfke**
Prof. Dr. Wolfgang Schlegel

Zusammenfassung

Während der Bestrahlung von Prostata- und Lungentumoren kann die intrafraktionelle Organbewegung erheblich sein. Wie sich diese Bewegung klinisch auf einzelne Patienten und Patientenkollektive auswirkt ist noch Gegenstand aktueller Forschung. In der vorliegenden Arbeit wurden für diesbezügliche Untersuchungen Echtzeitbewegungsdaten implantierter Transponder verwendet, die mittels eines elektromagnetischen Tumorortungssystems während zweier am dkfz durchgeführter klinischer Studien erhoben wurden. Für beide Tumorentitäten wurde zunächst die auftretende Bewegung charakterisiert und quantifiziert. Darauf aufbauend wurden für die Prostatabestrahlungen Untersuchungen zu den Auswirkungen dieser Bewegung auf Sicherheitssäume und eine experimentelle und rechnerbasierte Quantifizierung der dosimetrischen Konsequenzen für Patienten auf individueller Basis durchgeführt. In einer ersten klinischen Studie zur elektromagnetischen Tumorortung in der Lunge standen die Quantifizierung inter- und intrafraktioneller Veränderungen der Transpondergeometrie durch Atembewegung und Tumorschrumpfung im Mittelpunkt. Zusätzlich wurde die Korrelation zwischen interner Lungentumorbewegung und externer Brustkorbbewegung untersucht. Die Ergebnisse führen zu der Schlussfolgerung, dass eine Echtzeitüberwachung der internen Bewegung für beide Tumorentitäten notwendig ist, um eine Reaktion auf die Bewegung zu ermöglichen und so die resultierenden dosimetrischen Konsequenzen zu reduzieren, im Besonderen wenn eine hypofraktionierte Therapie durchgeführt wird. Für die Lungenpatienten ist es zusätzlich erforderlich die interne Tumor- und Transpondergeometrie mit Hilfe einer regelmäßigen Kontrollbildgebung zu überprüfen.

Abstract

It is well known, that intrafractional tumor motion can be remarkable in prostate and lung radiotherapy, but the clinical impact on single patients and patient populations is still under investigation. In this work, real-time motion data of implanted transponders gathered with an electromagnetic tumor tracking system during two clinical trials performed at dkfz was used for evaluations concerning this matter. For both tumor entities the occurring motion was characterized and quantified, first. Based on this data, investigations for prostate radiotherapy deal with implications of this motion on the size of safety margins and the experimental and computational quantification of dosimetric consequences for individual patients. In this first clinical trial on electromagnetic tumor tracking in lung, analyses focused on the quantification of inter- and intrafractional variations of the transponder geometry due to breathing motion and tumor shrinkage. Additionally, the correlation between internal measured lung tumor motion and external chest motion was assessed. According to our results, we conclude that real-time monitoring of the internal motion is necessary for both tumor entities to enable motion management reducing dosimetric consequences, in particular if a hypofractionated radiotherapy is applied. For lung patients it is additionally required to perform a regular control of internal tumor and transponder geometry through patient imaging.

Contents

1 Introduction

In radiotherapy, it is crucial to irradiate the pre-defined target volume, mostly a tumor, as precisely as possible. Firstly, to guarantee the curative effect of the therapy by irradiating the whole tumor with a sufficient radiation dose to kill all tumor cells. Secondly, to avoid side effects caused by the irradiation of healthy tissue and especially organs at risk that are in close proximity to the tumor.

In the last decade, many improvements in treatment planning algorithms and treatment delivery techniques have been made to enable the optimization and delivery of a tumor conformal dose distribution even for complex geometries, where e.g. the tumor surrounds healthy organs. These therapy options are for example intensity modulated radiation therapy (IMRT), arc therapy or radiotherapy with protons or heavy ions. Modern treatment devices can deliver these complex dose distributions containing steep dose gradients with an accuracy of approximately 1 mm in a phantom. However, expected changes in patient geometry during the irradiation (called intrafraction motion) and from day-to-day (called interfraction motion) cause the delivered dose distribution in a patient treatment to be different from planned. Furthermore, the definition of the clinical target volume is an additional source of uncertainty.

The detection, quantification and dosimetric consequences of inter- and intrafraction tumor motion are the topic of this thesis. Tumor motion can distort the delivered dose distribution mainly in two ways. Systematic shifts of the target volume lead to a shifted dose and random motion components induce a blurring of the applied dose distribution compared to the planned one. In general, there are two concepts of motion consideration in radiotherapy. Firstly, estimated motion, e.g. based on a similar patient population or on some motion data of the patient itself can be used during the treatment planning process. Secondly the treatment can be adapted during the treatment delivery process using current measured tumor position. The classic treatment planning based approach is to avoid an underdosage of the tumor by an enlargement of the high-dose volume, called margin concept. This method leads to an irradiation with therapeutic dose of some healthy tissue in the vicinity of the tumor, which can cause severe side effects. When an adaptive treatment approach is used, these margins can be reduced, but not omitted because of persisting sources of uncertainty.

The most widely used method of integration of current tumor position information in daily treatment delivery is the use of image guidance for patient positioning prior to each fraction. With this technique, e.g. realized by the acquisition of a cone beam computed tomography, most interfraction changes can be detected. The compensation possibilities range from direct repositioning of the patient to a replanning process, which will be available even online in the near future. More complex is the detection and management of intrafraction motion. An adaption of the treatment to intrafraction motion, like irradiation in a window of predefined

tumor positions only (called gating) or the active motion compensation either by moving the beam or the patient (called tracking) ideally need real-time information of tumor motion. This real-time information could be achieved via imaging methods as well, but these methods are often accompanied with an additional radiation dose to the patient or need a dedicated treatment device, like the MR-linac, which is still under development. To monitor breathing motion for the management of lung tumor motion, it is also common to use an external surrogate like chest motion to detect the current breathing phase. Treatment adaption using this external information has to rely on a stable relation between external motion and internal tumor motion, which is needed to check during the treatment, for example by frequent imaging. Another method for real-time monitoring of tumor motion without additional imaging dose providing sub-millimeter accuracy is electromagnetic tracking of implanted transponders, as used here.

Patient data from two clinical trials is used for the investigations in this thesis. Real-time motion data was obtained with the Calypso tumor tracking system by Varian Medical Systems Inc. for prostate patients in the first trial and for lung patients in the second one. For the prostate patients, the motion amount was quantified and two different evaluations were made based thereon: first, margins which would be sufficient to compensate this motion in different treatment scenarios were calculated using a population based approach. Second, a dose recalculation was made using the individual patient motion data together with the delivered treatment plans to evaluate the dosimetric consequences of the measured motion in combination with the dkfz margin concept. The lung trial was a multi-center trial organized by Varian for the clinical evaluation of newly developed lung transponders. The obtained data was used for quantification of motion amount and characterization of motion patterns to evaluate the potential of different motion management methods. The stability of the transponder geometry in lung tissue was evaluated on an intra- as well as on an interfractional basis to derive demands on the planned implantation geometry and the need of geometry checking during a course of treatment. Additionally, for three patients concurrent chest motion data could be collected and the correlation between internal transponder motion and external chest motion was investigated to evaluate for example phase shifts between the signals and inter- and intrafractional changes in correlation strength.

The thesis is organized as follows:

- **Chapter 2** gives an overview of the treatment procedure applied to the patient in photon radiotherapy and of tumor motion and its consequences. The chapter then focuses on a detailed description of motion detection and management methods in radiotherapy.
- **Chapter 3** presents the investigations made for intrafraction motion in prostate radiotherapy. The measured prostate motion is quantified and suitable margin sizes for different treatment scenarios are determined. Furthermore the dosimetric consequences of the found prostate motion is estimated. Three dose recalculation methods were tested, and after an experimental validation, one of it was applied to the patient data.
- **Chapter 4** deals with the new application of electromagnetic tracking in lung radiotherapy. Investigations on motion amount, reliability of transponder geometry and correlation between internal lung and external chest motion are presented.
- **Chapter 5** gives a conclusion on the obtained results.

Publications

In accordance with the rules of the combined faculties for the Natural Sciences and for Mathematics of the University of Heidelberg, parts of this thesis have been published and were presented at scientific conferences either as a talk or as a poster. The corresponding abstracts are the following:

Schmitt, D., Nill, S., Herfarth, K., Münter, M., Pfitzenmaier, J., Zabel-du Bois, A., Röder, F., Huber, P., and Oelfke, U. (2010). Assessment of IGRT strategies for prostate patient setup and the impact of intrafraction motion. *Radiother Oncol*, 96:452.

Schmitt, D., Nill, S., Herfarth, K., Münter, M., Pfitzenmaier, J., Zabel-du Bois, A., Röder, F., Huber, P., and Oelfke, U. (2010). Intrafraction organ motion during prostate radiotherapy: Quantitative correlation of treatment time and margin size. *Int J Radiat Oncol Biol Phys*, 78(3):752.

Schmitt, D., Nill, S., Röder, F., Herfarth, K., and Oelfke, U. (2012). Dosimetric consequences of intrafraction prostate motion: Comparison between phantom measurements and three different calculation methods. *Med Phys*, 39(6):3686.

Schmitt, D., Nill, S., Röder, F., Herfarth, K., and Oelfke, U. (2012). Dosimetrische Auswirkungen intrafraktioneller Prostatabewegung: Berechnung und Evaluation von Dosisverteilungen in bewegten Patientengeometrien. In *Abstractband der 43. Jahrestagung der DGMP*, pages 356 – 357.

Schmitt, D., Nill, S., Röder, F., Herth, F., and Oelfke, U. (2013). Quantification of intrafractional tumor motion in the upper lung using an electromagnetic tumor tracking system. *Med Phys*, 40(6):412.

Schmitt, D., Nill, S., Röder, F., Gompelmann, D., Herth, F., and Oelfke, U. (2013). Inter- and intrafractional changes in the geometry of implanted electromagnetic transponders in the upper lung. In *Abstractband der 44. Jahrestagung der DGMP*, pages 115 – 118.

2 The motion problem in high precision radiotherapy

The success of radiotherapy is dependent on the ability to deliver a sufficient amount of energy dose to the whole target region. This aim is restricted by the concurrent irradiation of healthy tissue, leading to side effects, in particular in organs at risk in the neighborhood of the target. Several techniques for treatment delivery as well as imaging and treatment planning were developed to achieve this goal. The first part of this chapter will give an overview with a focus on techniques, which are used for treatments analyzed in this thesis.

The effect of radiotherapy is based on the deposition of energy by ionizing radiation. This energy dose D is defined as the absorbed energy dE per irradiated mass dm ($D = \frac{dE}{dm}$). The ionizations can lead to DNA damage like double strand breaks and thereby to the death of irradiated cells. The organs at risk are protected against cell death by two aspects: first they are spared from radiation dose and second the radiation is delivered in several small parts (called fractions) over weeks in most cases. The latter technique, known as fractionation, uses the fact that healthy tissue has a larger ability to repair DNA damage, than tumor cells, so the healthy tissue can regenerate more between radiation fractions (Sauer, 2010).

Treating a patient with radiation will always contain the consideration of patient positioning and organ motion. In the treatment planning process, the tumor position within the patient is typically known from a computed tomography (CT) data set. Magnetic resonance imaging (MRI) and positron emission tomography (PET) can further be used for classification of the disease and for refinement of the tumor volume definition. Despite the use of all these imaging modalities, the definition of the target volume is one of the largest uncertainties in radiation therapy (Van de Steene et al., 2002; Rasch et al., 2005). Besides from that, this image data is only a snap-shot of the patient anatomy at the time of treatment planning. Even 4D-CT techniques for lung patients cover typically only a few breaths, to study the motion induced by breathing. The second part of this chapter describes causes of deviations between the actual treatment situation from this snap shot, their dosimetric consequences, as well as strategies to detect, avoid and compensate for them.

There are several types or radiation sources available for radiotherapy, providing different particles in various energy ranges, like electrons, photons, protons and heavy ions. All these particles have advantages and disadvantages regarding their use for patient treatment. In this thesis photon radiotherapy is considered only, as the vast majority of treatments worldwide are performed with photons.

2.1 The key components of modern radiotherapy

2.1.1 Imaging and treatment planning

After the clinical decision of performing a radiotherapy for a particular patient, image data of the patient has to be acquired for treatment planning. It is required that the patient setup in these images is as close as possible to the treatment setup. For example, this can be achieved by using the same positioning devices, like foot or arm rests. Additionally, these and other devices provide vital patient immobilization during image acquisition. The planning process itself, i.e. the optimization of treatment parameters like beam shapes and irradiation amount per beam and the dose calculation is done on a computed tomography (CT) data set. From the CT the spatial distribution of electron densities in the patient can be extracted, which is needed as basis for dose calculation as described in section 3.2.2.1. Depending on the tumor site additional magnetic resonance imaging (MRI) and/or positron emission tomography (PET) can be performed for better knowledge of the tumor position, volume, stage or affected lymph nodes. Thereby the MRI can provide morphological information because of the better soft tissue contrast in comparison to a CT while functional MRI and PET can provide biological information such as tumor metabolism.

For tumors moving with respiration, especially lung tumors, it is common to acquire an additional 4D CT data set (Vedam et al., 2003; Keall et al., 2004). During this acquisition the external breathing motion is detected and recorded, for example using a chest belt, see section 2.2.2.3. This external signal is analyzed regarding the periodic breathing cycle. After that the complete CT data set is binned according to the breathing cycle phase in which it is acquired. From this sampled data up to 10 CT image sets each representing a single breathing phase are reconstructed. This can be done using a time (phase) or an amplitude binning of the data. The first method assigns the breathing phase according to the percentage of whole cycle time, that has elapsed until the start of the current cycle. The second one uses the amplitude of the external signal for phase assigning. If this is done relative to the maximum amplitude of each breathing cycle, it can have advantages in comparison to the phase binning for complex breathing patterns (Wink et al., 2006).

For dose prescription and calculation, different volumes have to be delineated in the planning CT (ICRU, 1993). Considering MRI and PET information, if available, the gross tumor volume (GTV) is defined as the visible tumor. A larger volume around the GTV, called clinical target volume (CTV) is delineated based on knowledge of tumor site specific microscopic tumor infiltration into the healthy tissue. In radiotherapy of lung tumors the CTV is often replaced by an ITV (internal target volume (ICRU, 1999)). This ITV is commonly created by a fusion of all CTVs determined in all phases of the planning 4D CT, so it already contains the respiratory induced motion, that was present during the planning CT. Depending on tumor site and treatment delivery technique additional larger volumes around the CTV or ITV, called planning target volume (PTV), can be defined to account for tumor motion and other geometrical uncertainties in the dose calculation or delivery. A deeper introduction to these margin concepts is given in section 2.2.3.2.

After the delineation of the organs at risk different dose levels have to be specified. Depending on the tumor site a specific dose is prescribed to the target volume and maximum doses for the healthy organs are defined. At this point a treatment planning program is

used for dose calculation and optimization of beam parameters, while conforming to the predetermined normal tissue dose constraints and PTV prescription dose as much as possible. The optimization can be performed by manually adapting beam shapes and weights for conventional 3D conformal therapy (3D-CRT) or by an inverse optimization software via user defined constraints and penalty factors weighting deviations between calculated and prescribed dose distribution for intensity modulated radiotherapy (IMRT), see (Bortfeld and Thieke, 2006).

For a description of radiotherapy planning for different tumor sites see (Barrett et al., 2009).

2.1.2 Dose delivery

All patient treatments considered in this thesis are performed with the same treatment device, but with two different techniques of beam delivery. This section gives a short introduction in the generation of irradiation, the used coordinate system and beam delivery geometry. Details of the performed treatments can be found in sections 3.2.1 and 4.2.1 for prostate and lung patients, respectively.

2.1.2.1 Treatment device

All patient treatments analyzed in this thesis as well as the experiments are performed with a Siemens Artiste treatment device, equipped with a 160 MLC (Siemens AG, Munich, Germany). The main components and geometrical aspects of a medical linear electron accelerator can be seen in fig. 2.1(a). For all applications used in this work, electrons are accelerated to an energy of 6 MeV. These electrons are then directed to a target made of tungsten, where bremsstrahlung and characteristic X-ray radiation is produced. To form a radiation field with homogeneous fluence, the spatial fluence distribution is then flattened by the transition of a flattening filter, which is mainly a cone-shaped piece of tungsten. The resulting photon spectrum has a maximum energy of 6 MeV and a mean energy of about 2 MeV, depending on the distance from the central beam axis (Sheikh-Bagheri and Rogers, 2002; Faddegon et al., 2004). The beam aperture is then formed by a multi leaf collimator (MLC), made of tungsten as well. To create a large number of possible beam directions relative to the patient, the whole linear accelerator gantry can be rotated around the patient and the patient couch can be rotated around the vertical room axis corresponding to the central axis of a vertical beam. The point were the rotation axes intersect is called isocenter of the treatment machine, see fig. 2.1(a). The beam source-to-isocenter distance is 1 m. The maximum size of the irradiation field is $40 \times 40\,\mathrm{cm}^2$ in the isocentric distance. The 160 leafs of the MLC are arranged in opposing pairs, while each leaf pair can block a radiation stripe with a width of 0.5 cm in the isocentric plane.

All descriptions and results presented in this thesis use the IEC-61217 coordinate system. The axes are shown in fig. 2.1(b). In general the three terms lateral, longitudinal and vertical direction are used. They are always according to a patient lying on the treatment couch on his back with the head near the gantry, this position is called ‘head first supine’ (HFS).

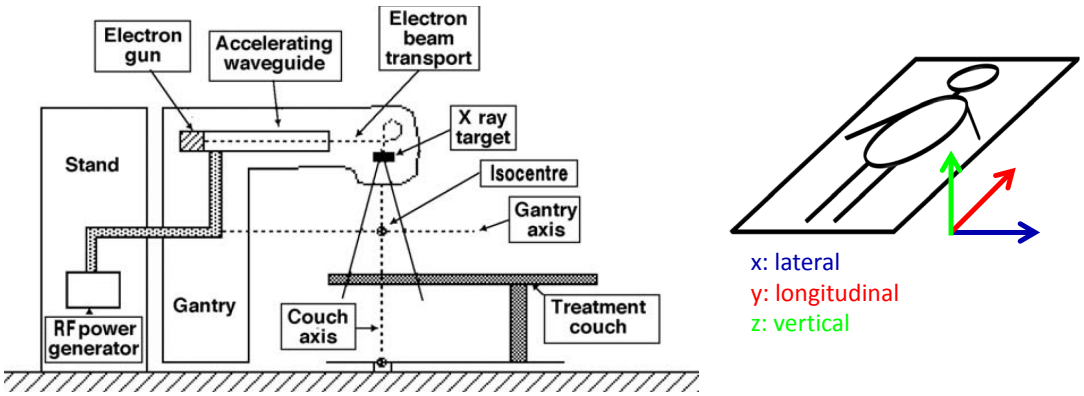

(a) (b)

Figure 2.1: (a) Scheme of a medical electron linear accelerator in photon irradiation mode, taken from (Podgorsak and International Atomic Energy Agency, 2005) (b) Draft of the used coordinate system IEC 61217, the point of origin is the isocenter.

2.1.2.2 Dose delivery techniques

The mechanical abilities of the treatment machine can be used in different ways to reach an optimal dose coverage of the target with concurrent sparing of the organs at risk. They differ in the workload and time for therapy planning and delivery. The technique is chosen due to the tumor site and geometrical properties of the patient anatomy. All treatments analyzed in this thesis are performed either as a 3D conformal or a step-and-shoot intensity modulated radiation therapy.

- **3D conformal radiation therapy (3D-CRT):**

  Performing three-dimensional conformal radiotherapy is a very intuitive way of irradiating a target volume. Initially, for each beam the aperture formed by the MLC is defined as the projection of the target shape to this beam angle. Then an adjustment to the beam shapes and weights and dose per beam is either manually or automatically optimized. The radiation delivery is organized as follows: for each beam the gantry moves to the planned position, the MLC forms the aperture, the radiation is delivered and the gantry moves to the next beam angle.

- **Step-and-shoot intensity modulated radiation therapy (SNS-IMRT):**

  The main difference to 3D-CRT is the substitution of a flat fluence distribution per beam by a heterogeneous fluence modulated beam, called an 'intensity modulated' beam. This is achieved by consecutive application of overlapping beam apertures formed by the MLC. Each one of these beam apertures is called an IMRT segment, while the whole irradiation amount from one beam angle is called a radiation field. The fluence pattern for each beam is thereby optimized using an inverse treatment planning software. The possibility to form complex fluence profiles per beam can lead to a more conformal tumor dose while sparing of organs at risk for complex patient geometries compared to 3D-CRT. In particular, the opportunity to form concave dose

distributions can be important e.g. in the treatment of tumors in the brain or spinal region. For a review on IMRT see (Bortfeld, 2006).

In a clinical setting, it is common for both techniques to manually select the number of beams and the gantry angles while considering the geometry of target volume and organs at risk. There are up to 10 beam angles defined, usually. For each part of radiation delivery of 3D-CRT and SNS-IMRT the beam angle and beam aperture are adjusted, before the beam is enabled, so there are no moving parts of the treatment device during actual irradiation. Obviously the duration of each treatment depends on the prescribed dose and the complexity of the patient case, leading to a different number of beams or IMRT segments. Typical fraction times from start of first beam to end of last beam including all gantry and MLC motion for the treatments analyzed in this thesis are about 5 min for 3D-CRT and about 10 min for SNS-IMRT.

2.2 Motion management in radiotherapy

2.2.1 Organ motion and its dosimetric impact

2.2.1.1 Motion types

In the vast majority of cases, a radiotherapy treatment is fractionated into several irradiations on different days. Depending on the tumor site and tumor stage, different fractionation schemes can be applied. Standard fractionation schemes often contain 30 to 35 fractions typically given over six to seven weeks, five times a week. Most treatments analyzed in this thesis are fractionated this way. Another fractionation scheme occurring in this thesis is the hyofractionation, where less fractions with higher fraction doses are prescribed. The hypofractionated treatments here are given in 10 fractions, 5 times a week. All these fractionation schemes lead to two different types of deviations from the situation, which was present at the time of treatment planning. These different types are called interfraction and intrafraction motion, described in the following:

- **Interfraction motion** summarizes all geometric deviations from fraction to fraction. This contains an inaccurate positioning of the whole patient with respect to the radiation source, as well as internal anatomy changes. These changes can appear due to physiological processes like digestion (e.g. different filling of digestive organs) or as response to the therapy, such as tumor shrinkage or a decrease of body-fat volume.

- **Intrafraction motion** is the motion occurring during one treatment fraction, typically lasting 5 min to 15 min. Intrafraction motion is mostly caused by organ motion on a short time scale like breathing or digestion. Digestion for example can lead to a changing bladder or colon filling. In addition, there can be motion due to different muscle tense of the patient, e.g. a continuous relaxation with increasing treatment time.

(a) Systematic (b) Random

Figure 2.2: Schematic of dosimetric consequences of systematic (a) and random (b) errors in radiotherapy treatments. For simplification, the static case is defined as a circular shaped target region (black circle) covered by a perfect fitting homogenous dose (blue area), shown on the left side of each figure. Assuming a systematic 2-dimensional shift of the actual relative to the planned target region, the dose distribution will be shifted and parts of the target will be not irradiated while some healthy structures are irradiated with the therapeutic dose (a). If an equally distributed 2-dimensional random displacement of the target is considered, there will be an inner region of the target getting the planned dose, while in the outer region the dose will decrease continuously leading to an underdosage of the tumor edge and an overdosage in the healthy vicinity of the target (b).

2.2.1.2 Motion effects on delivered dose distributions

Inter- and intrafractional motion can cause large deviations between the planned and the delivered dose distribution. Both motion types can have random and systematic components leading to different effects on the dose distribution as can be seen in fig. 2.2. In the following, the circumstances and dosimetric consequences of these permanent or temporary errors of geometric relation between irradiation field and target volume are described for the case of no motion management. The terminology follows (van Herk et al., 2000).

- **Systematic errors**

  Systematic errors are usually defined as errors due to inaccuracies in treatment preparation, e.g. in target definition or selection of landmarks for patient positioning. They are called systematic when they have the same influence on every fraction of the treatment for one single patient, while they are different for two patients. These errors cause a shift of the dose distribution, as can be seen in fig. 2.2(a). Intrafraction motion can have a systematic component as well, for example a continuous drift during the irradiation, if this drift is always towards the same direction.

- **Random errors**

  Random positioning errors and motion lead to a blurred dose distribution, as depicted in fig. 2.2(b). They are usually defined as inaccuracies in treatment execution differing from fraction to fraction, like errors in patient positioning on a day-to-day basis or random intrafraction motion.

These definitions are for a whole course of radiotherapy containing several fractions. Random positioning errors convert into systematic errors, when only single fractions are evaluated. There can be systematic errors leading to equal effects in all patients as well, like misalignment of the coordinate systems of the CT scanner and the therapy device. They are not considered here, because they can be detected and avoided by quality assurance measurements.

The methods to calculate dosimetric consequences using given patient motion data and clinical dose distributions in this thesis are presented in section 3.2.2.2.

2.2.2 Motion detection methods

There are various techniques for patient positioning and monitoring of inter- and intrafractional motion. All these techniques have advantages and drawbacks associated with the characteristics of acquired data and additional risks for the patients. The methods can be categorized by the type of provided motion information in: I) image guidance, II) electromagnetic detection of internal markers and III) detection of external surrogate motion. This section gives an overview of these methods with a detailed description of the specific techniques used in this thesis.

2.2.2.1 Image guidance

The most widely used application of image guided radiotherapy (IGRT) is the patient positioning prior to each fraction. Established methods using the MV treatment beam with a flat panel detector on the opposing side of the patient are 2D portal imaging (Hurkmans et al., 2001) and megavoltage cone beam CT (MV CBCT) (Pouliot et al., 2005). For better soft tissue contrast, kV X-ray imaging can be performed with one or more X-ray sources and associated flat panel detectors mounted on the linac gantry itself or elsewhere in the treatment room. 3D information can thereby be extracted from concurrent 2D imaging with at least two source-detector combinations (Fu and Kuduvalli, 2008; Jin et al., 2008), or a kilovoltage cone beam CT can be acquired with a linac mounted system (Jaffray et al., 2002). Using dedicated software tools, an estimation of 3D translations and rotations of the prostate can be made even from 2D projections of a single KV source, (Poulsen et al., 2008; Tehrani et al., 2013). Image guidance without additional imaging dose to the patient is possible using ultra sound or MRI. Established methods are an ultra sound probe for 2D-imaging (Lattanzi et al., 2000) and a combination of 2D imaging with infrared based tracking of the probe, leading to information in 3D (Johnston et al., 2008). Treatment machines with an integrated MRI are now available for irradiation with photons from ^{60}Co decay (ViewRay, ViewRay Incorporated, Oakwood Village, Ohio), but still under development for photon therapy based on electron linear accelerators (Lagendijk et al., 2008; Fallone et al., 2009).

Some of these methods can be used for monitoring of intrafractional motion as well. The aforementioned 3D volumetric imaging with the treatment beam or a kV source (CBCT) needs a complete or at least half a rotation of the imaging system around the patient with rotation times around 1 min impeding the application during the therapy. Continuous MV portal imaging, which is the detection of the therapeutic radiation field behind the patient

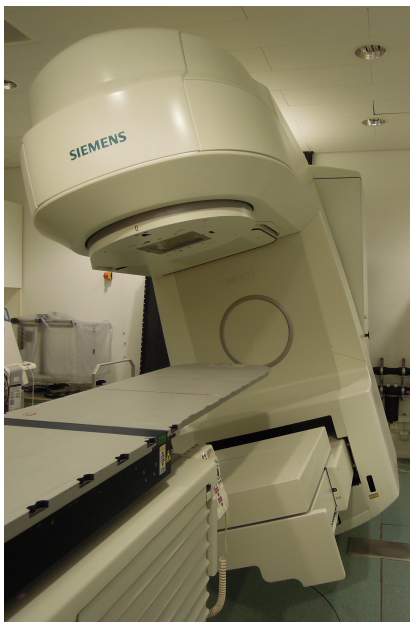

Figure 2.3: Photograph of the Siemens Artiste. The MV flat panel is extended and the gantry is slightly rotated. The treatment couch can be seen in the front.

and therefore not accompanied with additional dose, is able to monitor motion perpendicular to the beam direction, if fiducial markers are implanted (Berbeco et al., 2007), or even without markers for lung tumors (Rottmann et al., 2010). Combining two or more beam-detector combinations with different beam angels to a stereoscopic system, 3D-motion can be extracted, too (Berbeco et al., 2004), but with additional dose. An ultra sound probe can be used for continuous 2D imaging with the possibility of 3D motion estimation (Hsu et al., 2005), but stable acoustic coupling has to be guaranteed. A continuous full 3D imaging during irradiation is possible with an integrated MRI system as mentioned above.

Megavoltage cone beam CT (MV CBCT) In this thesis, MV CBCT data sets acquired for patient positioning prior to each fraction for all prostate patients are used. They are acquired with the Siemens Artiste treatment beam with a 6 MV photon spectrum, see section 2.1.2.1. Figure 2.3 shows the Siemens artiste with extended flat panel detector. The technique of acquiring a CT using a broad beam and a flat panel detector is called cone beam CT, because of the beam shape covering the whole imaged region in one rotation. The term 'cone beam CT' is in contrast to a conventional diagnostic CT which is called 'fan beam CT' because of a narrow beam and detector performing a spiral path with hundreds of rotations around the patient. To reduce scan time and hence motion artifacts, current developments in diagnostic CTs go towards broader beams and increasing number of detector rows as well as rising rotation speed (e.g. Aquilion One, Toshiba Corporation, Tokyo, Japan).

Imaging with the MV treatment beam leads to less soft tissue contrast in comparison to a kV X-ray source, which have typically mean photon energies below 100 keV. The tissue contrast in photon imaging methods is driven by tissue dependent attenuation of the beam, detected behind the patient. This attenuation can be described by the reduction in the photon beam intensity I behind a material of thickness d with a linear attenuation coefficient μ: $I(d) = I_0 \cdot e^{-\mu \cdot d}$, with the initial intensity I_0. The linear attenuation coefficient is the sum of the attenuation coefficients from all interaction types. In the energy ranges used here,

only the photo electric and the Compton effect have to be considered. In kV imaging the photoelectric effect is dominant, while in MV imaging the Compton effect is most important. This is mainly driven by the dependence of the photoelectric effect on the photon energy E_γ, namely $\mu_{\text{photo electric}} \propto 1/E_\gamma^3$. The contrast in the images is mainly achieved due to different atomic numbers Z of the tissues. For the photo electric effect the attenuation coefficient shows a strong dependence on Z ($\mu_{\text{photo electric}} \propto Z^{3 \text{ to } 4}$) while for the Compton effect this dependence is much weaker ($\mu_{\text{Compton}} \propto Z$). These conditions enable excellent opportunities for tissue differentiation in the human body for kV imaging, while in MV imaging their is nearly no soft tissue contrast. As a result patient positioning with an MV CBCT relies mainly on the bony anatomy, which can be distinguished from soft tissue due to a large Z difference, or on implanted fiducial markers, which are often made of gold.

2.2.2.2 Electromagnetic methods

Electromagnetic devices for patient positioning and motion monitoring deliver 3D position information with high update rates without imaging dose or the need of information extraction from image data. Two different systems are available, the Calypso Tumor Tracking System by Varian Medical Systems Inc., Palo Alto, CA and the RayPilot System by Micropos Medical AB, Gothenburg, Sweden (Shah et al., 2011b), while only the first is approved for clinical usage outside patient trials. Both systems are designed for reporting the coordinates of one special point in the patient over time. Thus, the main drawback of this technique is the absence of information about the current anatomic situation e.g. relative position of target and organs at risk or deformations of the target. Both systems work via an antenna array detecting resonant circuits within the patient. The main difference is the use of three implanted passive resonant circuits, which remain in the body after the therapy for the Calypso System and the use of one active cabled resonant circuit in a catheter, which is removed after the course of therapy for the RayPilot System. Both are developed for application in the prostate. But for the Calypso System removable skin transponders for fixation everywhere on the body were already approved for clinical use in the US and the EU and lung transponders are approved for clinical use in the EU and for investigational use in the US.

The Calypso System In this thesis, motion data detected by the Calypso System is used. This data was acquired for prostate and lung cancer patients during all treatment fractions. General system description follows the Calypso users manual (Calypso Medical Technologies, Inc., 2010a) and (Balter et al., 2005). Information about lung application refers to (Calypso Medical Technologies, Inc., 2010b).

A schematic of the device components can be seen in fig. 2.4, where a prostate case is shown. The only difference to lung application is the use of different transponders, called beacons. The transponders used for prostate implantation, shown in fig. 2.5(a), are implanted endorectally. The lung cancer patients get their transponders implanted bronchoscopically, a schematic of a lung beacon is shown in fig. 2.5(b). The electronic part of both beacon types is the same, but the lung beacons have a special capsule with nitinol legs, which are extended for fixation of the beacon in the specified air way close to or inside the tumor. This fixation capsule is necessary because smooth surface beacons show an insufficient fixation rate, see

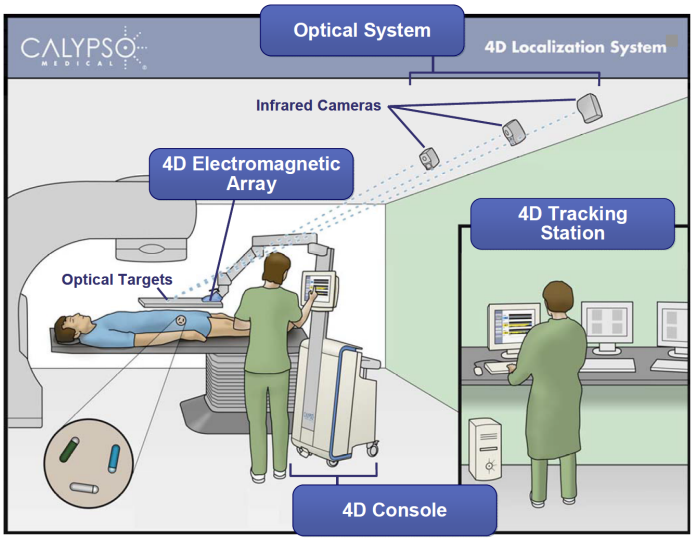

Figure 2.4: Overview of the components of the Calypso Tumor Tracking System, taken from (Calypso Medical Technologies, Inc., 2010b), with permission.

(Shah et al., 2013). The beacons are passive resonant circuits with three different resonance frequencies close to 300, 400 and 500 kHz, respectively. An antenna array is placed above the patient to localize the beacons in the patient. For this localization, the array is equipped with four source coils emitting electromagnetic waves with frequencies between 275 and 550 kHz consecutively and in periodic repetition. The beacons are excited corresponding to their individual resonance frequency. During periodic pauses of the exciting signal the frequency and strength of each beacon's emission is detected by 32 receiver coils placed all over the array for determining the individual beacon position relative to the array. We used the Calypso System version 2.0 in which each individual beacon is detected approximately every 300 ms. From these positions, the beacon centroid position is calculated and updated every 100 ms, when a new beacon position is known. The mobile array has nine active infrared markers integrated in its surface. They are tracked with infrared cameras, mounted permanently on the ceiling of the treatment room. Because of this combination, the position of the beacons and the beacon centroid relative to the fixed coordinate system of the treatment room is known.

During the treatment planning process, the planning CT is used to define the position of the treatment isocenter inside the patient and to read out the coordinates of the implanted beacons relative to it. This information is then transferred to the Calypso System. During the treatment fractions, the deviation between actual and planned position for only one point inside the patient is shown on the tracking station monitor and can be used for motion management. The geometry of the beacons and the defined isocenter constitutes this point and thereby the localization mode in which the system is operating. There are two localization modes, the centroid mode and the isocentric mode. Depending on the special beacon geometry in each patient, a maximum distance between the isocenter and the beacon centroid is allowed for the use of isocentric localization. If this distance is exceeded, the centroid mode is chosen and the displayed distance refer to the centroid's actual and planned position. Otherwise, the isocentric mode is chosen and the measured centroid

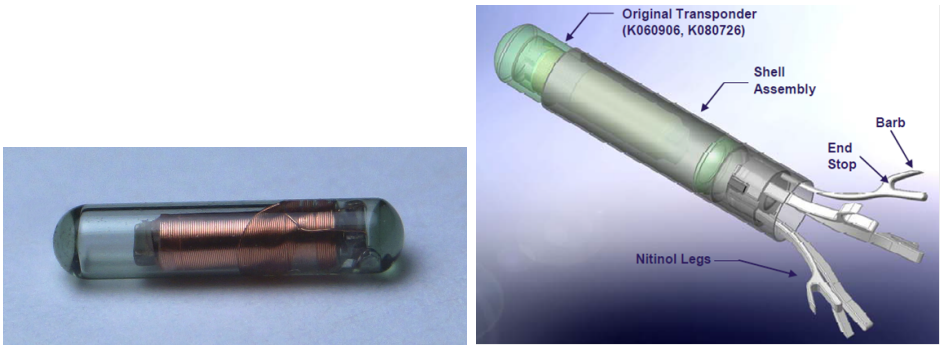

(a) (b)

Figure 2.5: Photograph of a transponder as used for the prostate patients: length 8 mm, diameter 1.85 mm (a). Draft of an encapsulated transponder for use in lung patients: length with legs 14 mm, diameter with retracted legs 2 mm and with extended legs 5.5 mm. Taken from (Calypso Medical Technologies, Inc., 2010b), with permission. (b)

deviation is converted into a deviation of the current and planned isocenter position. These two deviations are not identical, when rotations between the current and planned patient geometry occur. In such a situation, a determined translation is correct for the center of rotation defined by the coordinate system, only. This center of rotation is the beacon centroid. Considering the rotation angles around all three axes, measured in the beginning of each fraction, the centroid deviation can be converted into an isocentric deviation. This conversion assumes a rigid body, due to that it is done for small distances between beacon centroid and isocenter, only. The localization mode is relevant for some investigations presented in this thesis, there it will be referred to it, elsewhere the used term will be simply 'prostate motion' or 'target motion'.

The Calypso System is equipped with a detector, measuring scattered radiation outside the treatment field. The beam status (on or off) is measured with 10 Hz update rate, corresponding to the displayed target motion. For further analysis, all data is stored with a time stamp, including the beam status and the individual beacon positions.

The accuracy of the Calypso System in clinical use is declared as sub millimeter by the manufacturer (Calypso Medical Technologies, Inc., 2010a) for a localization volume beginning 8 cm below the array with 14 cm width and length and 19 cm height. Evaluations in air and saline results in an accuracy (distance from predefined position) of < 0.2 mm for the whole volume, while the reproducibility (read out stability) was very dependent on the vertical beacon-array distance with values up to 0.01 mm for a distance of 8 cm at the upper border of the localization volume and up to 0.62 mm in 27 cm distance at the lower border of the localization volume (Balter et al., 2005). Because of that the volume declared as usable for intrafraction motion monitoring is 14 cm wide and long, but reaches from 8 cm beacon-array distance until 21 cm, only.

In cooperation with the junior group computer assisted interventions at the dkfz, we performed measurements of the precision and accuracy of our Calypso System using a standardized protocol, which is designed for electromagnetic tracking devices used in computer

assisted surgery. The precision (root mean square of 150 adjacent data points without motion) ranges from 0.3 mm to 0.8 mm for distances between array and beacon centroid of 11 cm and 21 cm. The accuracy of the measurement of fixed 5 cm distances in horizontal planes was determined to (0.1 ± 0.1) mm for all array–beacon centroid distances. This evaluation is accepted for publication in the Journal of *Physics in Medicine and Biology* (Franz et al., 2014).

A drawback of the marker implantation besides the general risk of surgery is although the transponders are MRI safe, they are not MRI compatible. Meaning that there are no safety constraints on MR imaging after implantation, but the beacons cause artifacts in the surrounding tissue. The size of these artifacts depends on the applied MRI sequence with radii up to 1.5 cm and lengths up to 4 cm, which makes MRI unavailable for follow-up care, see (Zhu et al., 2009) analyzing 1.5 T and 3 T MRI.

2.2.2.3 External surrogates

The essential drawback of all external surrogate methods is monitoring not of the tumor itself, but of an external patient parameter, assumed to be representative for the tumor position. The correlation between the surrogate and the tumor position is usually known from the treatment planning CT. The general problem of all these methods is the question of robustness of this correlation over time from the day of planning CT to the days of treatment and during one fraction. Depending on the motion management strategy, which will be based on the surrogate measurement, it is necessary to check the correlation model by acquisition of imaging data with different time intervals. The advantage of all external surrogate methods is the avoidance of additional risk for the patient due to the data acquisition, because of the absence (or reduction) of imaging dose and invasive marker implantation.

The most widely used method is based on drawn marks on the patient's skin. For the classic technique of patient positioning prior to treatment these marks are aligned with the laser coordinate system of the treatment machine and this is commonly also done for advanced positioning methods as approximate pre-positioning. Surrogate methods can also be used for real-time monitoring of motion during the irradiation. For example infrared markers on the patients skin or optical LEDs on a tight vest can be detected continuously by cameras (ExacTrac, Brainlab AG, Feldkirchen, Germany and Synchrony Respiratory Tracking System, Accuray, Sunnyvale, CA, USA). Another method uses a scanning laser line for acquisition of a patient surface model (Sentinel, C-RAD AB, Uppsala, Sweden). For the investigations presented in this thesis one external surrogate motion monitoring system is used, the Anzai belt, which is a part of the Anzai Respiratory Gating System AZ-733V (Anzai Medical Co., Ltd, Tokyo, Japan).

The Anzai Respiratory Gating System The Anzai Respiratory Gating System is designed for motion detection and management in radiotherapy of tumors moving accordingly to breathing. The device performing the surrogate measurement is called the Anzai belt. It contains a pressure sensor and gets wrapped around the patients abdomen or chest thereby measuring the relative changes in abdomen or chest circumference due to breathing. The sensor delivers data with an update rate of 40 Hz to a PC via signal processing hardware.

Using the dedicated software, the periodic signal of in- and exhalation can be displayed and used on the PC. From a planning 4D-CT, during which the Anzai belt was used for binning of the CT reconstruction phases (see section 2.1.1), the correlation between internal tumor motion and external breathing signal is determined. The assumption that this correlation is still valid in all treatment fractions can lead to large discrepancies between predicted tumor position from external signal and actual tumor position, hence the correlation should be reviewed on a regular basis. The system is designed to use the external breathing signal for a motion management technique called 'gating' described in section 2.2.3.4 through a connection between the PC and the control software of the treatment machine. In this work, it is used for acquiring 4D CT data sets of the lung patients and for measurement of external breathing signal during radiation therapy for 3 lung patients.

2.2.3 Motion management strategies

There are various methods to deal with inter- and intrafraction motion in radiation therapy, differing in effort and required extra devices. The classical techniques cover motion prevention strategies and concepts for enlargement of the treated volume to encompass positioning errors or intrafraction motion (treatment margins). Another possibility is the inclusion of probability distributions of target position directly into the optimization process (probabilistic planning). More sophisticated methods that require frequent imaging or real-time motion information are frequent repositioning, pursuit of the tumor motion with the treatment beam (tracking) or irradiation triggering based on a predefined position window of the tumor (gating).

2.2.3.1 Motion mitigation

The most intuitive way to prohibit the distortion of the planned dose distribution due to positioning errors and intrafractional motion is the avoidance of this motion. Multiple techniques are available for patient setup which are designed to guarantee reproducible patient positioning and immobilization. Examples are patient specific thermoplastic masks mounted on the treatment couch (Tryggestad et al., 2011) for treatments in the cranial and head and neck region, or a patient specific vacuum mattress (Nevinny-Stickel et al., 2004) for treatments in abdominal and pelvic region.

Other methods are the choice of treatment position or a dietary protocol for the patients, with the aim of reducing digestive motion (Smitsmans et al., 2008). For tumors moving with respiration several strategies are explored to reduce the tumor motion amplitude during radiotherapy. The most obvious way of motion reduction is to irradiate during breath hold. One way to ensure the breath hold is so called 'active breathing control' (ABC), see (Wong et al., 1999). Thereby the patient is connected to an adapted ventilator which controls the respiration. Using this ventilator a breath hold of the patient can be initiated and held by closing both valves, the patients are trained to tolerate this process prior to the therapy. Another method is the 'deep inspiration breath hold' (DIBH), see (Hanley et al., 1999; Rosenzweig et al., 2000). In this method the patients are coached to follow breathing commands for deep inhalation and breath hold. During the therapy the therapists give these commands and the patients respiration is monitored via spirometry. The deep inhalation

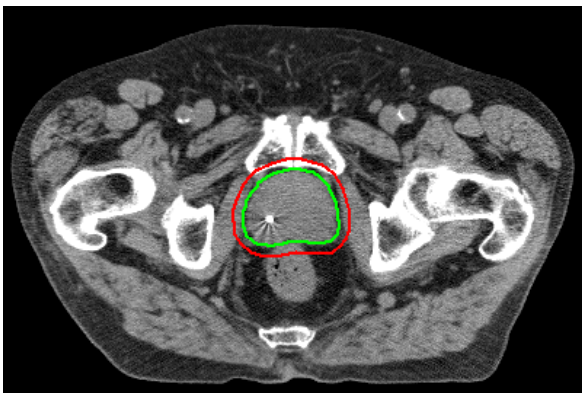

Figure 2.6: CTV (green) and PTV (red) drawn on a computed tomography slice, one of the Calypso beacons can be seen.

breath hold has the additional advantage of reduced lung tissue density, leading to less normal lung tissue in the radiation field compared to other breathing phases.

2.2.3.2 Treatment margins

During the treatment planning process, the target volume as well as organs at risk have to be defined based on imaging data. Around the clinical target volume or internal target volume (CTV or ITV, see section 2.1.1) a planning target volume is defined by adding a margin according to (ICRU, 1993). This is a region, where no tumor cell can be assumed under the anatomic conditions of the planning image data. It is only defined because of the uncertainties of volume delineation, treatment delivery and anatomic and physiologic changes between or during fractions. In fig. 2.6 a CTV and a PTV contour can be seen drawn in a transversal CT slice of a prostate patient. This margin leads to an enlargement of the irradiated volume, and due to that, to a higher radiation dose in parts of organs at risk. Thus these margins should be kept as small as possible to prevent radiation induced side effects. The margins calculated from collected motion data in this thesis are all CTV-to-PTV margins for the compensation of positioning errors or intrafraction motion for prostate irradiation.

The determination of an appropriate CTV-to-PTV margin is commonly not based on motion data from the individual patient but from population based data. This is because of the absence of information about the individual motion prior to therapy. There are various publications about a reliable method of margin determination, for a review see (van Herk, 2004).

The most widely used method is based on (van Herk et al., 2000). They calculated histograms of CTV coverage probability depending on systematic and random errors in treatment preparation and execution. To derive a certain margin recipe from their work, first a clinical decision on desired CTV coverage probability has to be made. The margin recipe used in this thesis is for the case that at least 90 % of the patients shall get a minimum of 95 % of the prescribed dose in the whole CTV. Another fixed input parameter is the width of the beam penumbra, which has to be regarded in the random error term as σ_p. This σ_p

is estimated with 3.2 mm (van Herk et al., 2000) in water equivalent soft tissue, but has to be larger for lower tissue densities (Witte et al., 2004), resulting in a smaller margin. In this thesis margins are only calculated for prostate treatments, hence the value for water equivalent tissue is used, σ_p is already integrated in eq. (2.1).

The formula to derive a CTV-to-PTV margin M is then:

$$M = 2.5 \cdot \Sigma + 0.7 \cdot \sigma. \tag{2.1}$$

In this equation Σ and σ represent the standard deviations of the systematic and the random error in patient position, respectively. These values have to be determined from the patient population. They are specific for the tumor site, the immobilization method and in principle for the patient population. They are determined as follows: After collection of data from various patients, for each patient a mean m_P and standard deviation σ_P of the target's deviation from the planned position is calculated. The standard deviation of the systematic error Σ is then determined as the standard deviation of all patient's m_P. The standard deviation of the random error σ is calculated as the root mean square of the patient's σ_P. For consideration of different sources of error, like positioning and intrafraction motion, the standard deviations can be added quadratically, before the margin calculation. All margins derived in this thesis are isotropic margins, which means that no different margins for lateral, longitudinal and vertical expansion of the CTV are calculated. Therefore, the standard deviations are determined in all directions and then added quadratically to three-dimensional values.

To reduce CTV-to-PTV margins in lung radiotherapy, the treatment planning can be performed with a CT data set representing the time averaged situation, reducing the systematic setup error. This idea is based on the results from (Engelsman et al., 2001) and (Witte et al., 2004). This CT data set can be achieved by choosing the best fitting CT from the 4D data set, then called 'mid-ventilation CT' (Wolthaus et al., 2006), or by reconstruction from a complete 4D CT data set using deformable registration, then called 'mid-position CT' (Wolthaus et al., 2008).

2.2.3.3 Probabilistic planning

In probabilistic planning the commonly used static patient model is replaced by a probability distributions of patient positions as proposed e.g. by (Löf et al., 1995; Li and Xing, 2000; Birkner et al., 2003). An implementation of probabilistic planning within a treatment planning program was realized by (Unkelbach and Oelfke, 2004) by integration of distributions representing interfraction motion measured with repeated CT scans. The implementation addresses the two main challenges of probabilistic planning. First, the probability distribution of patient positions is generally unknown and has to be estimated from only a few snap shots of patient positions. Second, the treatment is performed in a finite number of fractions. The optimized parameter is the expectation value of the dose, instead of the static dose value. It was found, that an additional minimization of the dose variance is necessary to gain clinical applicable treatment plans. This method was further developed to integrate combined patient specific positioning data and population based knowledge on position distributions (Unkelbach and Oelfke, 2005).

Probabilistic planning has also been demonstrated to be able to incorporate variations of intrafractional breathing motion into a 4D treatment planning process. The classical non-probabilistic 4D planning approach for consideration of lung tumor motion as e.g. proposed by (Zhang et al., 2004) uses the different phases of a 4D CT to calculate a motion vector for each pixel of tissue relative to the exhale phase. This information is used to calculate cumulative pixel doses summing up all contributions of each breathing phase weighted with the proportion of breathing cycle time in which this phase is present. This cumulative dose is optimized instead of a static dose using one CT data set only. This approach does not consider possible variations in breathing motion over single fractions or the whole treatment course, the information gathered from the 4D CT is assumed to represent each breathing cycle during the therapy. To overcome this assumption, probabilistic planning can be used to regard variations in tumor amplitude and motion baseline in 4D planning, see (Heath et al., 2009).

2.2.3.4 Repositioning, gating and tracking

In contrast to the motion management methods described previously, the techniques introduced in the following need monitoring of intrafraction motion of the individual patient. In principle, all near real-time motion detection methods can be used for these methods. The most simple one is a threshold based repositioning of the patient for non-periodic tumor motion. For example a new patient alignment procedure is triggered, when a 3 mm distance from planned position for any direction lasts more than 30 s for prostate patients (Curtis et al., 2013). Another method which is mainly designed for tumors, following respiratory motion is called gating. The goal of gating is the irradiation only at that points in time, when the target volume is in a previously defined window of positions. Typically this window covers the target positions around exhale position (Moorrees and Bezak, 2012), because of the large proportion of breathing cycle time, which is spent near exhale position and the better reproducibility of the exhale position in comparison to inhale position.

The most complex method of compensating intrafractional motion is called tracking. The aim of this technique is a stable relationship between treatment beam and tumor. This can be achieved by either moving the patient or the beam according to the current detected patient motion. Approaches for that are as follows: I) a linear accelerator mounted on a robotic arm (Cyber Knife, Accuray Inc., Sunnyvale, CA), II) a treatment couch mounted on a robotic arm (Hexapod, Medical Intelligence, Germany), III) tracking of the tumor motion due to reshaping of the MLC beam aperture for classic gantry based linear accelerators (Keall et al., 2006, 2014; Krauss et al., 2011b), IV) tracking of the tumor motion by tilting and panning the accelerator-MLC combination (Vero SBRT, cooperation between Brainlab AG, Feldkirchen, Germany and Mitsubishi Heavy Industries Ltd., Tokyo, Japan).

From all of these methods, tracking techniques have to deal most with system latency, i.e. the time between detection of motion and possible reaction on it, due to that, motion has to be predicted from previous positions. An analysis of different prediction algorithms can be found in (Krauss et al., 2011a).

3 The role of organ motion in prostate radiation therapy

In this chapter, first, the measured intrafraction prostate motion is quantified. Second, this data is used to calculate safety margins for different treatment scenarios. And third, the dosimetric consequences of this motion are determined for 21 patients after an experimental validation of the 4D dose reconstruction method.

Parts of the following investigations were presented at scientific conferences (Schmitt et al., 2010a,b, 2012a,b).

3.1 Clinical background and purpose

Prostate cancer is the most common cancer in men in Germany accounting for 25.7 % of all newly diagnosed cancers. This led to about 63500 men with this diagnosis in 2008. Although the relative 5-year survival rate is the second highest for all cancers, at 92 %, roughly 12000 men died due to prostate cancer in Germany in 2008, ranking it third in cancer caused mortality. The mean age at diagnosis is 70 years. Looking at time resolved analysis, the new cases per year are increasing, mainly because of the implementation of screening. Screening leads to a diagnosis at younger age and at earlier stages of cancer progression, not causing any clinical symptoms. This leads to a slight decrease in mortality rate by an increasing incidence rate, because early detected carcinomas are more likely to be cured. (RKI, 2012)

Beside additional hormone therapy for high risk cases, the two main therapy options for localized prostate carcinomas are radiotherapy and surgery (radical prostatectomy). The radiotherapy can be performed as external beam radiotherapy (EBRT) or brachytherapy (permanent or temporary incorporation of encapsulated radioactive material into the tumor) or as a combination of both. There is no clear advantage of one of the two options radiotherapy and surgery, neither regarding the overall survival rates nor the spectrum of side effects. (S3-Leitlinie, 2011; Resnick et al., 2013)

In radiotherapy of localized prostate carcinomas, dose escalation is shown to improve the clinical outcome (Dearnaley et al., 2005; Peeters et al., 2006). Because of the necessity of dose sparing for organs at risk, dose gradients and general target volume conformity of dose distributions have to be optimized for these higher target doses. Therefore, conventional IMRT and volumetric arc therapy is widely used for prostate patients.

These techniques require advanced assessment and management of interfractional anatomy changes, patient positioning and intrafractional organ motion. For the selection of proper

strategies per tumor site or even per patient it is important to know, how large these deviations are and which dosimetric effects have to be expected.

Intrafractional prostate motion was investigated using for example MV portal imaging (Nederveen et al., 2002; Kotte et al., 2007) or electromagnetic transponders (Kupelian et al., 2007; Langen et al., 2008b; Shah et al., 2011a). This chapter, first, describes typical motion patterns and quantifies the overall motion amount resulting from the individual motion patterns of our patients. This investigation characterizes the input for further margin determinations and calculations of dosimetric consequences of this motion. Due to that, it is presented to give an overview of the general and time dependent behavior of prostate displacement and is compared to published motion data to enable a more valuable discussion of the investigations based on this data presented in the following.

Most investigations on margins for intrafractional prostate motion published so far are based on complete fractions of conventional IMRT, e.g. (Litzenberg et al., 2006; Tanyi et al., 2010). Data on intrafraction motion and margins compensating for them considering different fraction times are very rare (Li et al., 2013). For prostate radiotherapy different treatment techniques and fractionation schemes, leading to different fraction times are applied. Reported treatment times reach from 2 min for single arc volumetric-modulated therapy (Chow and Jiang, 2013) up to 20 min to 40 min including imaging for hypofractionated linac-based stereotactic body radiotherapy (Madsen et al., 2007). Therefore CTV-to-PTV margins, which are necessary to avoid an underdosage of the CTV when no other motion management is applied, depending on different treatment times are calculated in this chapter.

In addition, two widely used strategies of MV CBCT usage for prostate patient positioning prior to each fraction are analyzed in comparison with a positioning using the electromagnetic system, which serves as ground truth. In these methods, the daily MV CBCT is compared with the planning kV CT, a translation vector is calculated and the patient is repositioned according to this vector. A registration of prostate positions in the image data is not possible, because of the less soft tissue contrast of the MV CBCT compared to the kV CT. Due to that, it is common either to use the bony anatomy for image registration or implanted fiducial markers in the prostate. The aim of marker implantation is thereby the assumption of a better representation of the prostate position, compared to the bones. Differences in bone and marker positioning are reported for different MV and kV imaging modalities (Nederveen et al., 2003; Beltran et al., 2008; Tanyi et al., 2010). These differences are caused by changes of the prostate position relative to the bones from day to day and on short time scales.

Margins are based on a concept of average motion of a patient population. The motion of the patient, for which the concept is applied during treatment planning is not considered. Because of that, this margin is larger than necessary for some patients and smaller than required for other patients. To quantify this effect, a patient specific evaluation of the dosimetric consequences of the intrafraction motion is performed. For this, three calculation methods for dose distributions considering intrafraction motion are evaluated using film dosimetry in a moving phantom as ground truth. For these film measurements, original patient motion data of whole treatment courses containing 35 fractions are mimicked by a movable phantom fixture during the irradiation of all fractions on one film. Based on this analysis one dose recalculation method is chosen for application to all patient data.

The dosimetric effects for whole treatment courses reported so far were mainly indicating to be negligible even on the PTV, although the effect for single fractions was remarkable in some cases (Li et al., 2008a; Langen et al., 2012). Using the same motion data for calculation of dosimetric effects for seven field step-and-shoot IMRT (Langen et al., 2012) and helical TomoTherapy treatments (Langen et al., 2008a), both without a boost concept, very different results are obtained. Additionally, several investigations on correlation between motion amount and dosimetric effect using different motion metrices and dosimetric endpoints are done concluding that there was a rather poor correlation between the two, (Langen et al., 2008a, 2012). In this thesis a retrospective quantification of the dosimetric effect of intrafraction prostate motion and a correlation analysis between three dosimetric endpoints of single fraction and cumulative plans and the geometric mean of the prostate displacement is performed for prostate treatments with an integrated boost irradiation delivered by a conventionally fractionated nine field step-and-shoot IMRT.

3.2 Material and methods

3.2.1 Patient data

All data from prostate patients used in this analysis are collected during a clinical trial performed in a cooperation between the dkfz and the University Clinic Heidelberg, represented by the departments of radiation oncology and urology. The title of this trial is „Online-Erfassung der Prostata-Position und eventueller Repositionierung bei der intensitätsmodulierten bildgestützten Strahlentherapie (IGRT) der Prostata mittels implantierter Radiotransmitter“ (engl. “On-line detection of prostate position and potential repositioning for intensity modulated image guided radiotherapy (IGRT) of the prostate due to implanted radio frequency transmitters”). This trial was approved by the ethics committee of the medical faculty of the University of Heidelberg (approval number MV-086/2007). The patient selection and information was done in the radiation oncology department. After each patient had agreed to take part in this trial, three Calypso transponders, as introduced in section 2.2.2.2, were implanted in the prostate endorectally with ultra sound guidance at the urology department. The treatment planning and the treatment itself were performed at dkfz.

One week after the implantation of the transponders, the treatment planning CT was acquired. In this kV CT the transponders were identified and target delineation, dose prescription, calculation and optimization was performed. The general concept of irradiation was an integrated boost, which leads to a high dose region in the CTV (called a boost volume) and a lower prescribed dose in the margin around it. The prostate was defined as boost volume and planned with a prescribed median dose of 76 Gy with an enclosing 95 % isodose. This volume was expanded by a margin of 7 mm including the base of the seminal vesicles with a prescribed dose of 70 Gy with an enclosing 95% isodose. The larger volume is called PTV. All used treatment plans were approved and employed for patient treatments, hence some plans differ from this concept, especially in the posterior margin close to the rectum, due to the physicians decisions. There was no dietary protocol, but the patients were asked for having an empty rectum and a full bladder during planning CT and treatment fractions. For each patient, a step-and-shoot IMRT with 9 coplanar equidistant beam

angles was performed. This treatment was split up in 35 daily fractions. Prior to each fraction an MV CBCT was acquired for image guided patient position correction. After that, the Calypso System was used to determine the prostate misalignment. Depending on the detected positioning errors by both systems, the patient was repositioned either using the Calypso information or the MVCT information depending on the physician's decision. After the completion of the positioning procedure, the irradiation was performed with concurrent prostate motion monitoring with the Calypso System.

For 25 enrolled patients the intrafractional prostate motion was monitored. For each investigation presented in this thesis, specific requirements had to be fulfilled e.g. regarding number of fractions with complete Calypso data set or length of data sets. Therefore for each investigation a different subset from these 25 patients was chosen.

Depending on the analysis, the following patient related data was used: I) kV planning CT, II) treatment plan including all beam angles, beam apertures and applied monitor units per segment, III) daily MV CBCT data sets and IV) Calypso motion data including beam status report.

3.2.2 4D dose reconstruction methods

This section describes the methods used to reconstruct dose distributions applied to a moving phantom or patient. In a first part, the dose calculation itself, based on the interaction of the applied radiation with the matter of the phantom or patient, is depicted. Using these methods, the dose distributions are optimized during the treatment planning process under static conditions. Second, it is presented how dose distributions are accumulated considering the phantom or patient motion during irradiation.

3.2.2.1 Dose calculation models

Dose calculation in radiation therapy is usually divided in two parts. (1) The determination of the output of the radiation source and (2) modeling of the interaction between the radiation and the patient leading to the absorbed dose in the patient. The output of the radiation device, here the properties of the primary photon beam, is determined once. This determination is independent of the dose calculation algorithm used to compute the dose deposition in the patient, in principle, but the needed input parameters vary between algorithms.

The primary photon beam The best estimation of the output phase space of the accelerator would be determined with a complete Monte Carlo simulation beginning with the electron spectrum emitted by the electron gun, tracing the electrons to the bremsstrahlungstarget and then simulating the interactions of the produced photons until the beam aperture forming devices, specific for the patient. In this way, data on the distribution of photon energies and directions as well as the fluence, i.e. the number of photons crossing a specified area, can be derived directly. Additionally, this simulation will provide information about electrons contaminating the primary photon beam. But such a Monte Carlo simulation requires exact knowledge of all involved components, which is often not available

in clinical practice. To overcome this lack of information, measurements have to be performed for example to determine depth dose curves, lateral dose profiles and the influence of the aperture forming collimators due to beam scattering. This measured data is then fitted to simulated data to establish a beam model. For example, the depth dose curve can be compared with depth dose curves for a weighted sum of mono energetic photon beams, generated with Monte Carlo simulations, the contaminating electrons are thereby implicitly accounted for by an over weighting of low photon energies. In this way, a model of the primary photon beam, that is compatible with the measured data, can be determined. If the dose calculation in the patient is performed with Monte Carlo simulations, too, the modeled phase space can be used as input directly (for an overview of beam modeling issues in Monte Carlo methods in radiation therapy, see (Chetty et al., 2007)). For kernel based dose calculation algorithms the primary energy fluence of the photon beam can be derived from the measurements and used as input. The primary energy fluence ψ describes the energy of the radiation field per area in each point in space $\boldsymbol{r}$ for each contributing photon energy E and its corresponding primary fluence ϕ:

$$\psi(E, \boldsymbol{r}) = E \cdot \phi(E, \boldsymbol{r}). \tag{3.1}$$

Primary thereby denotes the aspect, that these photons are produced outside the patient, in contrast to secondary electrons or Compton photons inside the patient. From now on, energy or particle fluence always refers to the corresponding primary fluence.

Dose deposition in the patient The calculation of the applied dose to the patient in clinical practice shows two conflicting requirements. First, the result should be as accurate as possible, but second, the calculation has to be as fast as possible. Speed of dose calculation is important during the iterative treatment plan optimization process, requiring a large number of calculations, in particular. The final dose calculation using the optimized beam apertures and beam weights for evaluation of the dose distribution can be performed with a more accurate slower algorithm, in principle. The most accurate method of dose calculation in the patient is a Monte Carlo simulation for which the material composition of the patient is estimated from the patient CT, an introduction to Monte Carlo treatment planning methods can be found in (Fippel, 2006). This simulation is much more time consuming than other methods, but recent developments in simulation software as well as in the used hardware made it clinically available in some commercial treatment planning programs (Monaco by Elekta AB, Stockholm, Sweden, MultiPlan by Accuray Inc., Sunnyvale, CA, US, ViewRay treatment planning system by ViewRay Inc., Cleveland, OH, US).

Nevertheless, the classic approach of dose calculation, a kernel based method introduced by (Mackie et al., 1985) and (Ahnesjö et al., 1987), is used in the vast majority of clinical dose calculations and is applied to all patient cases considered in this thesis. Kernel based methods divide the dose deposition in two components. First, the energy transferred to the patient by primary interactions of the photon beam with the patient is determined and second, the dose deposition around each point of primary photon interaction, done by secondary electrons, is modeled by a so called dose kernel. The inaccuracy inherent in the kernel methods is the assumption of a patient consisting of water, while the different media like bone and diverse organ tissues are considered as water with different electron densities in an inhomogeneity correction. This assumption leads to deviations between the calculated

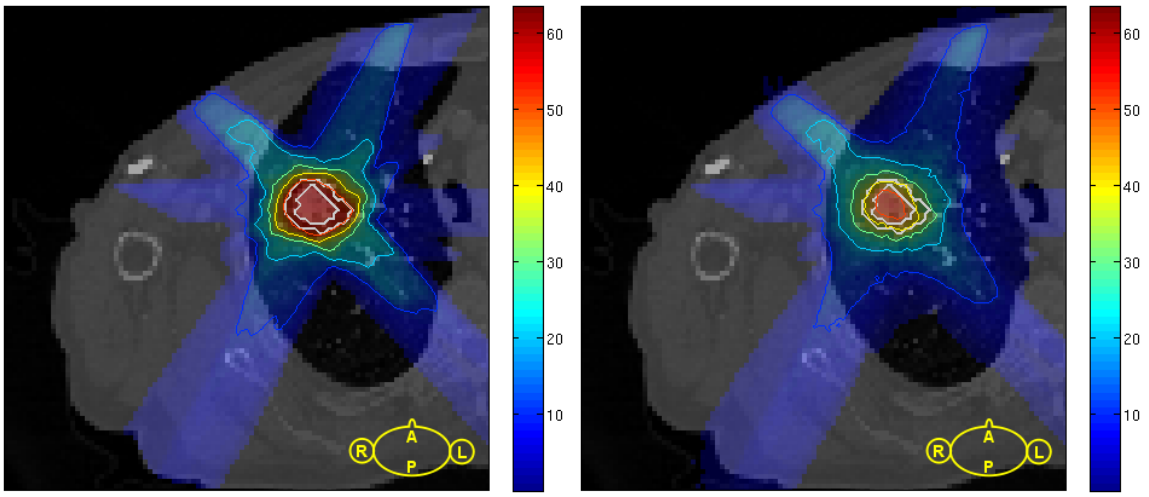

(a) (b)

Figure 3.1: Calculated dose distributions for a pencil beam algorithm (a) and a Monte Carlo simulation (b) in a lung case, the scale is in Gy. The optimization was performed with pencil beam dose distributions. The Monte Carlo recalculation of the delivered dose shows an underdosage of approximately 20 % in the tumor. Taken from (Siggel, 2012), with permission.

dose using kernel based methods and Monte Carlo calculations, often used as gold standard. The amount of these deviations depends on the applied kernel method and on the presence and distribution of not water equivalent tissues. Largest effects are observed in the head and neck region and in lung irradiation, because of a high percentage of air filled cavities and lung tissue with very low density. An example of deviations between dose calculation with a pencil beam kernel and with a Monte Carlo algorithm in a lung case is shown in fig. 3.1.

In the following, the principle of dose calculation with point spread and pencil beam kernels will be explained for dose deposition in water, after that, the inhomogeneity corrections are presented. The energy transfer from the photon beam to the patient is thereby described by the TERMA T (Total Energy Released per unit MAss). The TERMA for each photon energy E and point in space $\boldsymbol{r}$ is given by the linear attenuation coefficient μ, the mass density ρ and the energy fluence ψ:

$$T(E, \boldsymbol{r}) = \frac{\mu(E, \boldsymbol{r})}{\rho(\boldsymbol{r})} \cdot \psi(E, \boldsymbol{r}). \tag{3.2}$$

Depending on the specific photon energy the attenuation coefficients for the photoelectric effect, the Compton effect and pair production has to be considered. The spatial dependence of the energy fluence can be described approximately by the attenuation of the photon fluence ϕ due to the traversed medium until the regarded point $\boldsymbol{r}$. The photon fluence $\phi(d)$ in the tissue depth d is attenuated to:

$$\phi(d) = \phi(0) \cdot e^{-\mu \cdot d}, \tag{3.3}$$

with the initial fluence $\phi(0)$. The deposited dose D in the patient for each point $\boldsymbol{r}$ is the result of the superposition of the dose contributions from each primary interaction point $\boldsymbol{r'}$.

This dose contribution can be calculated via a multiplication of the TERMA $T(\boldsymbol{r'})$ in the primary interaction point and the dose kernel $k(\boldsymbol{r}, \boldsymbol{r'})$ describing the energy transport from $\boldsymbol{r'}$ to $\boldsymbol{r}$. An integration over all primary interaction points and all occurring photon energies E' gives the dose $D(\boldsymbol{r})$:

$$D(\boldsymbol{r}) = \int_E \int_V T(E', \boldsymbol{r'}) \cdot k(\boldsymbol{r}, \boldsymbol{r'}, E')\, d\boldsymbol{r'} dE'. \tag{3.4}$$

These kernels k are called point spread functions or point kernels and the corresponding calculation is called a superposition algorithm. Kernels for each photon energy can be derived with Monte Carlo simulations or by adapting analytical models using measured data. With the assumption of a translational invariant kernel, the calculation can be transformed to a convolution algorithm, which can be performed much faster:

$$D(\boldsymbol{r}) = \int_E \int_V T(E', \boldsymbol{r'}) \cdot k(\boldsymbol{r} - \boldsymbol{r'}, E')\, d\boldsymbol{r'} dE' = \int_E (T * k)(E', \boldsymbol{r})\, dE'. \tag{3.5}$$

To further reduce the computational effort, the concept of a pencil beam kernel can be used, as proposed e.g. by (Mohan et al., 1986) and (Ahnesjö et al., 1992). The idea is to not account for every single primary photon interaction during the dose calculation but to use pre-calculated kernels describing the dose deposition of an infinitely narrow photon beam (pencil beam). This pencil beam kernel k_{PB} is achieved by integrating point dose kernels for primary interaction points over depth in water. A schematic of a point dose kernel and a pencil beam kernel is shown in fig. 3.2. These pencil beam kernels are explicitly dependent on the water depth d and account for the whole energy spectrum in this depth and the attenuation of the primary photon beam. Hence, the dose calculation for each point $D(x, y, d)$ with x and y being the coordinates perpendicular to the incident photon beam is reduced to a two-dimensional convolution of the energy fluence $\psi(x, y)$ for the whole spectrum and the pencil beam kernel:

$$D(x, y, d) = \int_x \int_y \psi(x', y') \cdot k_{PB}(x - x', y - y', d)\, dx' dy'. \tag{3.6}$$

The assumption of a translational invariant polyenergetic kernel neglects the lateral differences in beam spectrum, called off-axis beam softening. It has been shown, that the use of the energy fluence $\psi(x, y, d = d_{\text{ref}})$ in the reference depth $d_{\text{ref}} = 10\,\text{cm}$ water instead of the common use of the incident energy fluence $\psi(x, y, d = 0)$ can compensate for that (Ahnesjö and Trepp, 1991).

The kernel based algorithms described so far are based on dose deposition in water and do not account for tissue inhomogeneities. The integration of inhomogeneity corrections differs from method to method and thereby leads to an increasing inaccuracy with an increasing level of approximation from superposition to pencil beam algorithms. All these corrections use the concept of a radiological depth, which is illustrated for a medium containing 3 tissues with different relative electron densities ρ_e compared to water in fig. 3.3. The radiological depth d_r has to be calculated as weighted sum over the tissues until the considered depth:

$$d_r = \sum_{i=1}^{N} \rho_e(i) \cdot d_i, \tag{3.7}$$

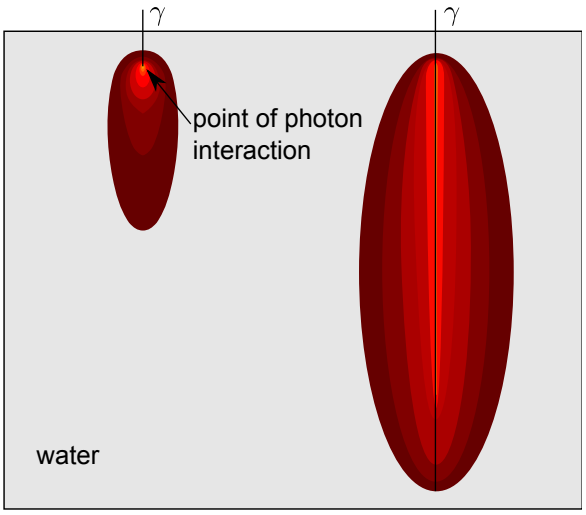

Figure 3.2: Dose kernels describing the energy deposition around primary photon interaction points in water. For the point kernel (left) only one interaction point is regarded, while the pencil beam kernel (right) accounts for all interaction points of a narrow photon beam. Adapted from (Siggel, 2008), with permission.

with N crossed tissue sections and their relative electron densities and path length, as depicted in fig. 3.3. The path lengths are thereby determined using a so-called ray tracing algorithm.

Most obvious, this radiological depth can be used instead of the geometrical depth d to determine the fluence in eq. (3.3). In a second step, the dose kernels have to be adapted to the specific spatial tissue distribution. This adaption is based on O'Connor's theorem, which indicates, that for an impinging energy fluence the deposited dose in a volume v_1 with electron density $\rho_{e,1}$ equals the dose in a volume $v_2 = (\rho_{e,1}/\rho_{e,2})^3 \cdot v_1$ with the electron density $\rho_{e,2}$, (O'Connor, 1957). For point kernels a ray tracing between each primary interaction point $\boldsymbol{r}'$ and each dose point $\boldsymbol{r}$ can be performed to calculate the respective radiological depth and derive a irregular shaped dose kernels. During this ray tracing a linear path of the secondary electrons is assumed, which is less accurate for growing distances between $\boldsymbol{r}'$ and $\boldsymbol{r}$. The isodose lines of these kernels will be stretched/compressed compared to the water kernel when a tissue with a lower/higher electron density compared to water has to be traversed. These adapted point kernels are not translational invariant and can thereby be used only for superposition methods and not in a conventional convolution algorithm.

When the concept of radiological depth is applied to correct pencil beam kernels for tissue inhomogeneities, the kernels are simply stretched or compressed regarding traversed tissue. This is done by substitution of the geometrical depth d with the radiological depth d_r in eq. (3.6). Because of the narrow beam geometry, no lateral deviations are considered. This leads to the assumption of a local slab geometry of different tissues.

Regarding the different levels of approximation and the quality of inhomogeneity corrections the dose calculation algorithm should be chosen depending on the treatment site. In the aforementioned head and neck region and for lung irradiations a superposition or Monte Carlo based algorithm should be used. Other anatomical regions are sufficiently homogenous

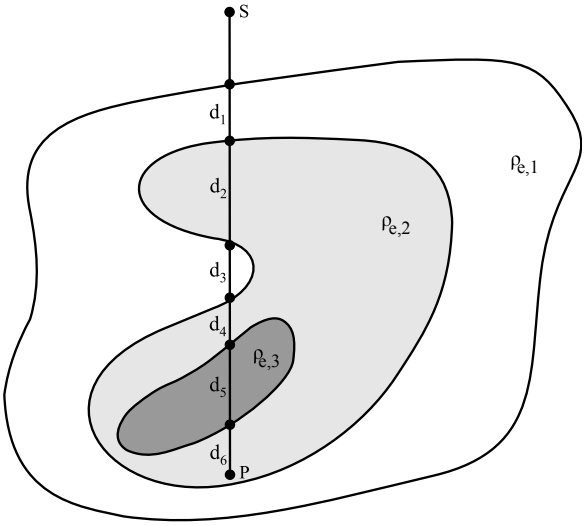

Figure 3.3: Schematic for the determination of the radiological depth from point S to point P. For each region of electron density the path length has to be determined. Adapted from (Siggel, 2008), with permission.

by means of electron density to justify the use of a pencil beam algorithm for fast dose calculation. Because of that, the dose distributions calculated for prostate patients in this thesis are generated with a pencil beam algorithm in an in-house implementation following (Bortfeld et al., 1993).

3.2.2.2 4D dose accumulation

The retrospective analysis of dosimetric consequences of intrafraction organ motion implies an accumulation of delivered dose in each analyzed voxel of the patient or phantom CT. For this accumulation two different concepts are used in this thesis. In the first one the pre-calculated static dose distributions serve as input for a convolution with a possibility density function of the occurring target displacements, while in the second concept a new dose calculation within the treatment planning program is performed using motion dependent target points.

Dose accumulation by convolution For each voxel of interest in the static patient CT, the dose contribution of each part of the patient motion has to be considered. When possible interplay effects between patient motion and accelerator head and collimator leaf motion is neglected, this can be done by a convolution of the static dose distribution D_{static} with a probability density function p of the target displacement, see eq. (3.8). The 'moved' dose distribution $D_{\text{moved}}(\boldsymbol{r})$ in each CT voxel is thereby estimated as integral over the dose in all voxels $\boldsymbol{r} - \boldsymbol{r'}$ of the static dose distribution, weighted with the probability $p(\boldsymbol{r'})$ of this specific displacement during the irradiation.

$$D_{\text{moved}}(\boldsymbol{r}) = (D_{\text{static}} * p)(\boldsymbol{r}) = \int D_{\text{static}}(\boldsymbol{r} - \boldsymbol{r'}) \cdot p(\boldsymbol{r'}) d\boldsymbol{r'}. \tag{3.8}$$

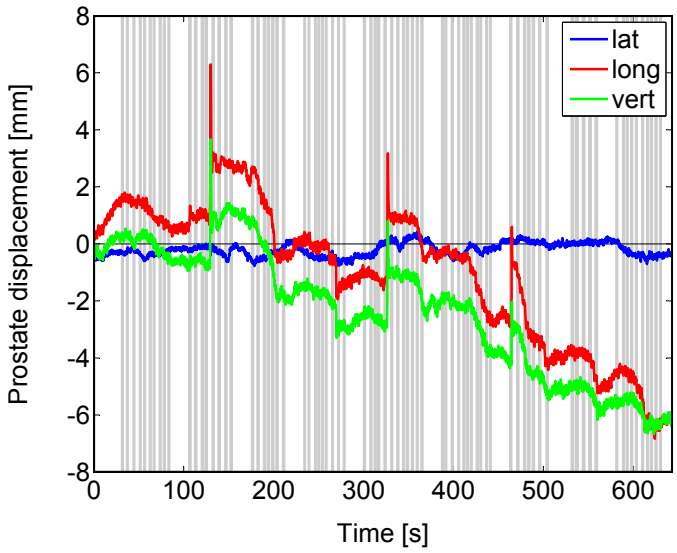

Figure 3.4: Example of Calypso motion data for one fraction. Shaded areas indicate times of irradiation (IMRT segments).

We made this calculation with two types of motion data sets acquired with the Calypso System. In the first case, all collected data points between the first and the last Calypso beam-on signal of all fractions were filled in one pdf of prostate displacements, later addressed as 'whole dataset convolution'. In the second case, only the motion data with activated Calypso beam-on signal was used for the pdf, this means the motion during pauses between the beams and segments was ignored, this method is later addressed as 'beam-on convolution'. This was done to evaluate, if there are characteristics of intrafraction prostate motion depending on the beam status, recognized by the patient, which are dosimetrically relevant. A pattern of beam-on and beam-off phases can be seen in fig. 3.4.

All convolutions were done using a MatLab script (The MathWorks Inc., Natick, MA).

Plan recalculation with shifted target points To consider all interplay effects in the dose accumulation, a method to recalculate dose distributions for given treatment plans and target motion data was implemented for our in-house treatment planning system. This tool performs a dose calculation for each delivered IMRT segment using a dedicated target point, determined from the motion data, to simulate the process of irradiation. Each of the 35 fractions were delivered in about $N \approx 80$ IMRT segments. For all segments, the mean prostate misplacement was determined from the Calypso data and converted to our CT coordinate system, denoted with (x, y, z). The relation to the IEC-61217 axes (Calypso System) here denoted as 'lat, long, vert' is as follows: x = lat, y = -vert and z = long. Using these misplacements, dose distributions were calculated based on the static treatment plans with the following procedure. For every segment s of every fraction f the dose distribution $d_{f,s}(\boldsymbol{r}, x, y, z)$ with $\boldsymbol{r}$ being a point in space and x, y, z the current target point was calculated. The current target point is defined as $(x, y, z) = (x_0 - \bar{x}_{f,s}, y_0 - \bar{y}_{f,s}, z_0 - \bar{z}_{f,s})$ with the original static target point (x_0, y_0, z_0) and the lateral, longitudinal and vertical seg-

ment's mean prostate misplacement $(\bar{x}_{f,s}, \bar{y}_{f,s}, \bar{z}_{f,s})$. The resulting dose distributions were then summed up to 35 'moved' fraction plans and one 'moved' cumulative plan for every patient, see eqs. (3.9a) and (3.9b).

$$D_{\text{moved},f}(\boldsymbol{r}) = \sum_{s=1}^{N} d_{f,s}(\boldsymbol{r}, x, y, z), \tag{3.9a}$$

$$D_{\text{moved, cum}}(\boldsymbol{r}) = \sum_{f=1}^{35} D_{\text{moved},f}(\boldsymbol{r}). \tag{3.9b}$$

3.2.3 Dose reconstruction – validation strategies

To validate the 4D dose accumulation methods, film measurements were performed as ground truth. In this section, the experimental setup is described as well as the used concepts to compare dose distributions.

3.2.3.1 Experimental setup

Dose distributions in a static and in a moving phantom were measured with the setup shown in fig. 3.5(a). The films were placed in the isocentric transversal slice of a cylindrical solid water phantom with a diameter of 20 cm, which can be seen in fig. 3.5(b). The phantom was mounted on a platform which can mimic 3D motion.

As described later, in section 3.2.4.2, treatment plans and motion data of four patients were chosen for the experimental validation. For each case two film measurements were performed, a static and a moved one. First, one static fraction was irradiated on a radiographic Kodak EDR2 film (Carestream Health Inc., Rochester, NY). Second, 35 fractions were irradiated on one radiochromic MD-V2-55 film (International Specialty Products, Wayne, NJ) while the phantom was moving accordingly to the Calypso motion data. In this way a cumulative 'moved' dose distribution of the whole treatment course was produced on the film. One of these irradiated MD-V2-55 films is shown in fig. 3.5(c).

The EDR2 films were developed and then all films were scanned with a Dosimetry Pro Advantage Vidar scanner (Vidar systems cooperation, Herndon, VA) with a resolution of 300 dpi. Film calibration was made using measurements up to 2.9 Gy for the EDR2 films and up to 118 Gy for the MD-V2-55 films.

3.2.3.2 Quantification of dosimetric differences

The validation of calculation methods as well as the evaluation of dosimetric consequences of the intrafractional motion is based on a comparison of dose distributions. Either between measured and calculated dose distributions or between different calculations. For these comparisons a γ-index analysis is used for both investigations, while the change in $D_{95\,\%}$ of patient specific target volumes is used in the patient application part only.

(a)

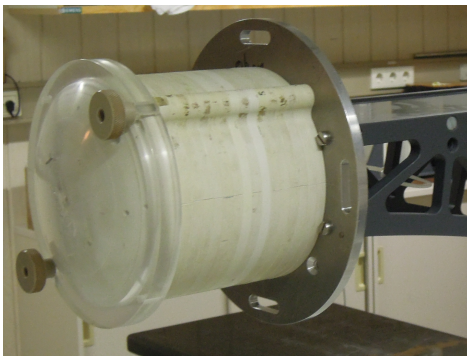

(b)

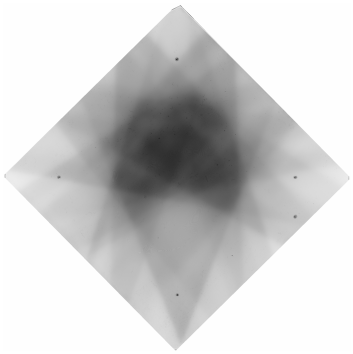

(c)

Figure 3.5: Experimental setup of the film measurements consisting of the Siemens Artiste treatment device and the programmable phantom fixture with the mounted phantom (a). Detailed view on the phantom made of circular solid water plates. The film is placed in the central plate gap (b). Radiochromic MD-V2-55 film after irradiation of 35 fractions in the moving phantom. The marked laser positions can be seen as black dots (c).

γ-index analysis The γ-index concept (Low et al., 1998) is a combination of pure dose differences and spatial dose deviations. It is based on a pixel-by-pixel comparison and can be performed either in 2D or 3D. All pixels $\mathbf{r}_e$ in the evaluated dose distribution for which a pixel $\mathbf{r}_r$ in the reference dose distribution exists, giving a $\Gamma(\mathbf{r}_r, \mathbf{r}_e) \leq 1$ in eq. (3.10), pass the criterion, defined by a dose difference ΔD and a spatial distance Δd, either defined in 2D or 3D. The γ-index is the percentage of pixels in the evaluated dose distribution passing the Γ criterion.

$$\Gamma(\mathbf{r}_r, \mathbf{r}_e) = \sqrt{\frac{|\mathbf{r}_e - \mathbf{r}_r|^2}{(\Delta d)^2} + \frac{(D_e(\mathbf{r}_e) - D_r(\mathbf{r}_r))^2}{(\Delta D)^2}}. \tag{3.10}$$

We used a 3 %/3 mm γ-index in most cases. This means the result is the percentage of pixels in the evaluated dose distribution for which there is a pixel in the reference dose distribution with the same dose in a 3 mm neighborhood or a 3 % deviating dose in the pixel at the same place and combinations between these cases. There are two possibilities to define the dose difference leading to a 'global' or a 'local' γ-analysis. For the global analysis, the dose difference is defined related to the maximum dose and for the local analysis, it is defined relative to the dose in the evaluated pixel. The γ-evaluations made in this thesis are local γ-evaluations, to account for dose deviations outside the high dose region, too.

Change in $D_{95\,\%}$ of a target volume It is also common to compare clinical dose distributions based on the dose calculated for a patient specific target volume like the CTV or the PTV. For this purpose, the $D_{95\,\%}$ of the considered volumes is calculated and compared. The $D_{95\,\%}$ is defined by the constraint that 95 % of the considered voxels receive a dose higher than $D_{95\,\%}$.

3.2.4 Performed investigations and procedures

3.2.4.1 Quantification of prostate motion and its impact on margin sizes

Motion characteristics and quantification First, a visual classification of the collected motion data yields a qualitative overview of the occurring motion patterns. Second, a quantitative analysis of the time dependent overall motion amount resulting from these motion patterns was done using all recorded intrafraction motion data.

Intrafraction prostate motion was summarized for all patients. Resulting in a population based non-individual analysis of motion amount in all three directions and in 3D. Data from 844 treatment fractions from 25 patients was used. For each data set, the points in time between the beginning of the first beam and the end of the last beam, as measured and recorded by the Calypso System, were employed. To consider intrafraction motion only, possible deviations from the planned position were set to zero at the time the first beam starts.

For each point in time after start of irradiation the mean and standard deviation for lateral, longitudinal and vertical prostate deviation from planned position was calculated. Additionally the three-dimensional distance between actual and planned position was determined.

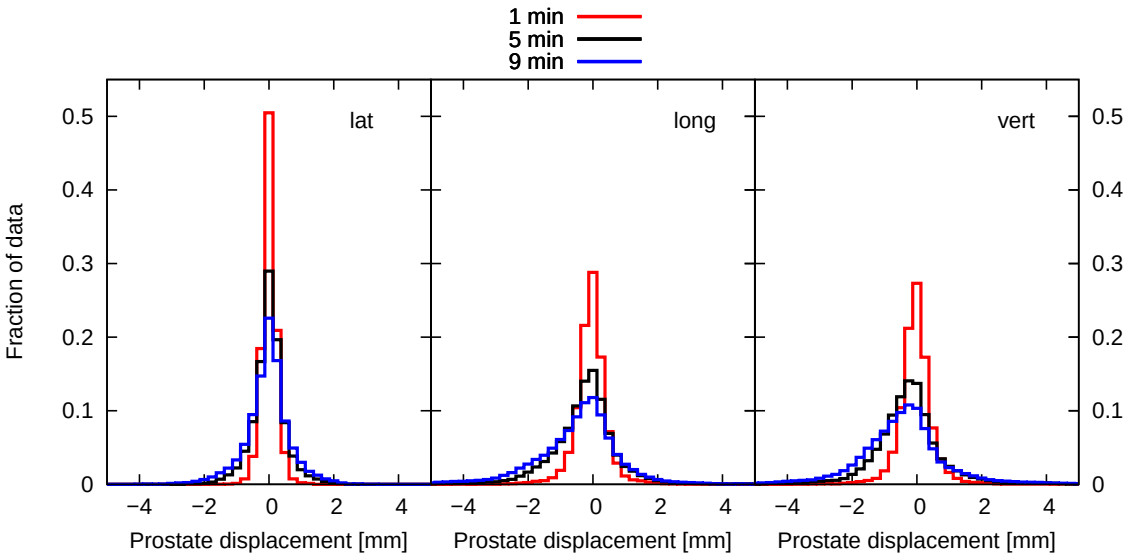

Figure 3.6: Histogram of the distribution of lateral, longitudinal and vertical prostate position for 15 patients. In each diagram data for 1, 5 and 9 min of treatment is displayed.

The time dependent behavior of these parameters was analyzed. It was also calculated for which part of time the 3D prostate displacement exceeded specific deviation thresholds per fraction and for all collected motion data.

Margins for different treatment times In this analysis only patients were included, whose recorded intrafraction motion data between start of first beam and end of last beam lasts for at least 9 min for all fractions. This leads to 340 analyzed fractions for the 10 patients in (Schmitt et al., 2010b), in the following the study is extended by data from another 5 patients giving 507 fractions in sum.

From the 9 min lasting data sets margins for daily treatment times ranging from 1 min to 9 min were deduced. All calculations, except the margin determination itself, are made separate for the three motion directions, for simplicity, the following equations are given for the x-coordinate, only. As can be seen in fig. 3.6, the motion amount per minute is increasing with enhanced treatment times. As the aim was to determine margins for different lengths of treatment time, without any bias due to this fact, each evaluated motion pattern starts at the beginning of the first beam t_s for each fraction f. This leads to the same number of data sets for all simulated treatment times. To consider intrafraction motion only, all intrafractional prostate positions $x^{p,f}_{\mathrm{intra},\,t}$ at time t are taken relative to the start position for patient p and fraction f:

$$x^{p,f}_{\mathrm{intra},\,t} = x^{p,f}_{t} - x^{p,f}_{t=t_s}, \tag{3.11}$$

with the original detected prostate position $x^{p,f}_{t}$. The data sets resulting from these procedures are combined per patient and treatment time. For each patient and treatment duration $d = 1 \ldots 9$ min a data set was constructed by stringing together all fractions F. Each fraction data consists of $d \cdot 600$ data points, because of the 10 Hz update frequency.

This lead to nine combined data sets per patient, one for each treatment duration. For each fraction time, the mean $m_{d,p}$ of the prostate displacement was calculated from these combined data sets for each patient:

$$m_{d,p} = \frac{\sum_{f=1}^{F} \sum_{t=t_s}^{d} x_{\text{intra},\,t}^{p,f}}{F \cdot d \cdot 600}, \tag{3.12}$$

together with the corresponding standard deviation $\sigma_{d,p}$. As described in section 2.2.3.2, population based isotropic CTV-to-PTV margins M_d were derived from this patient specific data using the recipe of (van Herk et al., 2000) via the standard deviations of the systematic error Σ_d and the random error σ_d, calculated for $d = 1 \ldots 9$ min.

Margins for IGRT positioning strategies The margins calculated so far consider intrafraction motion only. Thus a perfect patient positioning procedure is assumed. To estimate the needed margin for consideration of patient setup and intrafractional motion in combination, in the following two methods of image guided patient positioning in prostate radiotherapy using MV cone beam CT are quantitatively evaluated. It is analyzed, which margins should be used to account for positioning errors, if these methods are applied. The Calypso localization serves as ground truth for the prostate position. Data of 10 patients was used for this analysis. For each patient the kV planning CT was used together with the MV CBCT data acquired prior to each treatment fraction. As ground truth served the first position the Calypso System recorded for patient localization. For these 10 patients data from 289 fractions were found to be suitable for the investigations in terms of completeness.

The kV planning CT, acquired with a Toshiba Aquilion CT scanner (Toshiba Corporation, Tokyo, Japan) had the following parameters: 512×512 pixel per transversal slice with a pixel size of 0.976 mm and a slice thickness of 2 mm. The image reconstruction was performed with the standard abdominal kernel (FC13). The daily MV cone beam CT was acquired using the treatment beam of the Siemens Artiste with an opposing flat panel detector, see section 2.2.2.1. The acquisition parameters for these MVCTs were the following: 10 Monitor Units, 360° rotation, one projection per degree. The image reconstruction was performed using a smoothing kernel, resulting in a 3D data set with 512×512 pixel per slice with a three-dimensional isotropic edge length of 0.54 mm of each voxel.

Three implanted Calypso beacons could be identified in the prostate on all considered MV CBCTs and the related kVCT data employed for therapy planning. For each MVCT two image registrations with the planning kVCT of the corresponding patient were made. The aim of the first registration was an anatomy match, dominated by the bone structures. The second match was performed to align the transponder positions. For both a different volume of interest (VOI) was defined in the MVCT. For the first match we used the whole MVCT data set. For the second registration, the transponder match, we defined a small area with the transponders in them. For this the transponder positions in the MVCTs were used, which were read out for ensuring that they do not migrate. For all three directions we used the highest and lowest value of beacon position coordinates to define the bounding box for each patient. Then a 5 mm margin in all directions was added for read out inaccuracies of the beacon positions and inclusion of all transponder edges.

For the image registration an in house implementation of the mutual information match recommended by (Maes et al., 1997) was used. The chosen registration parameters were a histogram of 256×256 bins and 735000 voxels. This means a subsampling for the big VOI and a supersampling for the small VOI. To shorten the calculation time, for all registrations a pre-match was performed based on the shift vector between the isocentre in the kVCT and the zero position of the MVCT. These points would represent the same point in the patient for perfect patient positioning. For fractions with large deviations between the prostate position in the MVCT and the planned target position, the pre-match had to be adapted visually before the beacon match.

We compared the shift vectors from both image registrations with the shift vector the Calypso System indicates in the beginning, the so called localization of the patient. All shifts $\vec{t}$ are accompanied with rotations around all three axes (rotation matrix M). Because of that the shifts are correct only for the rotation point. The rotation point of the image registrations is the central point of the MVCT data set $\vec{c}$. The Calypso System gives the rotation in relation to the planned isocenter $\vec{i}$, or the beacon centroid $\vec{b}$, depending on the Calypso localization mode, see section 2.2.2.2. The shifts of the image registrations were recalculated in the particular Calypso coordinate system using eq. (3.13), here denoted for the isocentric localization mode. The index of $\vec{t}$ indicates the coordinate system.

$$\vec{t}_i = \vec{t}_c - (\vec{i} - \vec{c}) + M^c_{\text{rot}} \cdot (\vec{i} - \vec{c}). \tag{3.13}$$

The differences between the shift vectors originating from image registrations and the Calypso shift vector are then used for margin determination. Thereby, the Calypso data served as ground truth. The standard deviation of the systematic error Σ and the standard deviation of the random error σ of the differences between shifts determined with image registrations and Calypso shifts are calculated. Isotropic three-dimensional CTV-to-PTV margins were determined with these input parameters like described in section 2.2.3.2, eq. (2.1).

3.2.4.2 Experimental validation of 4D dose reconstruction

From the 21 patients used for the evaluation of dosimetric consequences of intrafraction prostate motion, described in section 3.2.4.3, four were chosen for experimental validation of the accumulated dose using film measurements as ground truth. These are the patients 2, 3, 6 and 7. The criteria of patient selection for evaluation were the number of available fractions and good representation of the range of the observed motion amount. The film measurements are described in section 3.2.3.1.

Dose calculation for the phantom The treatment plans of these four patients were transferred to a CT of the solid water phantom. The static phantom dose for one fraction was calculated following the common method used for IMRT plan verification at dkfz, described by (Rhein et al., 2002), aligning the center of the water equivalent material to the machine isocenter. For each patient plan, three 'moved' dose distributions summing up whole treatment courses were calculated using the methods described in section 3.2.2.2 with the original patient motion data.

For both convolution methods, the calculation was performed as follows: I) The static phantom dose was linearly interpolated to a grid size of $0.25 \times 0.25 \times 0.25\,\mathrm{mm}^3$ and scaled with a factor 35 to a whole treatment course. II) Depending on the type of convolution, the appropriate motion data of all fractions was filled in one probability density function (pdf) per patient also binned in $0.25 \times 0.25 \times 0.25\,\mathrm{mm}^3$ intervals. III) The convolution of static dose distribution and the pdf was performed for all four patients and both convolution methods.

The dose recalculation using the shifted target point was applied to the phantom CT using the patient's treatment plans and mean displacements per IMRT segment. The 'moved' dose distribution was calculated using our tool within the treatment planning software for each fraction and then summed up to one cumulative dose distribution, see eq. (3.9). After that, the dose distributions were also linearly interpolated to a grid size of $0.25 \times 0.25 \times 0.25\,\mathrm{mm}^3$. This small voxel size makes the comparison with the film measurements more reliable.

Comparison of measured and calculated dose For the comparison, the γ-evaluation tool within the verification software VeriSoft 3.2 (PTW, Freiburg, Germany) was chosen. In this software, the algorithm proposed by (Depuydt et al., 2002) is used. We chose the calculated dose distributions as reference matrices for the γ-evaluations, because of the larger pixel size. Before the irradiation, the phantom was aligned manually to the laser coordinate system in the treatment room. The lateral and vertical position of the film isocenter was determined from the marked laser positions. An $8 \times 8\,\mathrm{cm}^2$ region of interest (ROI) around the isocenter was selected for a $3\,\%/3\,\mathrm{mm}$ local γ-evaluation. The size of this ROI is restricted by the size of the MD-V2-55 films. All pixels with a dose less than $10\,\%$ as the maximum reference dose were ignored during evaluation to avoid influence of very small dose deviations outside the high dose region. To consider systematic misalignements in longitudinal direction, each of the films was compared with all transversal plan slices within a distance of 2 mm from the isocenter (17 slices per film) of all corresponding calculated dose distributions and the best fitting slice for every film was chosen. The specific longitudinal plan coordinate for each moved film was determined from the target point shifted plans. This did not lead to an advantage for the method of shifting the target point in the comparison, because of very small differences both in best fitting plan slice and between γ-indices from slice to slice, see section 3.3.2.1.

Comparison of calculated dose distributions For the four patients used for the film measurements, a comparison of the calculated dose distributions were made similar to the film comparisons. For each patient, the comparison was made only for the transversal slice the moved film is related to. The ROI was extended lateral and vertical to $11 \times 11\,\mathrm{cm}^2$. A larger ROI could not be evaluated, because outside this area there are small holes in the phantom plates, which are necessary for marking the laser positions on the films. Under these conditions γ-evaluations with $1\,\%/1\,\mathrm{mm}$ and $3\,\%/3\,\mathrm{mm}$ criteria were performed.

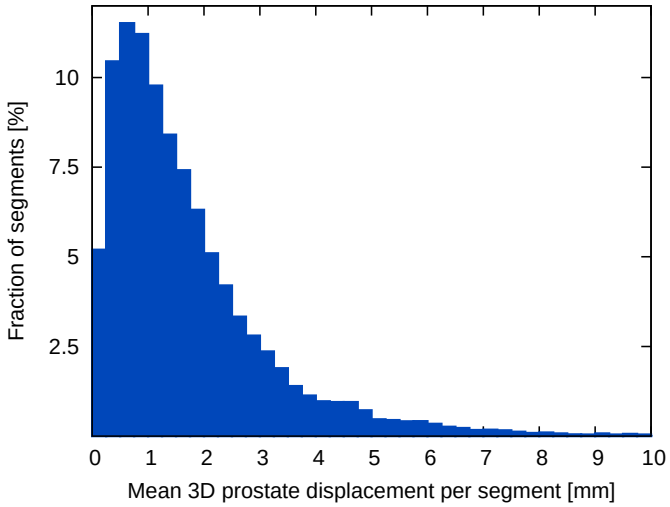

Figure 3.7: Frequency distribution of the segments mean three-dimensional prostate displacement over all patients. The total number of used segments is about 60000.

3.2.4.3 Dosimetric consequences on prostate IMRT

21 patients were chosen from the 25 patients trial cohort using the criterion of a minimum of 32 from 35 delivered fractions completely reported by the Calypso System. For all investigations needing a full treatment course, missing fractions were substituted by randomly chosen other fractions of the same patient to accumulate the whole prescribed dose. In total 17 out of 717 fractions were reused. Some fractions have data gaps of a few seconds which were filled by linear interpolation. To account for the intrafraction motion only, a perfect patient setup prior to the first beam of every fraction was assumed.

The three-dimensional prostate displacement of every segment used for this evaluation is shown as frequency distribution in fig. 3.7.

Calculation of 'moved' dose distributions For all 21 patients, 'moved' fraction dose distributions and one 'moved' cumulative dose distribution were calculated for comparison with the static fraction dose and the static cumulative dose. The 'moved' dose distributions were calculated using the target point shifting method, because of the reasons given in the discussion of the experimental validation (section 3.4.2.1). For these calculations the original voxel size of $1.95 \times 1.95 \times 2\,\mathrm{mm}^3$ was kept.

Comparison of static and 'moved' dose distributions For each patient, the corresponding 'moved' and static dose distributions for fraction plans and cumulative plans are compared using a MatLab script (The MathWorks Inc., Natick, MA) implemented following (Low et al., 1998). This script performs a three-dimensional $3\,\%/3\,\mathrm{mm}$ local γ-evaluation for the following volume of interest (VOI). In the isocentric transversal slice a $16 \times 16\,\mathrm{cm}^2$ region is defined with the isocenter in the middle. This mask was then transferred to all other slices to expand the VOI to the whole longitudinal plan range. The $16 \times 16\,\mathrm{cm}^2$ ROI in each plan

slice was chosen to be as large as possible without including the treatment couch. The static plans were used as reference dose distributions in the evaluation. As in the experimental validation voxels with a static dose less than 10 % of the maximum dose were neglected to eliminate the influence of low dose regions.

For each of the static and 'moved' plans per fraction and treatment course, the $D_{95\,\%}$ was determined for the boost volume and the PTV, like defined in section 3.2.3.2. This was done using an in-house developed script for dose volume histogram analysis. For all fractions and cumulative plans, it was calculated how much the $D_{95\,\%}$ differs for both the boost volume and the PTV between 'moved' and static dose distributions.

Correlation between motion amount and dose perturbation To relate the dosimetric changes with the amount of motion during the particular fraction or treatment course, for each fraction and hence for each treatment course the three-dimensional mean prostate displacement was calculated. For these parameters and the three dosimetric endpoints: γ-index for the comparison of static and 'moved' dose and the occurring changes in the $D_{95\,\%}$ of the boost volume and the PTV, Pearson's linear correlation coefficient was calculated for single fractions and for whole treatment courses.

3.3 Results

3.3.1 Quantification of prostate motion and its impact on margin sizes

3.3.1.1 Motion characteristics and quantification

There are two main types of intrafractional prostate motion occurring in our data, which can be seen in fig. 3.8. This motion mainly takes place in the longitudinal and vertical directions, while the lateral position of the prostate remains very stable. The two motion patterns are called spikes and drifts. Spikes are recurring prostate deviations, as can be seen in fig. 3.8(a), they are probably caused by rectal gas passing the prostate. Additionally the prostate can drift in negative longitudinal and vertical direction, which is shown in fig. 3.8(b). Which means for a patient lying in head first, supine position, a drift towards feet and back. Drifts are mainly associated to consecutive bladder filling and muscle relaxation in the pelvic region. Both motion patterns can occur concurrently.

The used data sets cover 9.4 min on average with a standard deviation of 0.8 min. The length ranges between 5.4 and 16.5 min. In fig. 3.9 can be seen how the lateral, longitudinal, vertical and three-dimensional prostate displacements develop over time. Because of the different length of recorded fractions, there are only a few motion data available for long treatment times. Due to that, the first 9 min are displayed only, ensuring a minimal content of 77 % of all fractions for each data point.

Analyzing the three motion directions, the following results are obtained. The lateral mean prostate position is very stable over time, with a maximum deviation of about -0.2 mm, which is recovered to be smaller then -0.1 mm in the end. The standard deviation of lateral prostate position is thereby growing continuously over time to about 1.0 mm at

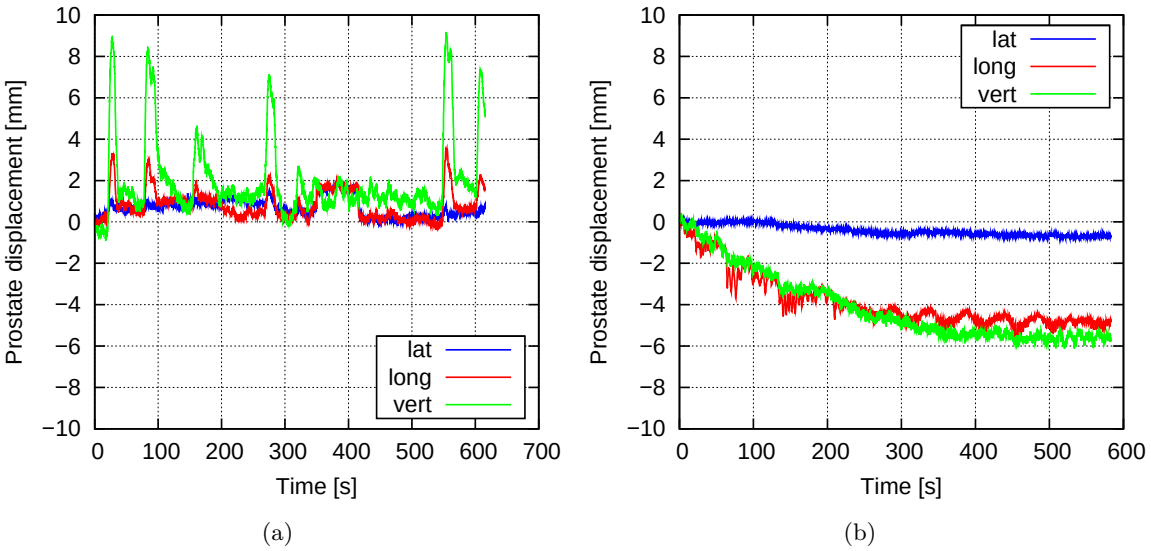

Figure 3.8: Example of prostate motion recorded by the Calypso System. Typical motion patterns can be seen: (a) Spikes in the longitudinal and vertical direction and (b) Drift in the longitudinal and vertical direction.

9 min, see fig. 3.9(a). The longitudinal and vertical prostate positions show a continuous drift towards negative values, resulting in a mean prostate displacement after 9 min of −0.9 and −0.8 mm in longitudinal and vertical direction, respectively, as shown in figs. 3.9(b) and 3.9(c). Additionally to these drifts, the standard deviations around the mean values increase up to 1.9 mm for longitudinal position and to 2.0 mm for vertical position.

The distribution of 3D prostate deviations is positively skewed, because of an accumulation of small values with a few outliers towards large deviations and no negative values. This leads to a large deviation between mean and median of the distribution. Therefore the median is chosen to represent the data and is shown in fig. 3.9(d). The mean is 0.25 mm larger than the median, for all points in time on average. For the three unidirectional distributions, this difference is below 0.06 mm. Because of the increase of three-dimensional prostate displacement with time, the mean–median distance is growing as well and reaches 0.6 mm for 9 min. To illustrate the width of the 3D distribution, instead of the standard deviation, the range of values, covering 68.3 % of all data was calculated. The median thereby splits the region in two 34.15 % covering regions, which are not of the same size. This illustrates the asymmetry of the distribution. As can be seen in fig. 3.9(d), the median 3D prostate displacement increase up to 2.1 mm with a 68.3 % range covering 3.1 mm for 9 min.

For all points in time between start and end of irradiation the 3-dimensional prostate displacement was calculated. With this data, the percentage of time, in which the displacement is above a specific threshold is determined for each fraction and for the whole data set. In table 3.1 the results per fraction are shown. For each fraction the percentage of the specific displacement is calculated. From this data the mean, median and maximum percentage is determined. For thresholds between 1 and 10 mm the mean percentages decreases from 60.9 % to 0.2 %. Up to a displacement of 3 mm the mean and the median are of the same or-

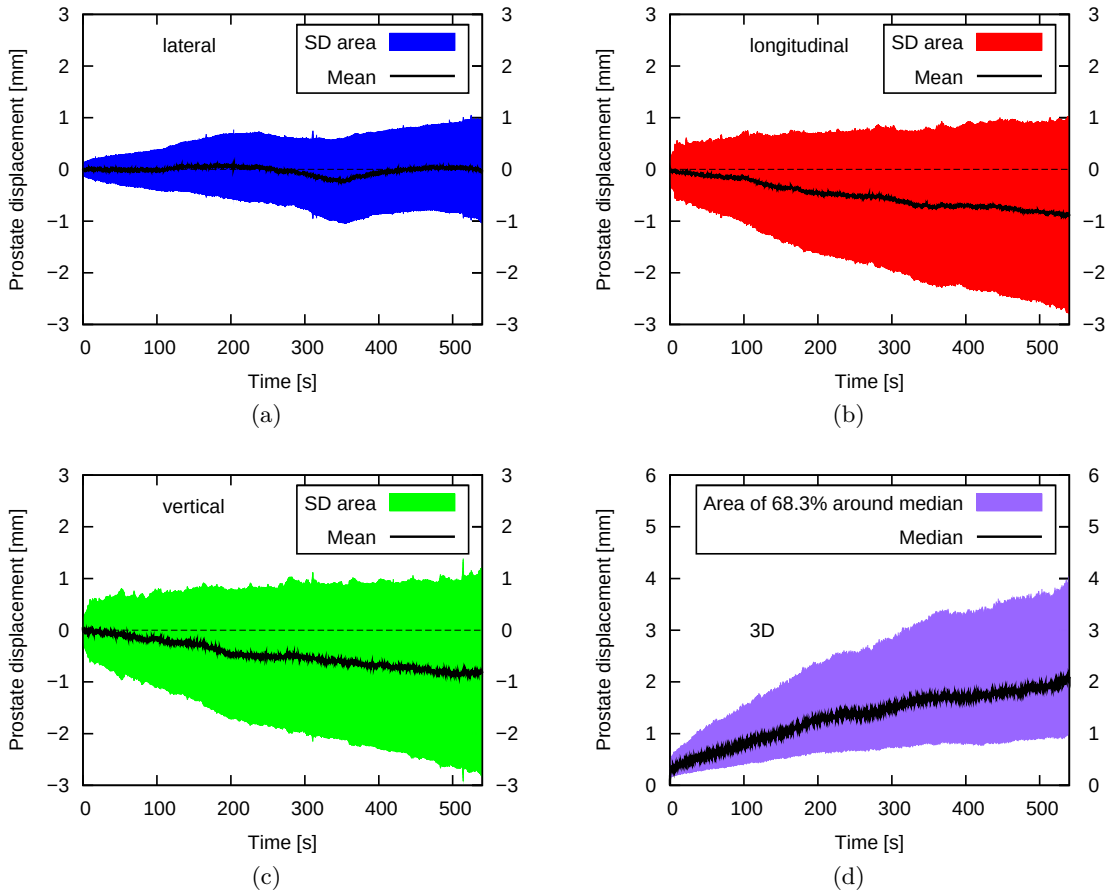

Figure 3.9: Trend of prostate motion over time for all 844 fractions. For the lateral (a), longitudinal (b) and vertical (c) direction the mean value for each point in time is shown with the corresponding standard deviation. For the three-dimensional motion (d) the median value for each point in time is given with a band of 68.3 % of the corresponding data points equivalent to the SDs.

Table 3.1: Mean, median and maximum of the percentage of time for which the three-dimensional prostate displacement exceeds a specified threshold value per treatment fraction.

Displacement [mm]	1	2	3	4	5	6	7	8	9	10
Mean [%]	60.9	28.2	13.4	6.8	3.5	1.9	1.1	0.6	0.3	0.2
Median [%]	67.1	20.4	13.2	0.5	0.0	0.0	0.0	0.0	0.0	0.0
Max [%]	99.9	99.8	99.7	99.7	99.6	99.5	99.0	60.7	44.3	36.2

Table 3.2: Percentage of data points for which the three-dimensional prostate displacement exceeds a specified threshold value in the whole data set.

Displacement [mm]	1	2	3	4	5	6	7	8	9	10
Fraction of data [%]	61.0	28.5	13.5	6.9	3.5	2.0	1.1	0.6	0.3	0.2

Table 3.3: Calculated CTV-to-PTV margins for different fraction times of 15 patients. This data is shown as part of fig. 3.10.

Duration [min]	1	2	3	4	5	6	7	8	9
Margin [mm]	1.0	1.4	1.9	2.2	2.5	2.8	3.0	3.3	3.5

der, while the median is 0.0 % for displacements larger 5 mm. As the maximum values show, single fractions can have large deviations, which can lead to strong dosimetric consequences, when not corrected for.

Summing up all fractions to one data set, 61 % of data points show a three-dimensional prostate displacement above 1 mm. This percentage decreases to 0.2 % for a displacement of 10 mm. All values are shown in table 3.2.

3.3.1.2 Margins for different treatment times

The margins determined for 15 patients are shown in table 3.3. The margin sizes calculated for 10 and 15 patients are almost the same, the values for 10 patients differ maximum 0.1 mm. In fig. 3.10, the trend over time is shown for the 15 patient analysis. Additional to the margin, the standard deviation of the systematic error Σ_d and the standard deviation of the random error σ_d of prostate displacement is displayed for each treatment time d. The standard deviation of the random error is always larger than the standard deviation of the systematic error. But after 3 min of treatment the systematic component dominates the margin size. This is due to the weighting in the margin calculation ($M_d = 2.5\Sigma_d + 0.7\sigma_d$) and the different slope of their time dependence. The margin increases almost linear in the analyzed time range: Beginning with 1 mm for 1 min until 3.5 mm for 9 min for each minute of treatment approximately 0.3 mm additional margin has to be considered.

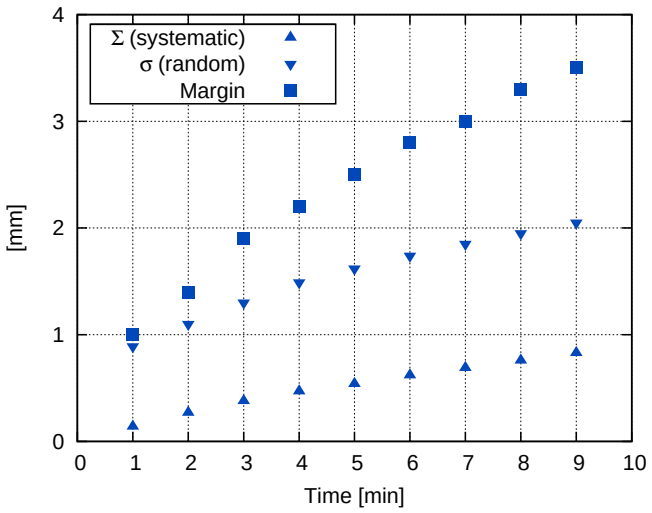

Figure 3.10: Treatment time dependence of the SD of the systematic and the random prostate displacement shown together with the resulting margin.

Table 3.4: Margins for both IGRT positioning methods and in combination with intrafraction motion for a fraction time of 9 min.

Scenario	Margin [mm]
Anatomic MV CBCT match, setup only	7.6
Marker based MV CBCT match, setup only	5.6
Intrafraction motion for 9 min	3.5
Anatomic MV CBCT match and intrafraction motion	8.6
Marker based MV CBCT match and intrafraction motion	6.8

3.3.1.3 Margins for IGRT positioning strategies

There can be large differences between image registration based on bony anatomy and markers in the prostate. This differences originate from prostate motion relative to the bone structure. An example of these deviations can be seen in fig. 3.11. There is shown an image fusion of a transversal slice of the planning CT and the corresponding slice of a fraction MVCT, after registration of the three beacons.

The derived isotropic CTV-to-PTV margins for the individual positioning methods are listed in table 3.4. A reduction of required margin size from 7.6 mm to 5.6 mm can be achieved by using fiducial markers in the prostate for image registration instead of the bony anatomy. Combining these setup margins with prostate displacements due to intrafraction motion for 9 min of treatment from section 3.3.1.2, by adding the corresponding Σ and σ quadratically, the resulting margins show an increase from 6.8 mm to 8.6 mm, when switching from marker based to bone based positioning.

The assumption of the Calypso position as ground truth does not take into account the motion occurring during the time gap between the acquisition of the MV CBCT and the

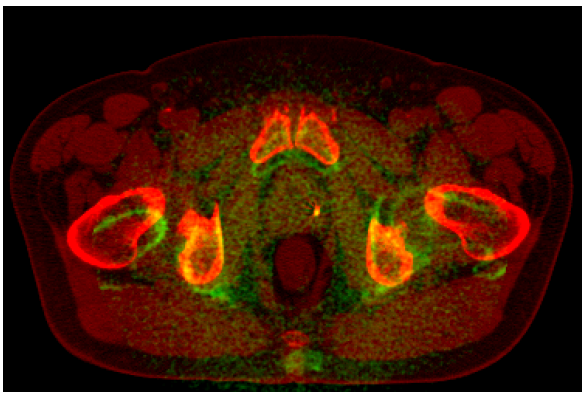

Figure 3.11: Planning kVCT (red) and position verification MVCT (green) fused after beacon match. All three beacons are aligned and the bones show large deviations. Only one of the beacons can be seen here.

Calypso localization. For this reason the given values are a combination of setup errors and approximately 5 min of motion, which is a realistic time difference between CT acquisition and start of therapy in IGRT as well.

3.3.2 Experimental validation of 4D dose reconstruction

3.3.2.1 Comparison of measured and calculated dose

The comparison between the moved films and the corresponding slices of the calculated 'moved' dose distributions using the target point shifting method shows a minimum 3 %/ 3 mm local γ-index of 91.4 %. Using the convolution methods the γ-indices for three patients are above 90 % too, but for the patient with the largest intrafraction motion they decrease to 89 %. Data for all patients can be found in table 3.5, where values for the static cases are additionally listed for comparison. As mentioned above, the best fitting transversal slice of the calculated dose distributions was determined from the target point shifted plans for the moved films. Using one of the convolution methods for the selection of the best fitting slices lead to a maximum deviation in slice coordinate of 0.5 mm. A comparison based on these slices does not change the ranking in calculation methods and increase the γ-indices obtained for the convolution methods below 0.2 %. Thereby the differences between γ-indices determined for adjacent slices are well below 0.3 % for the whole considered longitudinal region.

An example of dosimetric consequences which can occur from intrafraction motion is shown in fig. 3.12. The delivered monitor units for the phantom were the same as for the patient, leading to a maximum dose of 105 Gy in the phantom with a diameter of 20 cm. It can be seen that measured and calculated motion impacts on the dose are similar. For the absolute difference values, it has to be considered that the used corresponding slices of calculated dose distributions have a difference of 1.25 mm in the longitudinal coordinate, resulting from the search of best fitting plan slice, described in section 3.2.4.2. This leads to a combined effect of intrafraction motion and longitudinal dose gradients.

Table 3.5: 3 %/3 mm γ-indices for the comparisons between the calculated dose distributions and the corresponding films together with the mean prostate misplacement. The patient number P refers to the group of 21 patients used in the dose recalculation based on patient CTs and treatment plans.

P	Mean prostate misplacement [mm]	Whole data set convolution vs. Moved film [%]	Beam-on convolution vs. Moved film [%]	Target point shifted plan vs. Moved film [%]	Static plan vs. Static film [%]
2	1.7	95.6	95.8	96.3	96.3
3	1.4	93.1	93.6	93.4	94.5
6	1.1	94.0	94.0	94.8	98.6
7	2.8	89.2	89.6	91.4	94.1

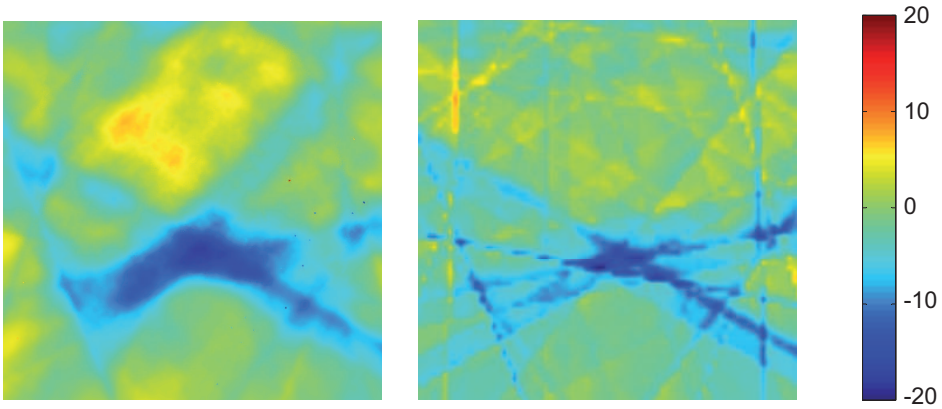

(a) (b)

Figure 3.12: Measurement: Difference between the moved and the scaled static film for patient 4 (a). Calculation: Difference between the corresponding transversal slices of the 'moved' plan (target point shifting method) and the static plan for patient 4 (b). The color map scale is in Gy for a maximum phantom plan dose of 105 Gy.

Table 3.6: γ-indices for the comparisons between the calculated dose distributions in the plan slices related to the moved films.

	Whole data set convolution vs. Beam-on convolution [%]		Target point shifted plan vs. Whole data set convolution [%]		Target point shifted plan vs. Beam-on convolution [%]	
Patient	3 %/3 mm	1 %/1 mm	3 %/3 mm	1 %/1 mm	3 %/3 mm	1 %/1 mm
1	100	100	100	95.5	100	96.1
2	100	99.1	100	93.7	100	96.1
3	100	100	100	91.7	100	89.0
4	100	100	99.6	77.5	99.5	77.9

3.3.2.2 Comparison of calculated dose distributions

The two convolution methods show no difference for the plan slices related to the films between each other beside a decrease to 99.1 % in one patient using a 1 %/1 mm local γ-index. All other 3 %/3 mm and 1 %/1 mm γ-indices are 100 %. The comparison between the plans recalculated with shifted target points and the convolution methods reach minimum 3 %/3 mm local γ-indices of 99.5 %. The differences between these methods in the homogeneous phantom get only visible when a 1 %/1 mm local γ-index is used. Then, the values range from 77.5 % to 96.1 %. All γ-indices are shown in table 3.6.

3.3.3 Dosimetric consequences on prostate IMRT

In the following section, results for the comparisons between the 'moved' and static fraction doses and cumulative doses for 21 patients are presented, they are summarized in table 3.7.

The mean prostate displacement was 1.7 mm in average, for single fractions it was up to 7.4 mm. [1]

The 3D γ-evaluation for the 'moved' fractions against the static ones resulted in an average γ-index of 83.6 %, with a minimum of 27.2 %. The γ-indices for all fractions are shown in fig. 3.13(a). Applying a plan acceptance criterion of a 3 %/3 mm γ-index of 90 %, only 154 of all 717 single fractions would pass (21.5 %). Combining single fractions to the cumulative dose distributions for each patient the average γ-index was 86.4 % with a minimum of 77.7 %.

[1] Additional to the geometrical mean a dose weighted mean prostate misplacement was calculated. For the dose weighted mean each segment's mean displacement was weighted with the product of the segment's field size and monitor units to account more for segments with more applied dose to the patient. There was no statistical difference between the geometrical mean and the dose weighted mean prostate misplacement, so all values in table 3.7 refer to both, even the range is the same. Calculating single fraction displacements, there were differences up to 0.4 mm between the two measures. For the cumulative values, the maximum difference is 0.1 mm. If these dose weighted mean prostate misplacements are used for correlation analysis, the changes in correlation coefficients are small, ranging from −1.1 % to 2.8 %.

Table 3.7: Results of the comparison between static plans and 'moved' dose distributions for single fractions and cumulative dose distributions per patient for 21 patients. r is Pearson's linear correlation coefficient between the dosimetric endpoint and the corresponding mean prostate misplacement. All correlations have p-values < 0.01.

	Mean ± SD	Range	r
Fraction mispl. [mm]	1.7 ± 1.0	(0.3, 7.4)	
Cum. mispl. [mm]	1.7 ± 0.5	(0.9, 2.8)	
Fraction γ-indices [%]	83.6 ± 9.3	(27.2, 96.8)	-0.94
Cum. γ-indices [%]	86.4 ± 4.6	(77.7, 94.7)	-0.88
Fraction boost $D_{95\,\%}$ [%]	-0.9 ± 2.1	(-26.7, 1.8)	-0.68
Cum. boost $D_{95\,\%}$ [%]	-0.3 ± 1.1	(-4.4, 0.7)	-0.72
Fraction PTV $D_{95\,\%}$ [%]	-2.0 ± 3.4	(-24.9, 2.4)	-0.82
Cum. PTV $D_{95\,\%}$ [%]	-1.2 ± 1.5	(-4.2, 1.4)	-0.72

The cumulative dose distributions for 6 of 21 patients pass the 90 % criterion. Data for all patients can be seen in fig. 3.13(b).

The change in $D_{95\,\%}$ of the boost volume for single fractions was on average $-0.9\,\%$ with a maximum change of $-26.7\,\%$. For the PTV these values are $-2.0\,\%$ and $-24.9\,\%$. Values for all fractions are shown in figs. 3.13(c) and 3.13(e). A change of $D_{95\,\%}$ of the boost volume of more than 1, 3 and 5 % occurred in 32.1, 7.1 and 3.6 % of all fractions, respectively. The corresponding PTV data are 50.2, 19.9 and 9.9 %. Combining single fractions to the cumulative dose distributions for each patient the change in $D_{95\,\%}$ of the boost volume was on average $-0.3\,\%$ with a maximum change of $-4.4\,\%$. The cumulative dose distributions lead to a mean change in $D_{95\,\%}$ of the PTV of $-1.2\,\%$ with $-4.2\,\%$ maximum change. Data for all patients can be seen in figs. 3.13(d) and 3.13(f). The change of $D_{95\,\%}$ of the PTV for the cumulative dose distributions were larger than 1, 3 and 5 % for 10, 4 and 0 patients, respectively. For the boost volume these values are reduced to 2, 1 and 0 patients.

Analyzing the correlation between motion amount and change in dose distribution, best correlation ($r = -0.94$) was reached by the single fraction γ-index. For the single fraction evaluation of the change of $D_{95\,\%}$ of the boost volume and the PTV the correlation was smaller with correlation coefficients of -0.68 and -0.82. For the cumulative dose distributions these values are -0.88, -0.72 and -0.72.

Correlating the change in $D_{95\,\%}$ of the PTV and the boost volume lead to correlation coefficients of 0.78 for the single fraction doses and of 0.65 for the cumulative dose distributions (both have p-values < 0.01). The linear regression between these parameters show a slope of 0.47 to 0.48, representing an effect in the boost volume of about one half compared to the PTV. All data for the comparison of boost volume and PTV change in $D_{95\,\%}$ are shown in fig. 3.14. As indicated, we observed that for one patient the boost volume change is larger as for the PTV, see fig. 3.14(b). 11 of the 12 fractions with a boost volume $D_{95\,\%}$ change of more than 8 % depicted in fig. 3.14(a) belong to this patient. It is the one with the largest amount of motion observed. Furthermore, the posterior margin for this patient was reduced to about 3 mm during the planning process instead of the general margin concept of an isotropic 7 mm boost-to-PTV margin.

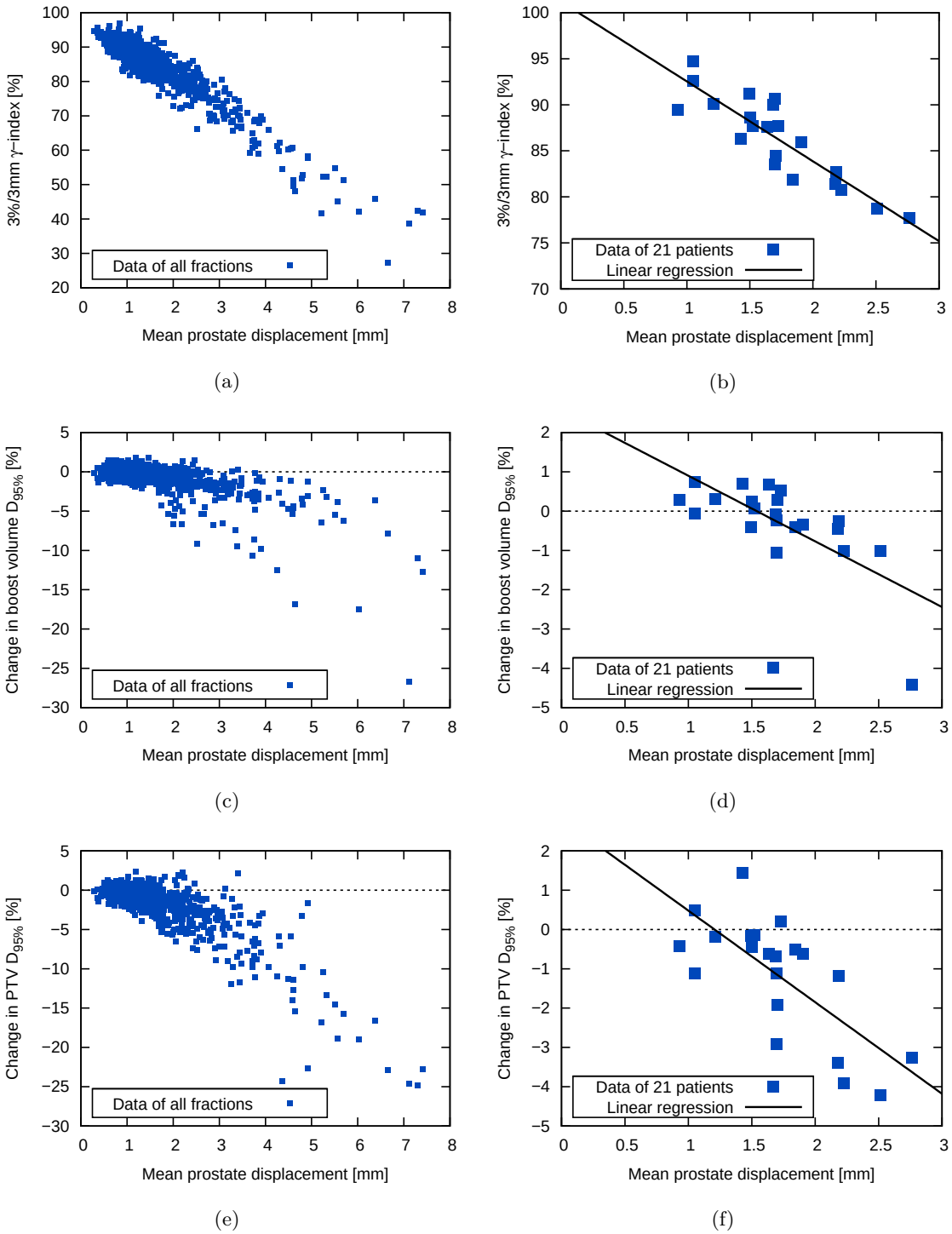

Figure 3.13: Results of the dose comparisons for single fraction plans (a,c,e) and cumulative plans for whole treatment courses (b,d,f).

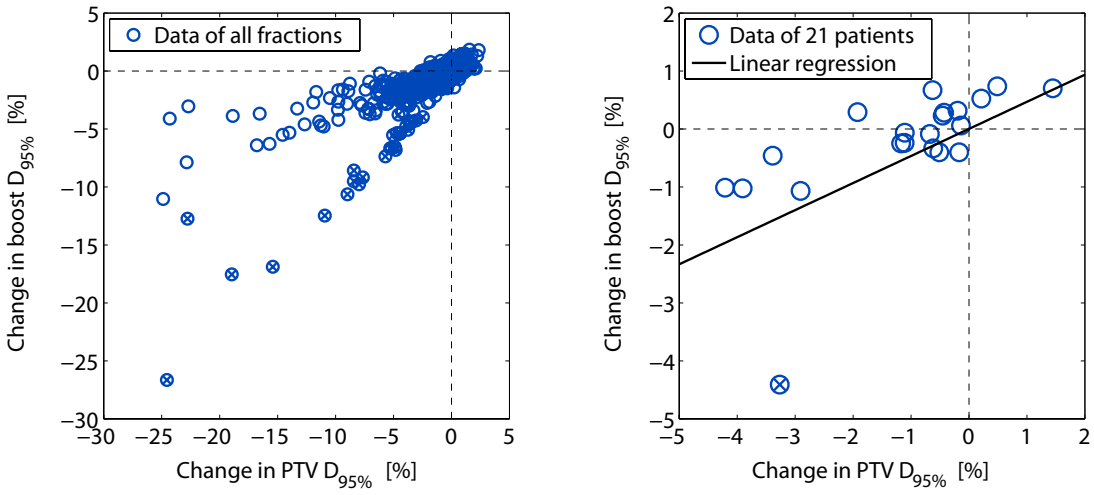

(a) (b)

Figure 3.14: Change in $D_{95\,\%}$ of the boost volume plotted against the change in the PTV for all fractions (a) and for the cumulative patient plans (b). All data points of the patient, for which the cumulative change in PTV $D_{95\,\%}$ is smaller than in the boost volume are marked with a cross.

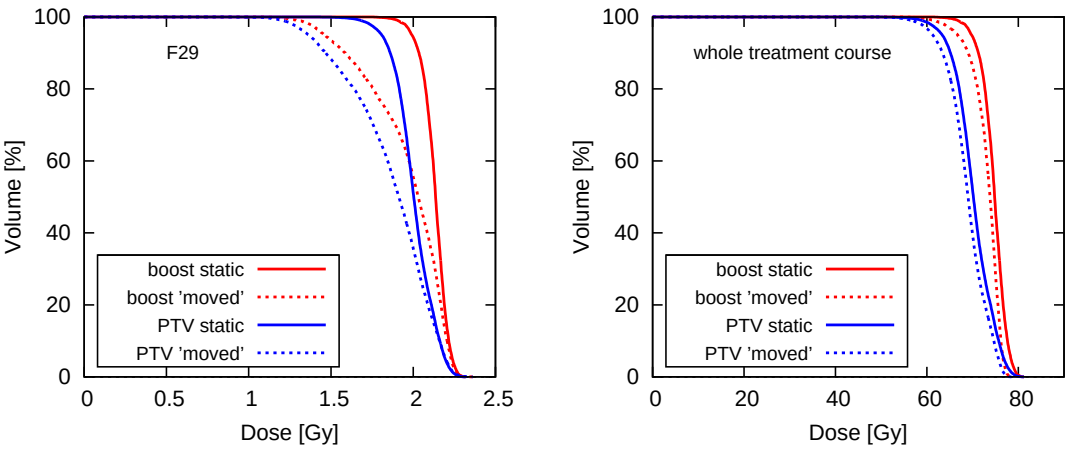

(a) (b)

Figure 3.15: Cumulative dose volume histograms for the boost volume and the PTV for the patient with the largest amount of motion. The static cases are shown together with the 'moved' dose distributions. For fraction 29, the outlier in fig. 3.14(a), large perturbations can be seen (a). While the effects for the whole treatment course are much smaller (b).

To illustrate the dosimetric effect in this pre-mentioned patient with the largest motion amount, cumulative dose volume histograms (dvh) are shown in fig. 3.15 for the single fraction with the strongest dose perturbation and for the whole treatment course.

3.4 Discussion

3.4.1 Quantification of prostate motion and its impact on margin sizes

The intrafractional motion patterns containing drifts and spikes in longitudinal and vertical direction reported here are in agreement with published data (Kupelian et al., 2007; Langen et al., 2008b). The overall motion amount from these individual fraction shapes is determined for all three directions and in 3D. Comparing the unidirectional analysis with data from (Li et al., 2008a) for 35 patients a more stable mean position over time for longitudinal and vertical direction is reported there with deviations about 0.4 mm in inferior and posterior direction after 9 min of treatment without clear trend in time. While here the mean inferior and posterior deviation after 9 min is 0.9 mm and 0.8 mm with a clear trend. The standard deviations after 9 min around these means show similar sizes with lateral, longitudinal and vertical values of 0.7, 1.6 and 2.0 mm in (Li et al., 2008a) and 1.0, 1.9 and 2.0 mm here. The analysis of three-dimensional prostate displacement in terms of percentage of time, a given value is exceeded per fraction can be compared by data of 17 patient in (Langen et al., 2008b). The mean values reported there for displacements above 3, 5, 7 and 10 mm, are 13.2, 3.1, 0.8 and 0.0 %, respectively. They are only slightly smaller than the ones reported here with 13.4, 3.5, 1.1 and 0.2 %. The median values for the same displacements are 13.2, 0.0, 0.0 and 0.0 % in this thesis, the values reported in (Langen et al., 2008b) (1.4, 0.0, 0.0 and 0.0 %) show a positively skewed distribution with a much larger proportion of fractions with only a few points in time exceeding the 3 mm.

The CTV-to-PTV margins derived from the patient's intrafractional prostate motion can be compared with two analysis (Tanyi et al., 2010; Li et al., 2013) in which the Calypso System is used for motion monitoring as well. In (Tanyi et al., 2010) treatments of 14 patients with fraction times between 8 and 16 min are evaluated without differentiation between different treatment times. From the data of their analysis a three-dimensional margin of 3.8 mm can be calculated. Our evaluation results in a margin of 3.5 mm for 9 min of treatment. Considering the unclear distribution of fraction times in the mentioned time interval for (Tanyi et al., 2010), these values are in good agreement. An analysis regarding time trends in margin sizes is presented in (Li et al., 2013). They used data from 105 patients with treatment times ranging from 8.1 min to 24 min with a median of 11.5 min. From their data margins of 1.6 and 1.7 mm for 3 and 5 min of treatment can be calculated. The corresponding values for our patient data are 1.9 and 2.5 mm, which shows a much larger increase in time. Li et al. additionally reported on a saturation in margin size after 9 min of treatment, which can not be analyzed with our data.

Most published evaluations of the difference in patient positioning strategies based on image registration using bony anatomy or implanted fiducial markers using the marker based registration as ground truth prostate position, e.g. (Nederveen et al., 2003; Langen et al., 2005). Because of that, they are not suitable for comparison with the data presented here.

In this thesis the Calypso localization serves as ground truth for both methods. This is also the case for an analysis in (Tanyi et al., 2010), where daily kV cone beam CT data sets are used for image registration with the planning CT. The marker based image registration leads to a 3D margin of 4.2 mm for the data published by Tanyi et al. and 5.6 mm in our case. For the image registration based on bony anatomy the difference is much larger with a value of 13.6 mm for Tanyi et al. and 7.6 mm for our patient data. Between the two reports, there are two differences beyond the imaging technique (kV versus MV CBCT): first, a larger slice thickness of the kV CBCT in Tanyi et al. (2.5 mm compared to 0.54 mm) and second, the consideration of the pelvis in the bony anatomy match, only for Tanyi et al. while in our evaluation the whole bone structure is considered. The enlarged slice thickness can lead to a larger uncertainty in transponder position detection. While the difference in bone matching should lead to a better result for Tanyi et al. in principal, because a better correlation between pelvic and prostate position than on whole bone structure and prostate position can be assumed. This is because the femoral heads can be in another position relative to the pelvis in both image sets, which complicates the registration procedure. These results allow for the conclusion, that the interfractional bone-prostate relation is more stable in our patient cohort than in the one used in (Tanyi et al., 2010). The origin of this difference between the patient cohorts is unknown, Tanyi et al. does not report information about a dietary protocol or some details about the weight or the general conditions of the patients.

For application of CTV-to-PTV margins in clinical practice, some points have to be considered.

First, beside the requirement to be large enough to enable curative dose to the target volume, the margin should be as small as possible to guarantee best dose sparing of the organs at risk. The patient subjective reduction in side effects due to smaller margins is shown in a trial with patient setup using the Calypso System and therefore reduced margins (Sandler et al., 2010).

Second, all reported margins in this chapter account for patient positioning or intrafractional motion, only. Other geometrical uncertainties, e.g. from the treatment machine or target delineation have to be assessed additionally. The resulting applied margins in clinical practice are of the same size as the margins calculated here for compensation of inter- and intrafractional motion, only. As described in section 3.2.1, the margin concept at the dkfz is an integrated boost concept with a 7 mm low dose margin. Other authors report the following values for classic isotropic CTV-to-PTV margins with a reduction in posterior direction to reduce rectal toxicity: 7 mm overall with 4 mm posterior margin in (Tanyi et al., 2010), 10 mm overall margin with a reduction to 7 mm in posterior direction in (Thongphiew et al., 2009) and 8 mm overall margin with 5 mm posterior margin in (Huang et al., 2002).

Third, there are some publications arguing that CTV-to-PTV margins according to the recipe proposed by van Herk et al. which is used here, are larger than necessary. One reason is the assumption made by van Herk, that the prescribed dose is shaped accurately and with very steep dose gradients around the PTV. This assumption is not fulfilled for overlapping beams from multiple angles (McKenzie et al., 2000), under these conditions a slightly blurred dose distribution is delivered, which acts as an additional margin. This results in the need of a smaller factor for the random component of the margin recipe. Another publication conclude the overestimation of margins with the van Herk formula even in the presence of additional deformation and rotation of the prostate (Mutanga et al.,

2011). Ballhausen et al. proposed a higher order correction for the Gaussian approach used to describe time dependent random errors in van Herks margin recipe (Ballhausen et al., 2013). They assume a random walk model of intrafractional prostate motion, which is shown to be consistent with empirical data. This random walk model leads to a Gaussian distribution of displacement in any direction for every point in time with varying mean and increasing standard deviation over time. Calculating the fraction average displacement distribution results not in another Gaussian distribution but in a Brownian distribution. A Brownian distribution has a steeper, narrower shape as a Gaussian distribution with the same variance. The incorporation of this correction in van Herks margin recipe leads to a reduction of the random component of CTV-to-PTV margins for compensation of intrafractional motion of about 30 %.

3.4.2 4D dose accumulation

Dose reconstruction using a convolution of the static dose distribution with a probability density function (pdf) of the target position is a known method (Lujan et al., 1999; McCarter and Beckham, 2000). To account for interplay effects between patient motion and leaf or gantry motion, this pdf can be applied per IMRT segment or per beam instead of using the data of the whole treatment (Li et al., 2008a,b; Adamson et al., 2011). Even the problem of tissue inhomogeneities (Craig et al., 2003a) in the patient is sometimes avoided by a convolution of the fluence maps before the dose calculation instead of the dose convolution (Beckham et al., 2002). But all these approaches lead to statistical uncertainties in dose estimation due to the finite number of data points in the pdf (Craig et al., 2003b), especially, if the convolution is performed segment-wise. In this thesis the two convolution methods were used to evaluate a possible difference in motion systematic between beam-on phases and beam breaks and to quantify the interplay effects through the comparison with the target point shifting method.

Approaches without convolution methods use different concepts of motion consideration. For example, in a calculation where the prostate is translated and rotated in a static dose cloud (Noel et al., 2010), which makes the assumption that only the prostate is moving in a rigid body frame. Another possibility is to treat the whole patient as rigidly moving together with the prostate, like in the method by Waghorn et al. (Waghorn et al., 2010). There, the fluence maps were exported from the treatment planning system and shifted accordingly to the prostate misalignment per monitor unit. The re-imported fluence maps were then used for dose calculation on the static CT.

Our calculation methods for 'moved' dose distributions assume a rigid patient, too. Thus, our dose distributions are an estimate whose agreement with the real delivered dose will differ from patient to patient. Using the Calypso System, no information is available about the relative motion of prostate and bony anatomy or seminal vesicles. The prostate shifts detected by the Calypso System were used as shifts of the whole rigid patient, this leads to some limitations of the calculation methods, which are discussed in the following. First, shifts between the bony anatomy and the prostate are not accounted for. (Palombarini et al., 2012) studied these shifts by a comparison of bone registration and soft-tissue registration of daily kV CBCT and planning CT in 18 patients. Considerable deviations were found in AP direction, namely 2.7 mm systematic and 2.8 mm random variation. Second, in our large

PTV margin, the base of the seminal vesicles is included as target, so it is arguable how they move relative to the prostate. Third, the effects of prostate rotations and deformations by physiological processes has to be viewed. (van der Wielen et al., 2008) evaluated data of 21 prostate patients with implanted fiducial markers, receiving four CT scans each. They reported on residual deviations of the prostate ($\leq$ 1.3 mm) and the seminal vesicles ($\leq$ 3.4 mm) using only translations for image registrations between the first and the following CTs, originating in deformations and rotations. These deviations describe the interfraction changes, so it can be assumed, that the intrafraction changes are much smaller. This data refer to the whole seminal vesicles, we consider only their base, so the effect will be even smaller. Altogether it can be assumed, that the dose estimation is best for the smallest amount of motion. This should be considered when looking at results for fractions with a large amount of motion. Whether these factors lead to an over or under estimation of the effect of intrafraction motion in general is not clear, this depends on the individual patients anatomy.

3.4.2.1 Experimental validation of 4D dose reconstruction

It has been demonstrated that the method of shifting the target point for every segment in a recalculation of the static plan is well suited to calculate 'moved' dose distributions. 3 %/3 mm local γ-indices above 90 % were achieved in comparison with measured doses for all considered patients. For comparison, we performed a convolution of the static dose with two different pdfs containing either all Calypso motion data or only the motion data during the beam-on phases. These method leads to good results, too (minimum 3 %/3 mm local γ-index of 89 % against the moved films).

The validation of calculation methods for 'moved' dose distributions are managed differently in the literature. For the comparison other calculation methods (McCarter and Beckham, 2000; Noel et al., 2010) or measurements (McCarter and Beckham, 2000; Waghorn et al., 2010) can be used. Inter-calculation comparisons have the potential to lead to a better result than validations incorporating measurements, bringing in additional uncertainties like phantom positioning and beam modeling in the calculation. Waghorn et al. reported a minimum 3 %/3 mm γ-index of 97.4 % for comparisons between film measurements and their calculation method of shifting the fluence maps according to phantom motion prior to dose calculation. This is larger than our minimum value for the target point shifting method (91.4 %), but the conditions of the measurements are also different. We irradiated whole treatment courses containing 35 fractions on one film and used measured patient motion. The film measurements in (Waghorn et al., 2010) are based on artificial sinusoidal motion and a dose equivalent of one fraction. In that way, our measurements each lasting more than 6 h are much more prone to accumulate small positioning errors and errors because of an unperfect synchronization between radiation and phantom motion.

The two convolution methods agree much better when compared to the target point shifting method. This shows the impact of interplay effects between patient motion and gantry and MLC motion, which is not considered by our convolution methods. The differences between dose distributions calculated with the two different convolution methods are very small. One of them considers the irradiation pauses and the other does not, this allow for the conclusion,

that the motion patterns in irradiation pauses are not mainly different from them during the irradiation.

We decided to use the target point shifting method for the evaluation of dosimetric effects of intrafraction motion in the analysis based on patient CT data. Besides the slightly better validation results, this has two reasons, first this method accounts for interplay effects between patient motion and beam delivery dynamics and second even with a pencil beam algorithm for dose calculation used here, the heterogeneous patient anatomy should be considered more explicitly than in convolution of a static dose cloud.

The presented dose recalculation tool of shifting the target point for every IMRT segment can also be used to evaluate and compare different margin sizes and dose prescription concepts using realistic patient motion patterns considering different approaches of adaptive radiotherapy.

3.4.2.2 Dosimetric consequences on prostate IMRT

The calculation of 'moved' dose distributions for single fraction plans and cumulative dose distributions representing a whole treatment course shows four main results: 1) In some fractions, large changes in dose are induced by intrafractional motion. This is consistent with other publications (Li et al., 2008a; Langen et al., 2009, 2012). 2) A fractionation with 35 fractions reduce this effect considerable, as can be expected from theoretical assumptions (Bortfeld et al., 2002). 3) The boost volume is in average much less effected than the PTV, which has to be expected and justifies the margin concept. 4) Correlation between motion amount and dose deviation is strong using the three-dimensional 3 %/3 mm γ-index, but decreases using the volume specific change in $D_{95\,\%}$.

To discuss our results in detail, we compare them with (Langen et al., 2012) in which dose recalculations for prostate patients for seven field step-and-shoot IMRT irradiations were done by shifting the fluence maps before dose calculation. They used plans with a classic CTV and PTV concept with a 5 mm CTV-to-PTV margin with exception of a posterior margin of only 3 mm. A comparison of margin concepts can be seen in fig. 3.16. In both concepts, there is an 'inner volume' and an 'outer volume', these are boost and PTV for this work and CTV and PTV for Langen et al. The motion data used by Langen et al. was the same as in another publication of the same group (Langen et al., 2008a). The amount of time the prostate misplacement exceeds 3, 5, 7 and 10 mm mentioned there is only slightly smaller than in our data. Due to that, the comparison of the dosimetric effect determined by them with the ones found in this work, can be used to evaluate dose sensitivity against intrafraction motion for both irradiation concepts (classic CTV-PTV and integrated boost). The reported dose effects using the change of $D_{95\,\%}$ in inner volume and PTV are smaller than ours, both for single fraction plans and for cumulative plans. They report on maximum single fraction deviations in the CTV and PTV of up to $-6.4\,\%$ and $-12.7\,\%$, while the values are $-26.7\,\%$ and $-24.9\,\%$ for our boost volume and PTV. The comparison of mean values and standard deviations is shown in table 3.8. In general, their average effects in single fractions and cumulative dose distributions are smaller than ours. The largest discussed dose perturbation is calculated for our PTV. This is constructed as a region of two dose levels with a high-dose volume in the middle, which complicates a comparison to the other

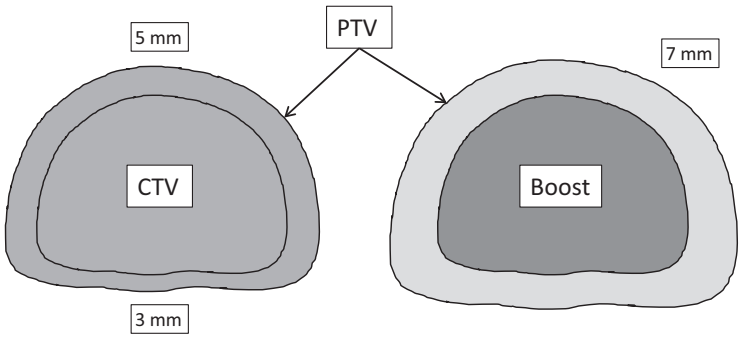

Figure 3.16: Margin concept used in (Langen et al., 2012) (left) with 3 mm posterior and 5 mm elsewhere and in this work (right) with 7 mm isotrop. Gray values indicate relative levels of prescribed dose per concept: The same prescribed dose for CTV and PTV (left) and a higher dose in the boost, than in the PTV (right). CTV and boost volume are later referred to as 'inner volume'.

Table 3.8: Comparison of the change of $D_{95\,\%}$ in different volumes. The cumulative dose distributions sum up 25 fractions in (Langen et al., 2012) and 35 fractions in this report. Inner vol. serves as abbreviation for CTV and boost volume for both studies, respectively.

Dosimetric endpoint	(Langen et al., 2012) Mean ± SD [%]	This report Mean ± SD [%]
Fraction inner vol. $D_{95\,\%}$	-0.2 ± 0.5	-0.9 ± 2.1
Cum. inner vol. $D_{95\,\%}$	0.1 ± 0.2	-0.3 ± 1.1
Fraction PTV $D_{95\,\%}$	-0.5 ± 1.1	-2.0 ± 3.4
Cum. PTV $D_{95\,\%}$	-0.2 ± 0.2	-1.2 ± 1.5

volumes. The differences in PTV effects can be illustrated by looking at the percentage of fractions, in which the PTV $D_{95\,\%}$ is altered by more than 1, 3 and 5 %. In the current report, the values are 50.2, 19.9 and 9.9 %, in the report by Langen et al. they are 12, 2.5 and 0.8 %.

Studying the correlations between motion amount and dose perturbation, high correlation coefficients were found using the three-dimensional γ-index as dosimetric endpoint (-0.94 for single fractions and -0.88 for cumulative plans). For correlation comparison with (Langen et al., 2012), the correlations with the geometric mean displacement were used for both studies. Correlation data are published for single fraction evaluations only. The change in $D_{95\,\%}$ of the PTV is better correlated to the motion amount than the change in $D_{95\,\%}$ of the inner volume, for both investigations. A decrease in correlation coefficients from -0.7 to -0.26 is reported there and our calculations give -0.82 and -0.68. In this comparison another important point can be anticipated. This is the correlation of $D_{95\,\%}$ change in the PTV with the change in $D_{95\,\%}$ of the inner volume. The single fraction changes in $D_{95\,\%}$ of CTV and PTV in (Langen et al., 2012) have a poor correlation coefficient of $+0.53$, which is together with the smaller change in the $D_{95\,\%}$ of the CTV a reason to say that their margin protects the CTV properly against motion caused perturbation. In our case the correlation between the changes in the PTV and the boost volume is stronger (r=+0.78). This is

an effect of the lower dose in our margin. Depending on the dose gradient between boost volume and PTV, almost all motion has influence on the PTV and the boost volume. There is no threshold for the boost volume, like in a classic CTV-to-PTV margin concept. The change in the boost volume are on average half of them in the PTV or lower, so this margin concept, using a large margin with less dose, is also appropriate for protecting the inner volume. But it has to be noted, that the dkfz margin concept was developed for a therapy using MV CBCT based patient setup, which leads to additional uncertainties, while the current investigation assumes intrafractional motion only. When considering interfraction motion in addition, the deviations between planned and recalculated dose distributions are expected to be larger.

There is one patient in our analysis, for whom the effects in the boost volume are remarkable and even larger than in the PTV. This is possible because of the integrated boost concept, where for the PTV motion a higher dose in the voxels near the boost volume can compensate lower dose near the normal tissue in the calculation of the $D_{95\,\%}$. It has to be kept in mind that this patient is the one with the largest amount of motion and therefore the assumption of a rigid patient leads to the largest effect of calculation uncertainty.

We used a fractionation scheme with 35 fractions, this leads to a much smaller motion induced perturbation of the dose distribution in the cumulative dose, than in the single fractions. Hypofractionation for prostate carcinomas is discussed and used for some time, especially because of the radiobiology of prostate tumors (Madsen et al., 2007; Ritter et al., 2009). Such a treatment scenario has two characteristics: less number of fractions and an increased treatment time per fraction. Both can lead to a larger effect of intrafraction motion on the dose distribution. The less number of fractions will lead to a smaller interfractional averaging effect. The increased fraction time can have two opposing effects. First some dose perturbation will be averaged out, like due to many fractions. But second, potential longitudinal and vertical prostate drifts can result in an increased prostate displacement at the end of each fraction, if no repositioning procedure is performed during the fraction. The increase of motion amount with fraction time was shown for a subset of our patient data for durations between 2 and 9 min in section 3.3.1.2.

4 Motion monitoring in lung radiotherapy: Challenges and chances

Electromagnetic tracking offers the possibility to monitor three-dimensional lung tumor motion continuously in real-time during radiation therapy without additional imaging dose for the first time and without the need of a special treatment device. In this chapter the investigations we made as part of the first trial evaluating the clinical use of the anchored Calypso beacons for lung tumor patients are presented. They regard the intrafraction motion and interfractional changes of it. No evaluation of setup accuracy was made, as the system was not used for patient positioning in this trial. In a first part we targeted on quantification of the motion reported for the transponder centroid, secondly the relative motion of implanted transponders during fractions and changes of the transponder geometry over the whole course of treatment were determined to proof the underlying assumption of a stable transponder geometry. In a third part the correlation between the intrafraction motion measured with the Calypso System and the Anzai belt was evaluated, thereby only the transponder centroid motion was used.

Parts of the following investigations were presented at scientific conferences (Schmitt et al., 2013a,b).

4.1 Clinical background and purpose

With a proportion of 7.0 % and 13.8 % of all newly detected cancers, lung cancer is for both women and men the third most common cancer in Germany. In absolute values about 15600 women and 34000 men were diagnosed with lung cancer in 2008. The mean age at diagnosis is 68 and 69 years for women and men, respectively. The relative 5-year survival rates are rather poor with 19 % for women and 15 % for men. This leads to deaths caused by lung cancer of nearly 13000 in women and 30000 in men in Germany in 2008, denoting the third most cancer deaths for women and the first rank in cancer deaths in men. In the last few years, an increase has been seen in lung cancer in women and a decrease in men, which is usually explained by an equalization of smoking behavior in both sexes. (RKI, 2012)

Radiotherapy is one option of curative therapy for lung cancer patients. All patients enrolled in our lung study were diagnosed with non-small cell lung cancer (NSCLC). In early stages of this disease surgery provides best outcome and is thereby first choice, possibly in combination with chemotherapy. A radiotherapy is only performed if the tumor is inoperable, or if the surgical resection was incomplete. In later stages treatment regimens combining chemotherapy, surgery and radiotherapy or chemotherapy and radiotherapy are applied. (Hansen and Roach III, 2010; Oertel et al., 2010)

Lung tumor motion is mainly induced by respiration and due to that not avoidable, this leads to the need of dedicated managing techniques for the intrafractional as well as the interfractional motion. These techniques rise the ability to tailor the irradiation fields more precisely to the target volume (smaller margins). Therefore the volume of healthy tissue, receiving high irradiation doses can be reduced. This volume reduction offers the opportunity to increase the dose to the tumor, while the side effects due to irradiation of healthy lung tissue remain acceptable (Nelson et al., 2006). Higher radiation dose to the tumor has shown to enlarge the local tumor control and the overal survival time for NSCLC patients (Kong et al., 2005).

The intrafractional motion is dominated by the approximately periodic breathing motion around a mean position, here called midline. Additionally the amplitude can vary during the fraction and the midline position can change over time, e.g. periodically or as a drift. The interfractional motion can have different aspects, too. For example the tumor midline position and motion amplitude can change from day to day typically due to different organ filings, e.g. of the stomach or from treatment related changes in anatomy or lung function. Some of these changes can be compensated for by the daily patient positioning procedure if the tumor position relative to the organs at risk has changed only slightly. While other interfractional changes like extensive tumor shrinkage can only be regarded through a replanning process.

There are several devices available for patient positioning and intrafractional detection of breathing motion, see section 2.2.2. Many of these detection devices use an external surrogate, like motion of the chest wall instead of the tumor motion. As shown by (Korreman et al., 2008), it is not possible to use smaller margins in gated therapy than in ungated when the gating information is based on an external breathing signal, only. It is concluded that internal tumor motion has to be monitored because of shifts in the tumor baseline (i.e. tumor position at end of exhale) and phase shifts between external and internal motion. All established methods for detection of internal lung tumor motion are based on imaging with the treatment beam or give an additional imaging dose to the patient. This often requires implantation of fiducial markers for reliable and fast motion detection. For this marker implantation several methods are developed in the last years, the standard approach is the percoutanuos implantation under CT guidance, like described by (Whyte et al., 2003), which has the drawback of a risk of pneumothorax of up to 45 % (Kothary et al., 2009).

With the development of new Calypso transponders for the use in lung radiotherapy, see section 2.2.2.2, Varian provides the first system for electromagnetic tumor tracking for lung cancer patients. These transponders are implanted via a standard bronchoscope. To bring each transponder as close to the tumor as possible, the catheter with the transponder exits the bronchoscope under continuous X-ray guidance to deposit it in a small airway.

In this chapter real-time 3D motion data acquired with the Calypso System was quantified enabling a comparison with image guided methods. The continuous 3D data of up to 30 fractions also allows for evaluations of the tumor midline and motion comparison between fractions.

For treatment techniques, using an active tracking of the tumor (either moving the beam or the patient) usually a prediction of future tumor position from actual position is necessary because of system latencies. The quality of this prediction increases the more regular the

motion is. To get an impression on this regularity over single treatment fractions, data from two patients are analyzed in consecutive time intervals. Thereby the focus is on differences between beam-on phases and beam breaks.

For image guided marker based motion management often more than one marker is implanted for better geometric reliability, e.g. (Shirato et al., 2003). These techniques usually assume a rigid patient geometry in the analyzed region. When the Calypso System is used in clinical routine, the centroid motion is the information which is available for online intervention during the therapy, also assuming a stable transponder geometry during the irradiation and over the whole course of treatment. Quantifications of deviations from this assumption are rare, some evaluations of interfractional transponder distance changes are made for hypofractionated therapy (Imura et al., 2005; van der Voort van Zyp et al., 2011). However, especially for conventionally fractionated therapy over several weeks, a decrease in tumor volume has to be expected. This decrease in tumor volume influences the geometry of the surrounding tissue and hence the transponder geometry and therefore questions the reliability of the centroid position as surrogate for the tumor position. Reported values are e.g. a median GTV regression of 41.7 % measured with weekly 4D CTs in eight patients over six weeks on average (Britton et al., 2007) and a mean shrinkage of the primary GTV of 1.2 % per day determined for 10 patients using the TomoTherapy MVCT (Kupelian et al., 2005). To our knowledge no analysis of continuous intrafraction data on inter-marker distances is published so far. In this chapter the inter- and intrafractional variability of inter-marker distances are investigated for three markers outside the tumor, detected continuously with the Calypso System. The amount of deformation in the tissue of the upper lung is evaluated considering two aspects of transponder geometry variations: 1) due to intrafraction breathing motion and 2) interfractional changes because of radiation effects in the normal lung tissue and tumor shrinkage.

When external surrogate motion is used for motion management in lung radiotherapy, the robustness of the relation between this external signal and the tumor motion itself is one main point that has to be assigned individually for each external surrogate method. Here the correlation between the changes in chest circumference due to breathing and the three-dimensional motion of the beacon centroid was assessed.

4.2 Material and methods

4.2.1 Patient data

The lung patient data used in this thesis was collected during a multi-center trial for the evaluation of anchored Calypso beacons organized by Varian Medical Systems, Inc. This trial was approved by the ethics committee of the medical faculty of the University of Heidelberg (approval number MZmu-026/2011) and has the title “Evaluating an anchored transponder in lung cancer patients receiving radiation therapy”. The main objectives of this study are the evaluation of the implantation procedure, position stability of the anchored beacons over time and ability of the Calypso System to detect the beacons properly. All of these evaluations will be done by Varian Medical Systems Inc. The investigations presented in this thesis are additional work (also covered by the approval) using the collected data.

The trial cohort contains seven patients, four of them with an upper lobe tumor and three with a right middle lobe tumor, two got an additional chemotherapy, one before and one concurrently to the radiotherapy.

The patient treatment was organized as part of a collaboration between the dkfz and the Thoraxklinik at the University of Heidelberg. For all participants of this study, the implantation of the anchored Calypso beacons was performed at the Thoraxklinik bronchoscopically. The treatment planning and the radiotherapy were done at the dkfz. For treatment planning several CT data sets were acquired: a kV 4D CT scan, a kV CT scan under free breathing conditions and a kV CT scan in maximum exhale breath-hold position. The dose prescription and calculation was done on the free-breathing CT, the other CT data sets deliver information for defining the ITV. For the treatment two different schemes are applied, either a hypofractionated 3D conformal therapy with six beam angles and 10 fractions per patient (for two patients in an early tumor stage without affected lymph nodes), or a step-and-shoot IMRT with eight or nine beams in 30 fractions (for five patients). All of these beam angles were coplanar. Prior to each fraction, a cone beam CT was acquired. For the first 6 patients, this was an MV CBCT, for the last patient kV CBCTs were used after the integration of a kV cone beam CT system at the Siemens Artiste gantry. The patients were positioned according to the shift vector, determined between the daily CBCT data set and the planning free-breathing CT. After the positioning was completed, the treatment was performed during continuous motion monitoring with the Calypso System. The aforementioned set of CT image data, used for planning, was repeatedly acquired for every patient once a week during treatment for control issues. Additional to the trial parts planned by Varian, we had the opportunity to measure respiratory motion externally with the Anzai chest belt (see section 2.2.2.3) for three patients.

Depending on the analysis, the following patient related data was used: I) kV 4D planning and control CTs, II) Calypso motion data including beam status report and III) respiratory signal, detected by the Anzai system.

4.2.2 Motion quantification

In this part of the investigation data from all seven lung patients was used. The fraction data used from both fractionation schemes are the following: 20 fractions with a mean duration from start of first beam until end of last beam of 4.5 min for the hypofractionated patients and 142 fractions with a more than doubled mean duration of 9.6 min for the IMRT patients. The determination of the breathing frequency was only feasible for five patients, see section 4.2.2.2.

4.2.2.1 Overall displacement, midline changes and motion amplitude

All calculations were made for the unidirectional components and for the absolute value r of the 3D positions, which is used in the following equations. First, a midline M_t of the detected motion was calculated for each point in time t by a sliding mean of the positions

r with a window width of 10 s, consisting of the data point r_t itself and the 50 positions before and afterwards:

$$M_t = \frac{1}{101} \sum_{i=t-50}^{t+50} r_i. \tag{4.1}$$

This 10 s window covers approximately 2–4 breathing cycles. Motion analysis is made only for the time between the start of the first beam and the end of the last beam. Only for the midline determination, position data for the 5 s before and after this time interval was used. The midline at the time irradiation starts t_s for each fraction f is called initial midline M^f_{inital} of this fraction, $M^f_{\text{initial}} = M^f_{t=t_s}$.

The intrafractional centroid displacement $r^f_{\text{intra},t}$ was calculated for each point in time of each fraction relative to this initial midline as shown in eq. (4.2a). All fractions F per patient were put together to calculate a mean and standard deviation of this overall intrafractional centroid displacement. The equation for the mean is shown in eq. (4.2b). Thereby each fraction f has a total number of data points T^f from start t_s to the end of irradiation t_e. This measure represents the motion that has to be compensated if the patient would be positioned to the breathing midline in the beginning of each fraction.

$$r^f_{\text{intra},\,t} = r^f_t - M^f_{\text{initial}}, \tag{4.2a}$$

$$r_{\text{intra, mean}} = \frac{\sum_{f=1}^{F} \sum_{t=t_s}^{t_e} r^f_{\text{intra},\,t}}{\sum_{f=1}^{F} T^f}. \tag{4.2b}$$

To analyze the motion characteristics, the intrafractional changes of the midline was determined as well as the amplitude relative to it. The intrafractional midline motion was determined similar to the overall displacement. The midline positions $M^f_{\text{intra},t}$ relative to the initial midline M^f_{initial} were calculated for each point of time between start and end of irradiation of each fraction, see eq. (4.3a). For each patient a mean of the intrafractional midline motion over all fractions was calculated, as shown in eq. (4.3b), as well as the corresponding standard deviation. As for the overall displacement, these values were determined for all three directions and in 3D. Two examples of longitudinal centroid motion and the corresponding midline can be seen in fig. 4.1.

$$M^f_{\text{intra},\,t} = M^f_t - M^f_{\text{initial}}, \tag{4.3a}$$

$$M_{\text{intra, mean}} = \frac{\sum_{f=1}^{F} \sum_{t=t_s}^{t_e} M^f_{\text{intra},\,t}}{\sum_{f=1}^{F} T^f}. \tag{4.3b}$$

The amplitude was measured as motion around this midline. Therefore, the distance between each inhale and exhale peak and the current midline for the corresponding time point

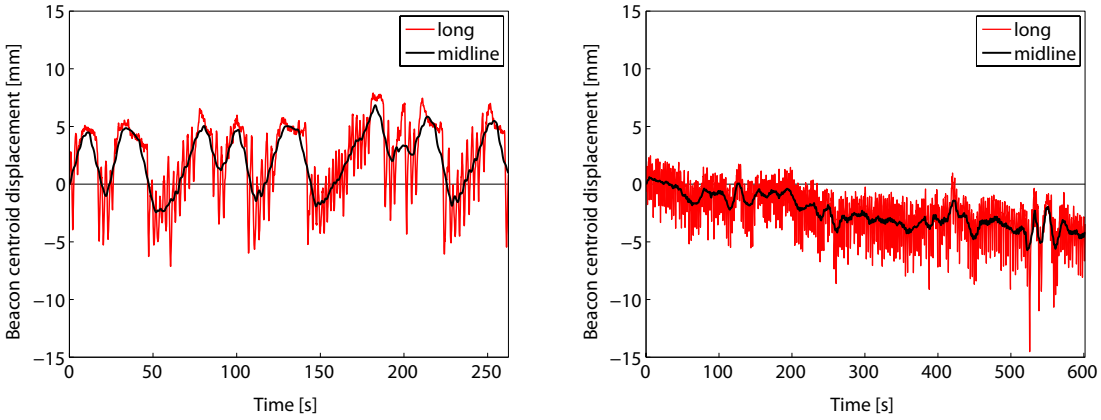

Figure 4.1: Longitudinal motion and corresponding midline for one fraction of patient 1 (a) and patient 6 (b). Motion data is presented for the time interval between start of first beam and end of last beam, only. To illustrate the method and the motion patterns, two extreme examples are chosen.

was calculated. From this data a mean amplitude for each fraction was determined in all directions and in 3D. From these means a mean and standard deviation was calculated for each patient. Thereby the standard deviations represent the interfractional variation of mean breathing amplitude.

To illustrate the parameters introduced here for the beacon centroid motion, some examples are given in the following. For a regular periodic breathing motion with constant inhale and exhale position all unidirectional mean overall displacements would be zero, because of compensation of positive and negative position values relative to the initial midline. The standard deviation would be non-zero and its value depends on the inhale-to-exhale distance. For the absolute value of the 3D overall displacement both mean and standard deviation would be non-zero, because of no negative values in the averaging process. The mean and standard deviation of the midline motion would be zero for all directions and for the absolute value of the 3D midline, because stable midline is one of the characteristics of the regular breathing. The amplitude would be half of the inhale-to-exhale distance in the unidirectional cases and in 3D. All changes of this described regularity beside from slight changes in breathing frequency have the potential to impede the averaging effects leading to non-zero results for all parameters at least in the direction in which this variation occurs and in 3D. These changes will arise from variations in inhale or exhale position or both, leading also to a time dependent variation in motion midline as shown in fig. 4.1 for two cases.

4.2.2.2 Breathing frequency

Additionally the breathing frequency was assessed from the motion data. This was done using a fourier analysis. The frequency was determined from the unidirectional motion with the highest amplitude for each patient. For each fraction the fourier transform was

calculated and a gaussian fit was performed to the power spectrum. For each fraction the mean of this gaussian fit was used as representation of the breathing frequency. From all fraction means, a patient mean and standard deviation was calculated. For patient 3 and 7 all motion amplitudes are below 1 mm, see table 4.1. Because of this, the noise from the Calypso measurement dominates the fourier transform, which makes it inappropriate for the determination of the breathing frequency. Three fractions of patient 6 could not be used because of coughing periods inhibiting the extraction of the breathing frequency.

4.2.2.3 Motion differences between beam time and adjacent beam pauses

Data of patients 1 and 4 was used to evaluate differences in motion between subsequent time intervals with and without beam delivery. These patients were picked because they show the largest mean 3D amplitude and therefore effects would show up best. A schematic of the fraction time line for one of the 3D conformal irradiations consisting of beams and beam pauses is shown in fig. 4.2. In the beam pauses the gantry of the treatment device is rotated to the next beam angle and the MLC aperture is adapted. The time line of a step-and-shoot IMRT fraction has in general the same structure, but the beam blocks are separated in segments with short beam pauses in between for adaption of MLC aperture without gantry rotation. In this analysis the beam phase of each beam for the step-and-shoot IMRT patient was defined as the time interval between the start of the first beam segment and the end of the last beam segment. This leads to a similar pattern of beams and beam pauses like for the patient receiving 3D conformal therapy. In general, the beam pauses are shorter than the beams, especially for an IMRT treatment. To avoid an influence of these different durations on the results of the following analysis, each set of motion data from one beam pause was compared with two adjacent beam time intervals of the same length. This is depicted in fig. 4.2, as well. These time intervals are called the first, second and third interval related to each beam pause. For both patients the length of these intervals is around 20 s.

For each of these intervals, two values were calculated for each motion direction for comparison. First the standard deviation of the beacon centroid position was calculated for a comparison of general motion amount. Second the mean of the motion midline during these intervals was evaluated for an analysis of beacon centroid drift. This midline mean was calculated relative to the initial midline at start of the first beam as before.

4.2.3 Inter-transponder variations

Main parts of the following analysis of the transponder geometry were presented at the annual meeting of the German Society for Medical Physics (Deutsche Gesellschaft für Medizinische Physik, DGMP) 2013. With permission of the DGMP, this section and the corresponding results and discussion is based on the abstract (Schmitt et al., 2013a), but modified and extended in parts.

Data from six lung tumor patients is used for this investigation. These were patients 1, 2, 3, 4, 6 and 7, while patient 5 was excluded because of only two transponders usable for electromagnetic localization. From these six patients, four have tumors in an upper lobe

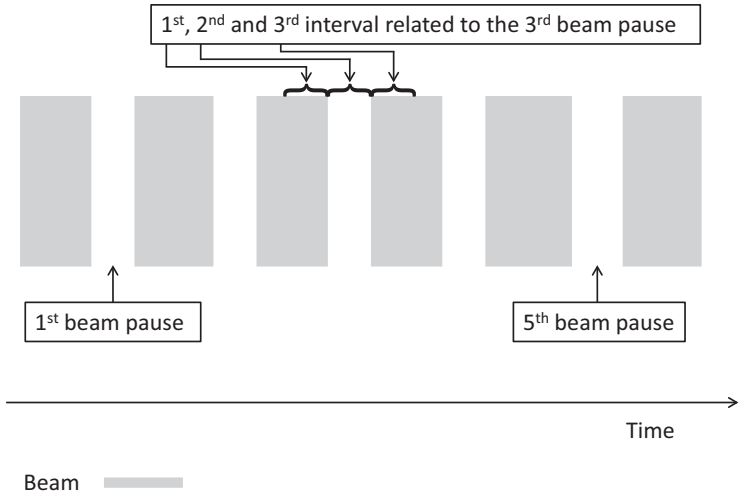

Figure 4.2: Schematic of an irradiation time line for 3D conformal therapy.

of the lung and two in the right middle lobe. Two patients received hypofractionated 3D conformal radiotherapy with ten fractions and four a conventionally fractionated step-and-shoot IMRT treatment. Average fraction time was 4.5 min and 9.2 min, respectively, with a total number of 133 evaluated fractions. As described in section 2.2.2.2, each individual transponder position is updated at a 3.3 Hz rate. These single transponder positions were made available to us for research purposes only. For all fractions, the time interval between the first and the last beam-on signal was analyzed. The single transponder positions were interpolated to 10 Hz for getting position information at the same points in time for all transponders. In fig. 4.3 a schematic of the transponder geometry is shown.

4.2.3.1 Intrafractional changes

Using the interpolated data, all inter-transponder distances in lateral, longitudinal and vertical direction as well as the 3D distances were calculated. Means and standard deviations (SD) of all data were computed for each fraction. The intrafractional variation was quantified by the SDs of the lateral, longitudinal and vertical inter-transponder distances. To analyze the reasons for large intrafractional changes, three correlations were evaluated for the motion coordinate with the largest fraction SDs. As influencing parameters, the transponder distances itself and the overall motion amount were analyzed as well as the combination of both. First, the SD of the intrafractional inter-transponder distance was correlated with the corresponding mean 3D inter-transponder distance for each fraction. A second correlation was performed between the SD and the the mean 3D amplitude detected for the transponder centroid in the corresponding fraction. Third, the SD was correlated with the product of both quantities.

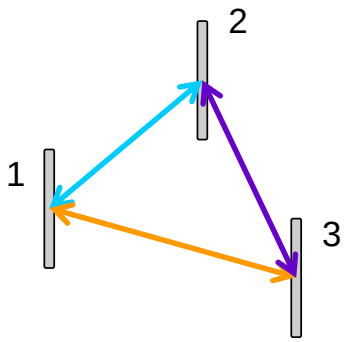

Figure 4.3: Schematic of a transponder geometry. Colors for identification of each inter-transponder distance are as used in figs. 4.8 and 4.13.

4.2.3.2 Interfractional changes

Large interfractional changes in transponder geometry can make a replanning procedure necessary. To quantify these changes, the variations of the area of the triangle spanned by the transponders were analyzed. This was done in two ways: 1) From the transponder distances determined in section 4.2.3.1, the area of the spanned triangle was calculated for each point in time. For these areas, the means and standard deviations per fraction were determined. 2) To check if the changes determined via electromagnetic localization can be reproduced in the CTs as well, the area of the beacon triangle was derived from the CT data sets for the two patients with the largest decrease in triangle area. For the read outs of beacon positions the maximum exhale phase of each 4D CT data set was used, because they are expected to show minimum motion artifacts. This is because of the large proportion of breathing cycle time this phase is covering, see e.g. (Moorrees and Bezak, 2012). From each data set the positions of all beacons were determined in all three directions and from their distances the triangle areas were calculated.

Additional to these patient specific calculations, an average change in 3D inter-transponder distances per day after first fraction over all patients was calculated from the Calypso data. For this, a linear regression of 3D mean distance and day was done for all transponder pairs. All 18 slopes (6 patients $\times$ 3 transponder pairs) of these regressions were then averaged.

4.2.4 Correlation between internal and external motion

For three lung patients (patients 5, 6 and 7) we had the possibility to monitor the chest motion with the Anzai belt, see section 2.2.2.3, concurrently with the Calypso measurement. For these three patients, the correlation analysis was made for 29, 23 and 25 fractions, respectively. In sum, 7 fractions had to be excluded from the evaluations because of coughing periods. The mean duration of the used fractions was 10.3 min. Prior to the correlation analysis, the data sets had to be synchronized and sampled to the same update rate, this was done as follows. First, the different data sets were synchronized using the particular beam-on status data, collected together with the motion data. To obtain these beam status data, the Calypso System uses a detector for scattered radiation, while the Anzai system gets beam status data directly from the accelerator control unit. Second, the Anzai data, originally sampled with 40 Hz are recalculated to the 10 Hz pattern of the Calypso data.

For each fraction the linear correlation coefficients r between the 3 unidirectional beacon centroid motion data and the one-dimensional Anzai data was calculated.

To evaluate possible phase shifts between the signals, either due to the different methods of beam status determination and sampling rate or due to anatomical or physiological effects, these calculations were repeated with time shifted Anzai data. The Calypso time T_C were held fixed and the Anzai time T_A were shifted in steps of 50 ms forward and backward until half of the mean breathing cycle time T_{BC} was reached, $-T_{BC}/2 \leq T_C - T_A \leq T_{BC}/2$. The breathing cycle time for patient 7, which could not be determined from the Calypso data, was taken from the Anzai data reports. The correlation coefficients for each fraction were averaged for each patient to mean correlation coefficients for each motion direction per time shift to extract systematic shifts. The time shift corresponding to the best correlation coefficient (largest norm of mean r), was then taken as phase shift.

This correlation analysis for whole fraction data sets does not consider intrafractional changes in correlation between internal beacon centroid motion and external chest motion. The correlation can vary over time because of changes in the breathing pattern or because of patient motion leading to changes in the patient setup. Due to that, the data for whole fractions represents averages of the time dependent correlation. When the external signal is used as surrogate for the tumor motion, it is important to either guarantee a stable correlation between internal and external motion or to update the correlation model frequently, otherwise the applied dose distribution will differ from the planned one. To demonstrate possible changes within a single fraction, the correlation is analyzed using a sliding window covering three mean breathing cycle times (as proposed by (Ionascu et al., 2007)) for the fractions with the best single fraction correlation coefficients. For this analysis, the time shift found for this single fraction is used.

In a last step, the norm of the best correlation coefficient for each direction of the three patients was plotted against the mean amplitude of the corresponding Calypso data, taken from table 4.1. The correlation between these two parameters was assessed.

4.3 Results

4.3.1 Motion quantification

4.3.1.1 Overall displacement, midline changes and motion amplitude

The distribution of overall intrafractional centroid displacements relative to the initial midline for all patients can be seen as a boxplot in fig. 4.4. The corresponding means and standard deviations are listed in table 4.1. The mean values of the unidirectional displacements are near zero (absolute value below 0.5 mm) for the majority of cases, as it is expected for a periodic breathing motion. The norm of the 5 larger deviations are between 0.6 mm and 1.9 mm. These values indicate a change in the motion midline. The three-dimensional displacement, whose values are not dominated by the compensation of positive and negative position values, show mean values between 1.2 and 4.6 mm with standard deviations from 0.7 mm to 2.6 mm.

Table 4.1: Results of beacon centroid motion evaluation for all patients. For amplitude and breathing frequency, the standard deviations describe the interfractional changes. The motion directions related to the highlighted amplitudes were used for breathing frequency determination. The motion amplitudes of patients 3 and 7 are too small to determine a breathing frequency. Abbreviations: RUL: right upper lobe, LUL: left upper lobe, RML: right middle lobe.

[1]Calculated using eq. (4.2b).
[2]Calculated using eq. (4.3b).

Patient			P1	P2	P3	P4	P5	P6	P7
Tumor position			RUL	LUL	LUL	RML	LUL	RML	RML
Intrafractional displacement [mm]	Lat	Mean	0.0	-0.2	0.1	0.4	0.4	0.2	0.4
		SD	0.9	0.9	0.6	1.5	0.8	2.2	0.7
	Long	Mean	0.6	-0.1	0.3	0.7	0.1	-1.0	0.4
		SD	3.3	0.6	0.7	2.6	0.8	2.4	0.8
	Vert	Mean	-1.9	0.1	0.0	0.1	0.1	-0.6	0.0
		SD	3.2	1.2	0.5	0.7	2.2	1.7	0.7
	3D	Mean[1]	4.6	1.5	0.9	2.8	2.1	3.4	1.2
		SD	2.6	0.7	0.6	1.5	1.3	1.9	0.7
Intrafractional midline motion [mm]	Lat	Mean	0.0	-0.2	0.1	0.4	0.4	0.2	0.4
		SD	0.4	0.4	0.5	0.9	0.6	1.9	0.7
	Long	Mean	0.6	-0.1	0.4	0.7	0.2	-1.0	0.4
		SD	2.5	0.5	0.7	1.0	0.6	1.9	0.7
	Vert	Mean	-1.5	0.1	0.0	0.1	0.1	-0.6	0.0
		SD	2.6	0.6	0.5	0.5	1.4	1.6	0.6
	3D	Mean[2]	3.4	0.8	0.8	1.4	1.4	2.9	1.0
		SD	2.0	0.4	0.7	1.0	0.9	1.7	0.7
Amplitude around current midline [mm]	Lat	Mean	0.9	1.1	0.4	1.4	0.8	1.6	0.3
		SD	0.2	0.3	0.1	0.3	0.2	0.3	0.1
	Long	Mean	3.1	0.5	0.2	3.2	0.4	2.1	0.7
		SD	0.6	0.1	0.0	0.5	0.2	0.3	0.2
	Vert	Mean	2.7	1.6	0.3	0.5	2.2	0.7	0.5
		SD	0.3	0.2	0.0	0.1	0.7	0.2	0.1
	3D	Mean	4.0	2.0	0.5	3.4	2.3	2.8	0.9
		SD	0.6	0.3	0.1	0.5	0.7	0.3	0.2
Frequency [breath/min]		Mean	15	23	-	13	10	24	-
		SD	1	1	-	1	1	3	-

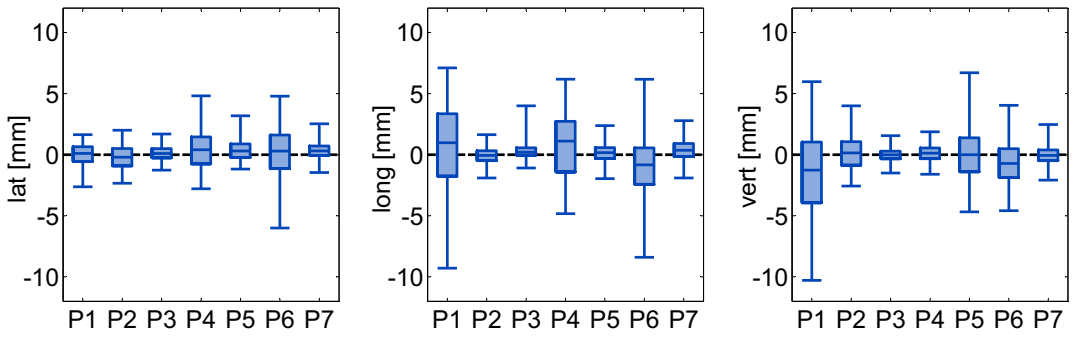

Figure 4.4: Beacon centroid displacements for all patients in three directions calculated as deviations from the initial midline for all fractions. The box indicates the values between 25 % and 75 % of the motion data and the vertical line within the box marks the median. To exclude outliers, the whiskers cover only 99 % of the data.

The intrafractional changes of the motion midline are shown in table 4.1 as well. Here the unidirectional means range from −1.5 mm to 0.7 mm with standard deviations between 0.4 and 2.6 mm. Two different patterns of midline changes can be seen in fig. 4.1. The longitudinal midline changes are periodic for the fraction of patient 1 in (a) and for the displayed fraction of patient 6 the midline drifts towards negative values (b). For the three-dimensional midline changes mean values between 0.8 and 3.4 mm with standard deviations between 0.4 and 2.0 mm were measured.

The mean amplitudes around the current midline are presented in table 4.1, too. For two of the seven patients all amplitudes, including the three-dimensional one, are below 1 mm. For the other five patients the maximum unidirectional amplitude appears either in the longitudinal or in the vertical direction, as highlighted in the table. These maximum amplitudes are between 1.6 and 3.2 mm. Three-dimensional amplitudes range from 0.5 mm to 4.0 mm. The standard deviation for all amplitudes represent the interfractional change of motion amplitudes, which is small with all values well below 1 mm.

4.3.1.2 Breathing frequency

Breathing frequencies were determined from the unidirectional motion data with the largest amplitude per patient, as highlighted in table 4.1. The fourier transforms lead to power spectra like the one shown in fig. 4.5. In this figure, a power spectrum of lateral motion of one fraction of patient 2 is shown. This spectrum is not used for the determination of breathing frequency, because it is not the dominant motion direction. But it shows another motion aspect, which can be seen best in lateral spectra: a second peak around 1.3 Hz representing motion induced by heart beat. The mean breathing frequencies lie between 0.4 and 0.17 Hz equivalent to a range of 10 breath/min to 24 breath/min. The standard deviation representing the interfractional change of the fractions mean frequency is between 4 and 13 % of the mean.

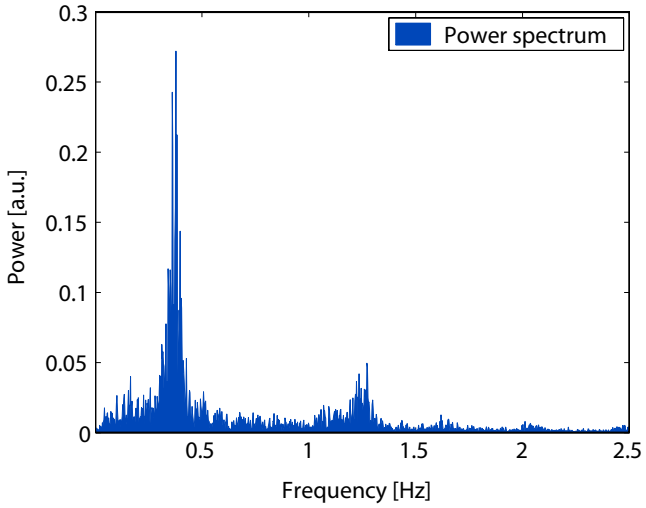

Figure 4.5: Power spectrum of the lateral motion of one fraction from patient 2. The smaller peak at around 1.3 Hz results from heart beat.

4.3.1.3 Motion differences between beam time and adjacent beam pauses

Differences between consecutive motion patterns can be large, as shown in fig. 4.6 for patient 1. The standard deviations have differences up to 2.1 mm in longitudinal and up to 4.2 mm in vertical direction. The lateral deviations are small, as the motion amount in lateral direction is small in general. The differences in mean midline position are up to 7.0 mm in longitudinal and up to 9.1 mm in vertical direction.

To evaluate, if these large deviations arise from a systematic difference between patient motion during beam-on phases and beam pauses, the vertical motion of the two fractions from patient 1 showing the largest deviations is shown in fig. 4.7. For fraction 1 in fig. 4.7(a), the periodic breathing pattern is superimposed by a periodic motion pattern, with a larger cycle duration. This motion pattern leads to motion shifted to the negative vertical direction in some beam pauses, but it fits not perfectly to the periodicity of beam-on and beam-off phases. Thus it is unlikely that it results from a voluntary movement or change in breathing pattern of the patient recognizing the beam-on phases. In fraction 10, depicted in fig. 4.7(b), the superimposed motion pattern is different in cycle time but with some similarities in the pattern itself.

The patient with the second large 3D motion amplitude (patient 4) is chosen for this evaluation, too. The obtained differences in standard deviations and midline positions are very small. For all fractions and motion directions the differences in standard deviations are below 1 mm, while the mean midline position deviates not more than 2 mm between adjacent time intervals.

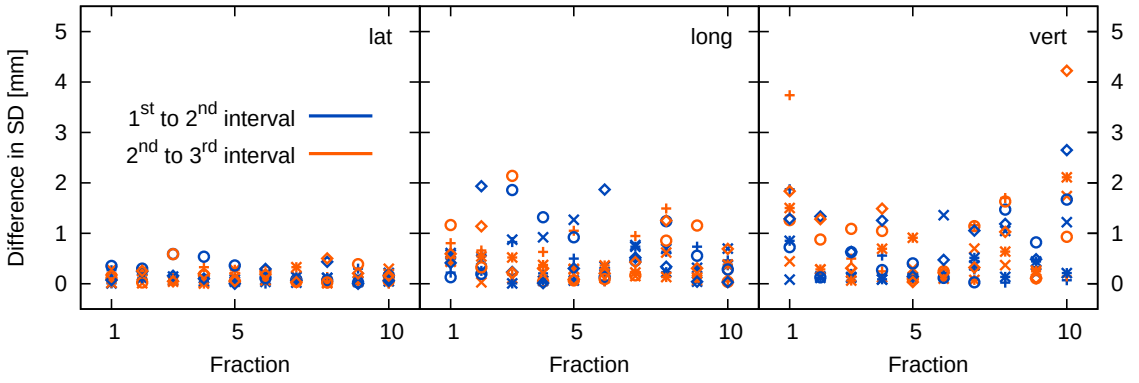

(a)

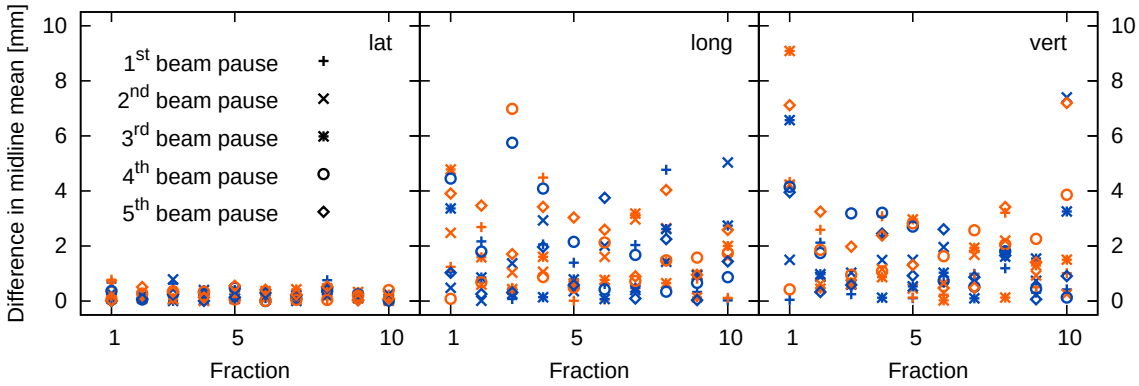

(b)

Figure 4.6: Results for the evaluation of differences in motion amount and patterns between each beam pause and the beam-on phases prior and after the specified pauses for patient 1. Deviations in overall standard deviations are shown (a) as well as deviations in mean midline position (b). Both legends are valid for all images.

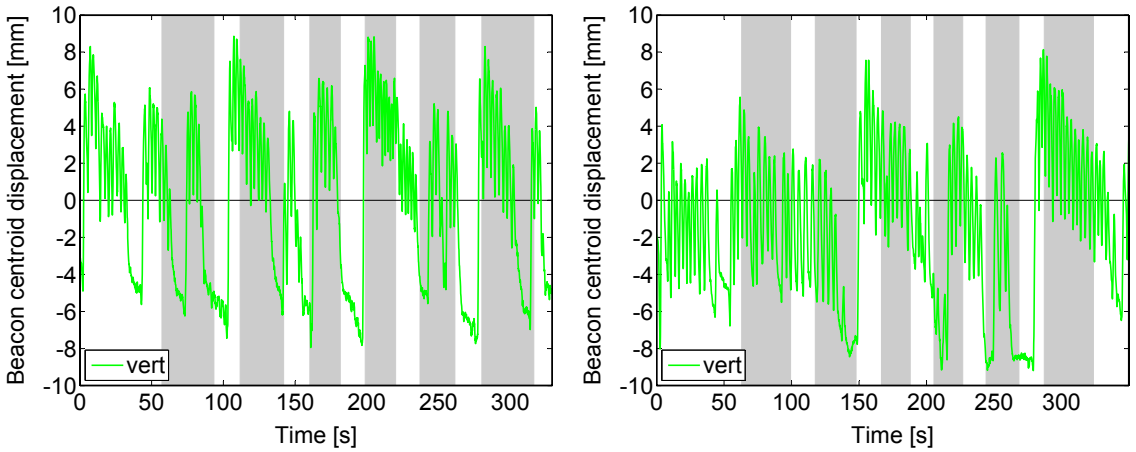

(a) (b)

Figure 4.7: Vertical motion for fraction 1 (a) and fraction 10 (b) of patient 1. The shaded areas indicate the beam-on times.

4.3.2 Inter-transponder variations

4.3.2.1 Intrafractional changes

The six patients show very diverse results in the intrafractional variations of inter-transponder distances, see fig. 4.8. For three patients (3, 6 and 7) nearly all SDs of inter-transponder distances lie below 1 mm for all three directions. For patients 2 and 4 there are SDs between 1 and 2 mm in longitudinal direction for two transponder pairs, while for patient 1 there are values of above 3 mm of SD for two transponder pairs in longitudinal direction. The corresponding mean 3D inter-transponder distances for patient 1 are 6.8 and 6.0 cm. Only the SDs in longitudinal direction show values of above 1 mm, hence they were studied further. No correlation of the longitudinal SDs with the corresponding mean 3D inter-transponder distance per fraction was found (Pearson's correlation coefficient r=0.42), see fig. 4.9(a). The same was shown for the relation between the longitudinal SDs and the mean 3D centroid's amplitude (r=0.49), see fig. 4.9(b). A much stronger correlation (r=0.83) was found for the relation between the longitudinal SDs and the product of the prementioned parameters, see fig. 4.10. All correlation coefficients are accompanied with a $p < 0.01$.

4.3.2.2 Interfractional changes

A decrease was found for the beacon triangle area over the whole treatment course for all patients, see fig. 4.11. The extent of decrease differs from patient to patient. Using the data from the linear regression, a decrease of 5.1 % and 5.9 % was found for the two hypofractionated patients. For the conventionally fractionated IMRT patients the decrease range from 6.6 % for patient 4 to 41.5 % for patient 7. The determination of beacon triangle area from CT data was made for patients 3 and 7, the two patients with the largest decrease in triangle area determined from the Calypso data. As can be seen in fig. 4.12, for all

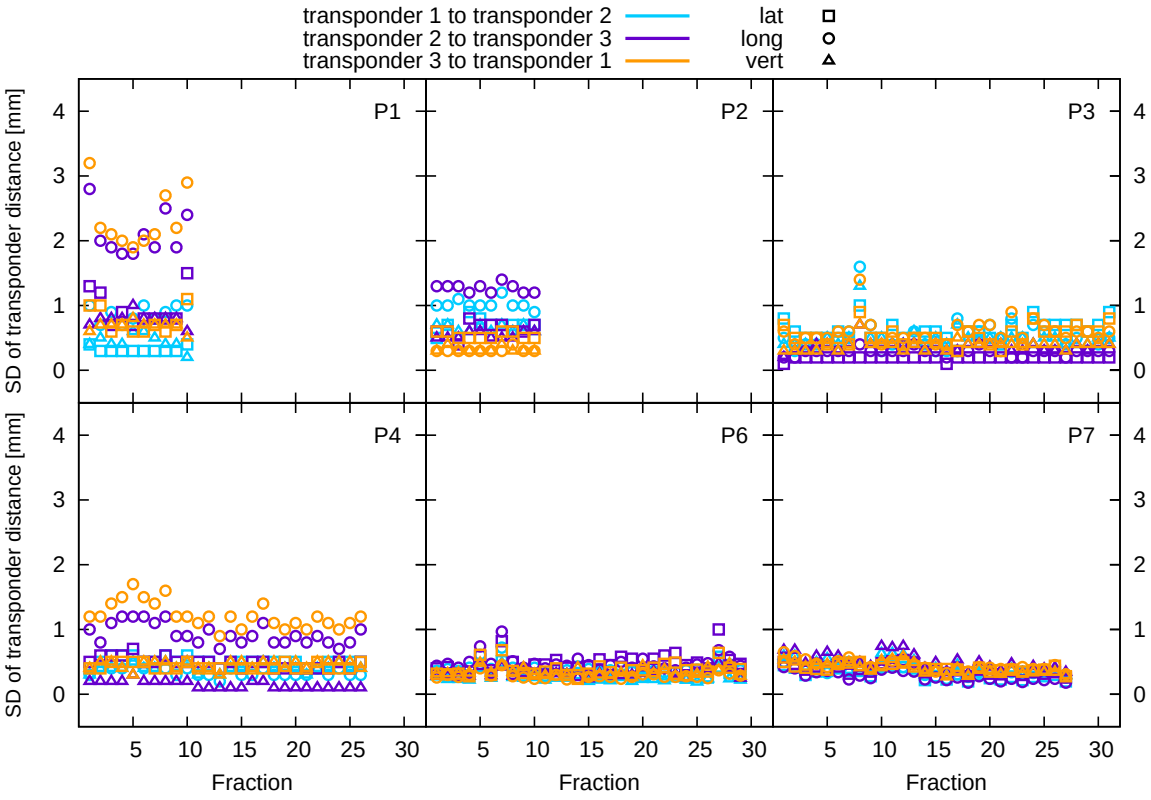

Figure 4.8: Standard deviations of the lateral, longitudinal and vertical inter-transponder distances for all fractions of each patient.

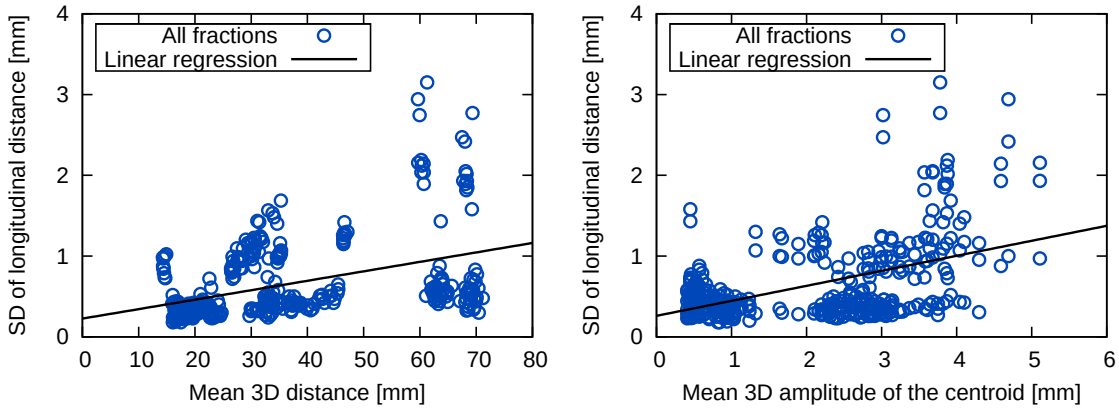

(a) (b)

Figure 4.9: Standard deviations of longitudinal inter-transponder distances per fraction plotted against mean 3D distance per fraction (a) and against mean 3D amplitude of the transponder centroid motion per fraction (b). Additionally the graphs of linear regressions are shown. It can be seen, that the linear correlation of the respective data pairs is weak.

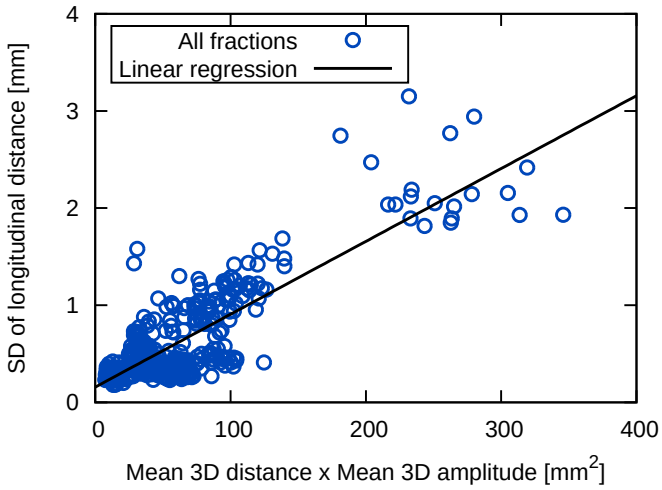

Figure 4.10: Standard deviations of longitudinal inter-transponder distances per fraction plotted against the product of mean 3D inter-transponder distance and mean 3D amplitude of the transponder centroid motion per fraction. A strong correlation can be seen. Additionally the linear regression is depicted.

days with corresponding data the triangle areas determined with both methods are in good agreement. The Calypso value lies always inside the error region of the value calculated using the CT data set. This error region was calculated from the inaccuracy which is expected for manual read out of beacon positions in the CT slices. Here this inaccuracy was estimated with half of the pixel size in all directions.

The interfractional changes in inter-transponder distances resulting in such decrease in the area of the beacon triangle can be very heterogeneous in one patient. Two examples are shown in fig. 4.13. For patient 6 can be seen, that two transponder distances decrease, while one distance increases over time. For patient 7 a shrinkage of the inter-transponder distance of 8 mm for two transponder pairs over the whole treatment can be found. These pairs had an initial 3D distance of 3.7 and 4.5 cm. This is the patient with the largest slopes in the linear regression of the transponder distances against the day after first fraction, namely -0.25 mm per day for one transponder pair and -0.24 mm for another. The calculation of this slope for all transponder pairs in all patients lead to an average shrinkage of 3D inter-transponder distances of (-0.04 ± 0.09) mm per day. This mean slope with large standard deviation reflect the very heterogeneous situation between patients and even between transponders in the same patient, with some transponder distances even growing over time.

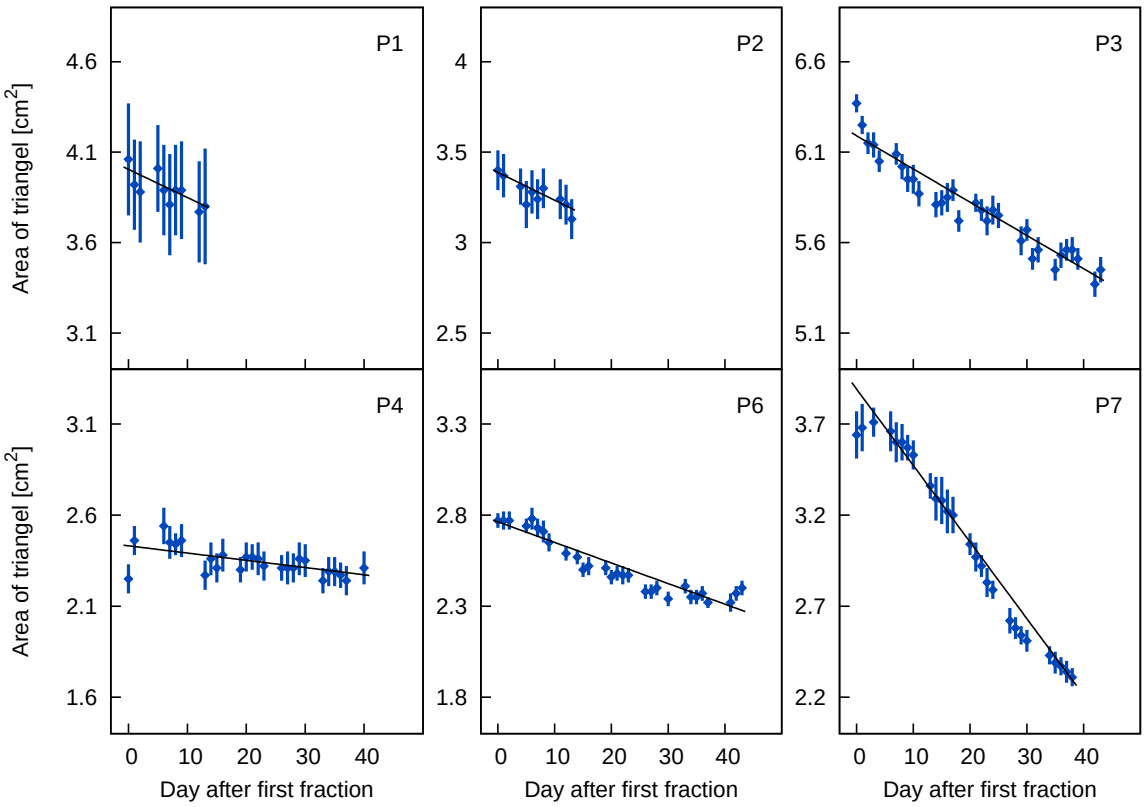

Figure 4.11: Mean and standard deviation (depicted by error bars) of the triangle area spanned by the three transponders for all fractions of all patients. In addition the graph of the linear regression is shown for better visualization of the trend. Each vertical axis has a range of $2\,\mathrm{cm}^2$.

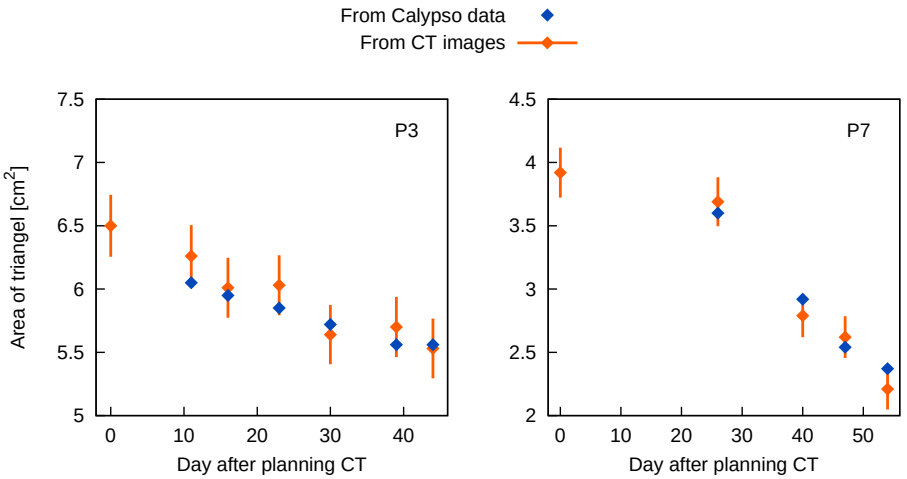

Figure 4.12: Comparison of the beacon triangle area determined from Calypso data and from CT data sets for patients 3 and 7. The error bars indicate the error from read out inaccuracy due to CT pixel size. The first data point of each patient was determined from the planning CT, because of that, no Calypso data exists for this day. Both vertical axes cover a range of 2.5 cm^2. The first control CT was acquired at the day of the fifth fraction for patient 3 and at the day of the sixth fraction for patient 7.

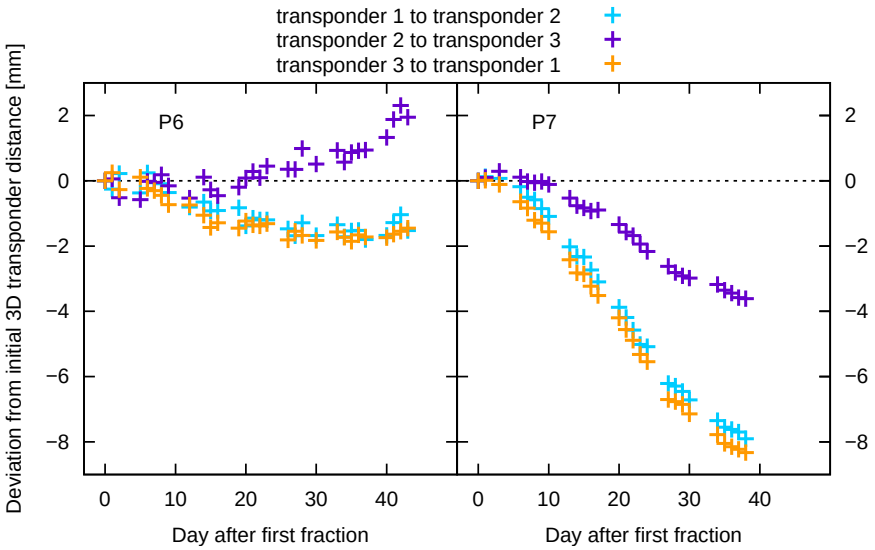

Figure 4.13: Deviation of the mean 3D inter-transponder distances from the initial distances for each fraction of patients 6 and 7.

4.3.3 Correlation between internal and external motion

The correlation coefficients in dependence on time shifts are shown in fig. 4.14. For all patients and motion directions the pattern of one period of a sinusoidal function can be seen as effect of the periodic character of both underlying data sets.

The numerical results of the correlation analysis between the Calypso centroid motion and the changes in abdominal circumference detected by the Anzai belt are shown in table 4.2. The mean correlation coefficients are very heterogeneous, both between patients and between motion directions. Without regarding a phase shift between the monitored motion data, only the longitudinal beacon centroid motion of patient 6 shows strong correlation ($|r| \geq 0.8$) with the Anzai signal. Taking possible phase shifts into account, the best mean correlation coefficients for patient 5, 6 and 7 are 0.82 for the vertical motion, -0.85 for the longitudinal motion and 0.57 for the vertical motion, respectively. The sign of the correlation coefficient gives the direction of the relation between internal and external motion. For these three values is the relation as follows: positive sign of r for vertical direction means an inhalation causing increase of chest circumference is accompanied with a transponder centroid motion in anterior direction, while the negative r for longitudinal motion describes a caudal transponder centroid motion for inhalation.

In table 4.2 the best single fraction correlation coefficients are shown for completeness. These single fraction data are determined with time shifts, too. These time shifts are not listed, as they differ only slightly from the time shifts determined for the best mean correlation coefficients. In most cases, this best single fraction correlation is much stronger, than the best mean correlation. This is not caused by averaging effects due to different time shifts for each fraction. The time shifts for different fractions of one patient show no large differences. Large discrepancies between best mean correlation coefficients and best single fraction correlation coefficients are an effect of the outlying character of the best single fraction in comparison to the others.

In fig. 4.14 mean values and standard deviations are depicted, only. The development of the correlation coefficient from fraction to fraction, all gathered at the time shift of the best mean r, is shown in fig. 4.15 for the vertical Calypso motion of patient 5 and the longitudinal motion of patient 6, as they are the only ones with a strong mean correlation coefficient. No interfractional trend can be seen. For both patients nearly all fractions lie in a band of correlation coefficients with a width of 0.2, the outliers go down until 0.54 for patient 5 and until -0.76 for patient 6.

For the single fraction correlation analysis the following two data sets were used: fraction 6 of patient 5 (vertical direction) and fraction 19 of patient 6 (longitudinal direction), as these are the fractions with the largest single fraction correlation ($r = 0.94$, resp. $r = -0.94$). For patient 7 no fraction with a strong correlation was found. The variations with time can be seen in fig. 4.16. They show no trend in time but variations between 0.90 and 0.98 for patient 5 and between -0.73 and -0.99 for patient 6.

In fig. 4.17, the norm of the best mean correlation coefficient is plotted against the corresponding mean Calypso centroid amplitude for all directions of the three patients. The data is shown together with a linear regression. This linear regression is accompanied with a correlation coefficient of 0.81 ($p < 0.01$). This indicates a strong relationship between

Table 4.2: Results of the correlation analysis between internal and external measured motion. The correlation coefficients are highlighted with coloured background: red: weak correlation ($|r| < 0.5$), yellow: moderate correlation ($0.5 \leq |r| < 0.8$), green: strong correlation ($|r| \geq 0.8$). Best single fraction correlation coefficients are listed without the corresponding time shifts.

			P5	P6	P7
Lat	Mean r without time shift		0.00	-0.67	-0.30
	Best mean r		-0.63	-0.67	-0.32
	Corresponding time shift	Absolute [s]	1.40	0.00	-0.15
		Part of breathing cycle [%]	22.2	0.0	5.6
	Best single fraction r		-0.86	-0.88	-0.63
Long	Mean r without time shift		-0.54	-0.85	0.45
	Best mean r		-0.64	-0.85	0.54
	Corresponding time shift	Absolute [s]	0.55	0.00	-0.20
		Part of breathing cycle [%]	8.7	0.0	7.4
	Best single fraction r		-0.89	-0.94	0.78
Vert	Mean r without time shift		0.65	-0.18	0.57
	Best mean r		0.82	-0.36	0.57
	Corresponding time shift	Absolute [s]	0.60	-0.40	0.00
		Part of breathing cycle [%]	9.5	16.0	0.0
	Best single fraction r		0.94	0.56	0.79

the Calypso motion amplitude and the correlation of internal centroid motion and external chest motion: the larger the internal motion amplitude, the larger the correlation between internal and external motion.

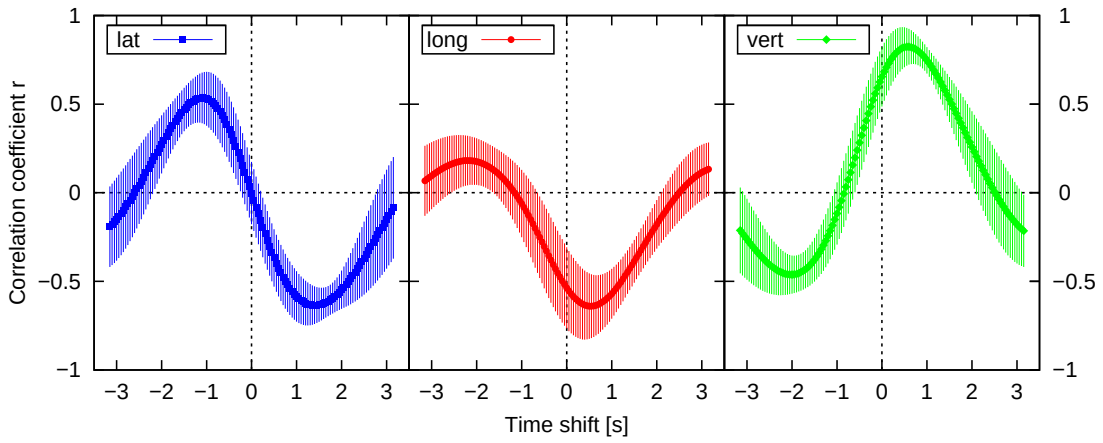

(a)

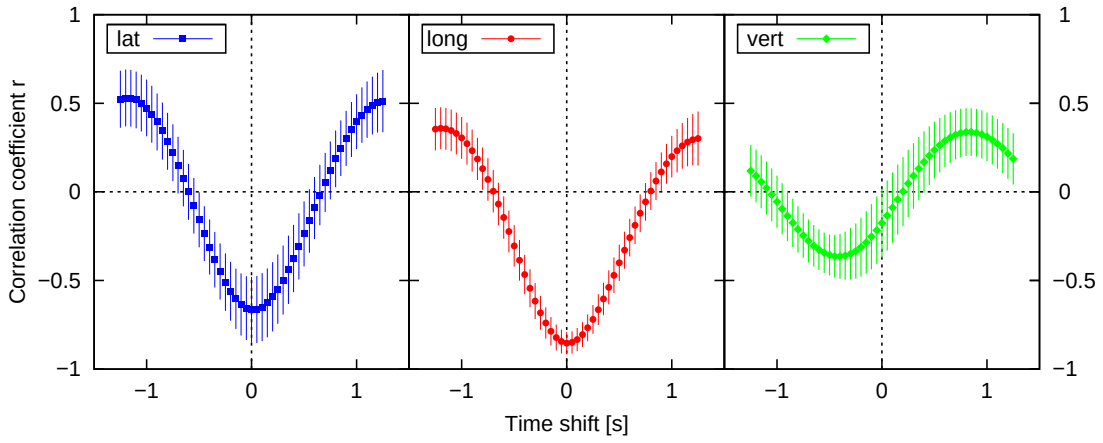

(b)

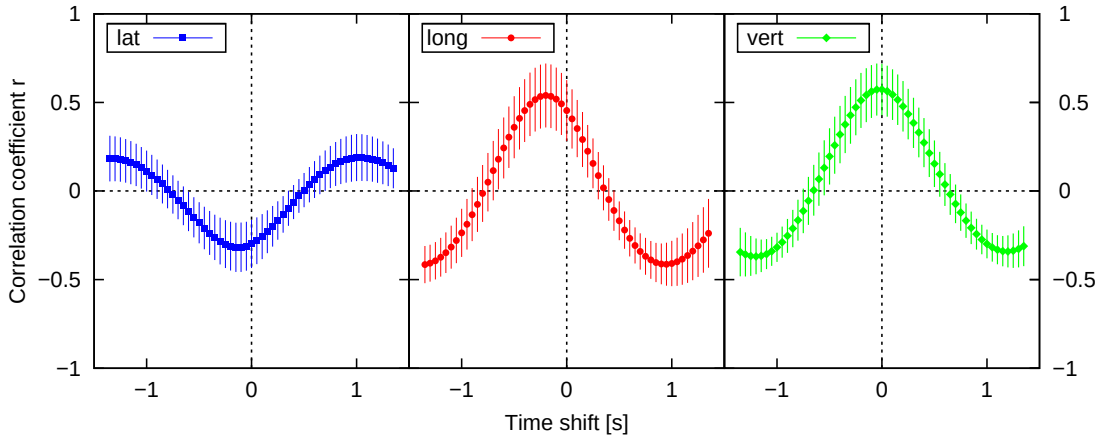

(c)

Figure 4.14: Correlation coefficients between the three-dimensional Calypso data and the one-dimensional Anzai signal. Mean values with standard deviations over all fractions are shown. They are plotted against the time shift between the corresponding signals, used for calculation. The time scale at the horizontal axis covers the mean duration of one breathing cycle for each patient. Data for patient 5, 6 and 7 are shown in (a), (b) and (c), respectively.

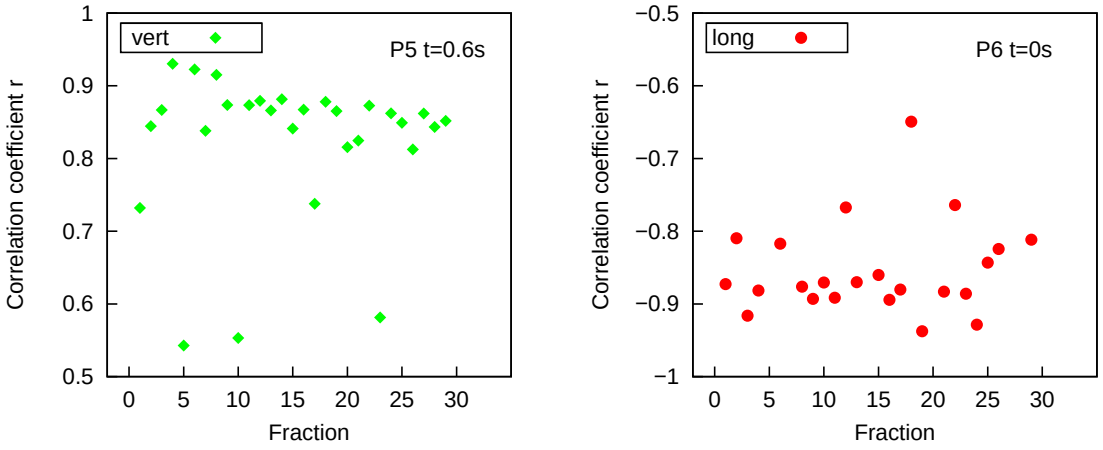

(a) (b)

Figure 4.15: Correlation coefficients for all fractions between Anzai data and Calypso data for patients 5 (a) and 6 (b), using the motion direction with largest correlation, only. For all fractions of each patient the time shift corresponding to best mean r is used, as given in table 4.2. Gaps in (b) result from the excluded fractions.

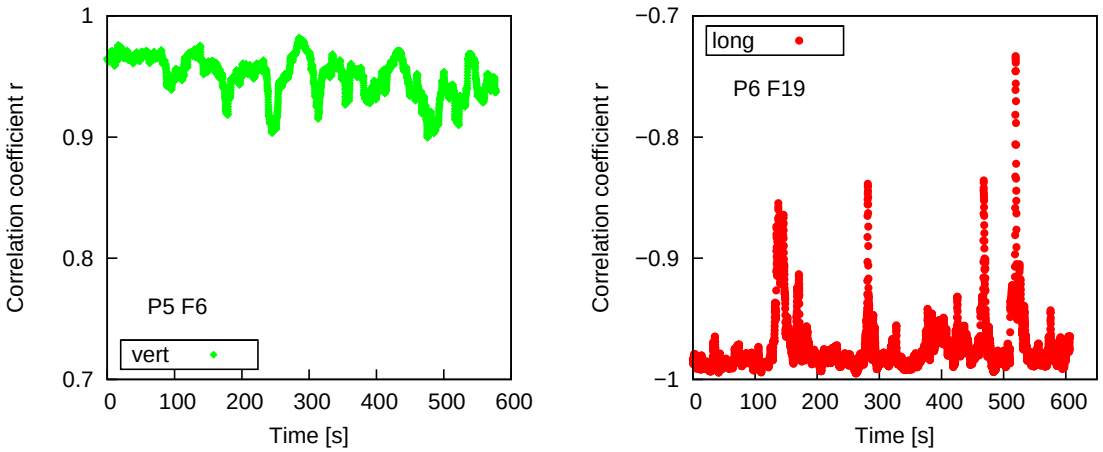

(a) (b)

Figure 4.16: Intrafractional variation of the correlation coefficent between Anzai data and Calypso data. The correlation is calculated in a sliding window of 3 mean breathing cycle durations each starting at the depicted time point (horizontal axis) after start of irradiation. For patients 5 and 6 the fraction with the largest single fraction r is chosen. For patient 5 the vertical motion direction of fraction 6 is used, with a corresponding time shift of 0.45 s (a). For patient 6 the longitudinal motion direction of fraction 19 is used, with a corresponding time shift of 0.00 s (b).

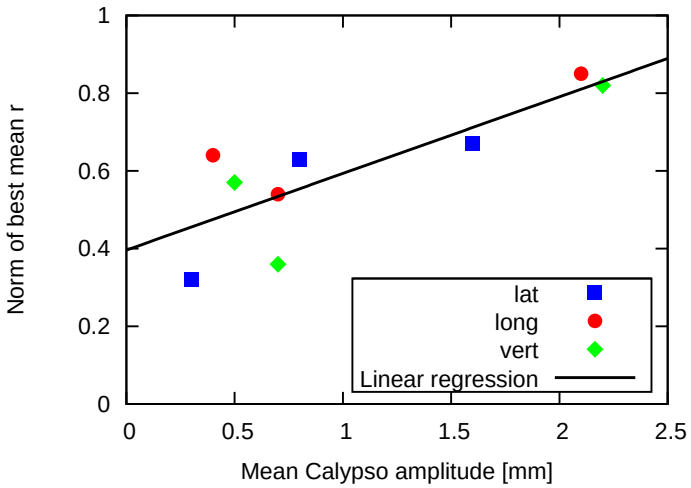

Figure 4.17: Plot of the norm of the best mean correlation coefficient against the corresponding mean amplitude of the beacon centroid for all three directions.

4.4 Discussion

4.4.1 Motion quantification

Besides the pure motion quantification, the correlation between motion amount and tumor localization was studied in some cases, e.g. using orthogonal radiographs (Stevens et al., 2001; Seppenwoolde et al., 2002), an MR scanner (Plathow et al., 2004) or multiple CT scans (van Sörnsen de Koste et al., 2003). Two of these analyses show tumor motion amplitude to be larger the nearer the tumor position is to the diaphragm (increasing for the locations upper lobe, middle lobe, lower lobe). The patient cohort used in this thesis contains only seven patients, four with upper lobe and three with middle lobe tumors. Due to that, the derived results are compared with published data for upper and middle lobe tumors, if not stated different. In this thesis the amplitude is defined as distance between midline and inhale or exhale peak, respectively. In the publications used for data comparison, a peak-to-peak amplitude is used. Therefore the current results are doubled for comparison.

Published data for image based breathing motion analysis shows similar values for motion amplitudes and breathing frequencies as found here with the electromagnetic system. An analysis using respiration correlated cone-beam CT (Bissonnette et al., 2009) reports on mean 3D amplitudes extracted from 6 CTs per patient. Considering only the 11 patients with tumors in an upper or middle lobe in this publication, a mean 3D amplitude of (3.7 ± 3.2) mm can be calculated. The corresponding value for our data is (4.5 ± 2.5) mm. Mean values for unidirectional intrafractional motion, determined from lung marker motion detected fluoroscopically 30 times a second are reported by (Seppenwoolde et al., 2002). Therefore the peak-to-peak amplitude was determined for each breathing cycle and then averaged, considering only the 13 patients with tumors in an upper or middle lobe the following values are valid: lateral (1.2 ± 0.9) mm, longitudinal (3.2 ± 3.2) mm and vertical (2.6 ± 2.2) mm. The corresponding values determined in this thesis are (1.8 ± 1.0) mm, (2.9 ± 2.6) mm and (2.4 ± 1.9) mm. Determination of the average value of the largest inhale-to-exhale difference during the setup procedure using the same marker detection method as Seppenwolde et al. for 21 patients results in distances of (8.2 ± 6.5) mm in lateral, (10.7 ± 8.6) mm in longitudinal (8.8 ± 7.0) mm in vertical direction (Shirato et al., 2006). The localizations of these tumors are not specified, hence there can be lower lobe tumors integrated, leading to more pronounced motion. Our data for complete intrafraction motion show smaller values: lateral (4.7 ± 2.3) mm, longitudinal (7.9 ± 5.8) mm and vertical (6.6 ± 4.5) mm. For the 13 patients in (Seppenwoolde et al., 2002) breathing frequencies are calculated to range from 13 breath/min to 22 breath/min with a mean and standard deviation of (18 ± 2) breath/min, the seven patients evaluated here show similar breathing frequencies: a range of 10 breath/min to 24 breath/min and a mean and standard deviation of (17 ± 6) breath/min.

Intrafractional changes in the motion midline can be large, as shown here. The largest mean difference between intrafactional 3D midline position and the fraction specific initial midline is determined to 3.4 mm for patient 1. In the same patient, the largest difference in unidirectional mean midline position between two consecutive intervals of 20 s was found to be 9.1 mm in vertical direction. (Guckenberger et al., 2007) reported on maximum longitudinal drift in mean tumor position for repeated 4D CT scans of 6.9 mm for one lower lobe

tumor within 30 min. These results have to be considered if gating or tracking of the tumor during the irradiation shall be performed. It has to be ensured that the used gating window remains in the planned relation to the tumor position. For motion tracked irradiation, it has to be decided for each individual patient if the motion prediction, needed because of system latencies, can deal with the patient's irregular breathing pattern.

Interfractional changes of tumor midline can not be evaluated with our data, because the Calypso System was not used for patient positioning in the trial. All calculations in this thesis are relative to a fraction specific initial midline. But there is published data indicating remarkable interfractional variations of mean tumor position relative to the bony anatomy. This data indicates the necessity of a patient positioning procedure, which is based on the actual tumor position and not on any external marker or landmark. Variations in mean tumor position from fraction to fraction are reported to be up to 18 mm in longitudinal direction and up to 24 mm in lateral and vertical direction, determined from the planning 4D CT and a repeated one after 15 fractions (Schmidt et al., 2013). (Sonke et al., 2008) calculated interfractional variations of the time-weighted mean tumor position of 40 patients using a median number of nine 4D CBCT data sets per patient. The group systematic error (one standard deviation) was determined to 1.6 mm in lateral direction, 3.9 mm in longitudinal direction and 2.8 mm in vertical direction. The random error was found to be of the same size. (Juhler Nøttrup et al., 2007) analyzed interfractional changes in exhale positions of a box with infrared markers on the patient's chest for 11 patients, the median value of interfraction span in these positions was calculated to 14.8 mm with a range of 5.5 mm to 31.0 mm.

4.4.2 Inter-transponder variations

Longitudinal inter-transponder distances vary due to intrafraction breathing motion with an SD of up to 3 mm. This variation depends on the combination of inter-transponder distance and overall motion amount. The motion amount for each patient is unknown before the transponder implantation, so the inter-transponder distances should be as small as possible enclosing the whole tumor, while the transponder centroid should be as close to the tumor centroid as possible for good representation of tumor motion. Some implications on marker positions for different tumor locations in the lung are made by (Smith et al., 2011) evaluating tissue motion around tumors in 4D CTs.

There is a general decrease in inter-transponder distances over the course of radiation treatment. The spanned triangle area of the transponders shrank between 6.6 % and 41.5 % for the conventional fractionated patients. Two patients got additional chemotherapy, however, no statement can be made about the effect of the combination of radiotherapy and chemotherapy. The patient with the concurrent chemotherapy was excluded from this part of investigation, because of only two trackable transponders, as described before and the patient with the chemotherapy before the irradiation showed a decrease of 17.6 % which fits in the decrease of the other patients.

To compare the shrinkage with published data, the distances itself have to be reviewed. Their variations are larger than reported for interfractional changes of fiducial marker distances by (Imura et al., 2005). They report on inter-marker distances during one to two

weeks of treatment and follow up measurements until 40 days after the first fraction. Thereby 80 % of the measured distances differ maximum 1 mm from the initial distances, while 95 % are within 2 mm. The corresponding values for the changes in mean fraction distances for the Calypso transponders in this work are much less with 45 % and 75 % for 1 mm and 2 mm, respectively. The changes in inter-transponder distances are an indicator for geometry variations in the surrounding lung tissue. This can lead to a deviation of the relationship of transponder centroid and tumor centroid from the situation found in the planning CT, especially, if the shrinkage is not uniform for all inter-transponder distances in a patient. (Roman et al., 2012) report on mean interfractional marker-to-tumor centroid displacements of (4 ± 2) mm in lateral, (4 ± 3) mm in longitudinal and (3 ± 2) mm in vertical direction, measured in weekly 4D CBCTs over seven weeks in seven patients. The corresponding 3D distance change is (5 ± 3) mm. This indicates a necessity of a regular evaluation of the inter-transponder distances, if a conventional fractionation is performed. The Calypso System provides a daily transponder geometry check to enable this evaluation. Due to geometry changes, a new CT and treatment planning procedure can be necessary not only to customize the irradiation fields to the tumor but also for an update of transponder positions relative to the tumor. To be aware of these changes, a weekly CT scan can be recommended.

For our data on shrinkage of the beacon triangle, no data on simultaneously changes in GTV volume is available. But it can be assumed that the GTVs are shrinking, too, like described in the aforementioned studies (Kupelian et al., 2005; Britton et al., 2007). It is not clear if this data allows for an early estimation of the benefit, the patient got through the radiotherapy, during the course of treatment. Although the change in tumor volume is a standard measure to quantify therapy response in general, see e.g. (Eisenhauer et al., 2009), it is not necessarily correlated to a longer overall survival time. For example, no correlation between tumor shrinkage during chemotherapy assessed with repeated CT data sets and the overall survival can be found for NSCLC patients (Knollmann et al., 2014). For radiotherapy it is shown that the metabolic information of the treated tumor provided by PET imaging is superior to the pure morphological information in the CT data set in predicting the survival time of NSCLC patients in follow up care (Manus et al., 2003).

One possible side effect due to irradiation of healthy lung tissue is a pneumonitis, which can lead to a persistent lung fibrosis, see e.g. (Sauer, 2010). A lung fibrosis is characterized by the exchange of normal lung tissue by fibrotic tissue (like scarred tissue) which is less elastic and not able to provide for the gas exchange and is thereby a very serious late side effect. The standard deviations of the transponder distances show no trend with time, thus no statement about early changes in lung tissue elasticity because of side effects over the course of treatment can be made.

4.4.3 Correlation between internal and external motion

For two of the three regarded patients a strong correlation between one coordinate of the internal transponder centroid motion and the changes in chest circumference can be found. This is the vertical coordinate for patient 5 and the longitudinal one for patient 6. The best mean correlation coefficients per motion direction are accompanied with a time shift between the internal and external signal. This time shift range from -0.6 s to 1.4 s. These

time shifts are too large to be caused by the different beam status detection and sample rates of the two motion detection systems. An anatomical or physiological reason seems to be probable as other publications report on the same effect with different motion detection methods. (Tsunashima et al., 2004) reports on time shifts of up to 1 s for a laser surface scanner as external breathing motion indicator and fluoroscopic images acquired after the patient setup in a study with 32 patients suffering from tumors in lung, liver or esophagus. (Korreman et al., 2006) analyzed the correlation of internal fiducial markers detected with 19 cine fluoroscopies in seven lung patients acquired over 40 s each and the motion of a box with infrared markers on the patient's abdomen. They report on time shifts up to 1.9 s. Their best correlation coefficients lie between 0.49 and 0.99, the norm of the best single fraction correlation coefficients in the current analysis is similar with values between 0.56 and 0.94.

Even if the best mean correlation is strong, this correlation varies intrafractional and interfractional as shown here and demonstrated in (Ionascu et al., 2007). Because of that, a frequent update of the correlation model has to be performed if the external signal shall be used for motion management like proposed e.g. by (Wu et al., 2008) for gating or integrated in the CyberKnife system for tracking, see (Sayeh et al., 2007). If infrared markers on the patient's skin are used, the stability of internal/external correlation can also be increased by the use of a combined signal from multiple markers, see (Yan et al., 2006).

The correlation has shown to be stronger for larger internal motion amplitudes. This can be explained by the problem of low signal to noise ratio of the Calypso signal for small amplitudes. In these cases, the respiratory induced motion is not dominant enough to drive the correlation analysis, as presented for fluoroscopic signals by (Ionascu et al., 2007).

5 Conclusions

In this thesis, investigations on inter- and intrafractional motion of prostate and lung cancer patients during radiotherapy were made. The used patient data was collected during two clinical trials performed at dkfz. For all 32 patients, real-time motion data of implanted passive resonant circuits was detected continuously during the treatment with an electromagnetic tumor tracking system, the Calypso System by Varian Medical Systems Inc. Based on this motion data, different evaluations were performed. For both tumor sites the overall motion amount and motion pattern characteristics were studied, while the other evaluations were diverse. The analysis of the prostate data focused on the arising consequences I) for margin concepts, if MV CBCTs are used for patient positioning and no intrafraction motion management is available and II) for the delivered dose distributions in the individual patients studied here. For the new application of electromagnetic tracking in lung radiotherapy, which has not been studied before, evaluations were made to assess inter- and intrafractional changes of the geometry of implanted transponders, which can compromise the use of the transponder centroid motion as tumor motion surrogate. Additionally, a correlation analysis between transponder centroid motion and chest motion was done for three lung cancer patients, because chest motion is often used as external surrogate for lung tumor motion in gated radiotherapy.

Prostate

Derived margins for compensation of the combination of MV CBCT based patient setup and intrafraction motion for treatment fractions lasting for 9 min ranges from 7 mm to 9 mm dependent on the image registration strategy. However, these margins would have to be enlarged for clinical application due to other uncertainties. A thereby enlarged irradiated volume of organs at risk with high prescription doses up to 80 Gy, desired in modern prostate radiotherapy, will increase the probability of severe side effects and therefore these margins are not clinically applicable.

Evaluating the dosimetric consequences of intrafraction motion for individual patients with the experimentally validated 4D dose accumulation method based on motion dependent target points, large dose perturbations in single fractions can be found. Due to averaging effects, a remarkable dosimetric consequence on the clinical target volume for the whole treatment course is determined for one patient, only. The irradiation concept was thereby an integrated boost irradiation, which results in an inner high dose region (boost volume) with a lower dose margin of 7 mm. This margin seems to be sufficient for 20 of 21 patients to compensate for intrafraction motion, but the additional uncertainties from interfraction motion was not accounted for during the dose reconstruction.

These investigations lead to the conclusion, that an adaptive approach for motion management in prostate radiotherapy is necessary in particular, when a hypofractionated therapy is performed meaning less fractions with higher single fraction doses, as discussed for prostate due to radiobiological reasons. The aim of adaptive motion management is the reaction on motion information acquired during the irradiation, enabling the reduction of margin sizes without compromising the dose delivered to the tumor. Different methods of adaptive radiotherapy are very diverse in effort regarding both technical equipment and additional time for preparation, the treatment procedure itself and quality assurance. The simplest way would be a repeated positioning procedure using image guidance during the therapy to enable the compensation of prostate drifts. If real-time motion data is available, a threshold based repositioning can be applied in combination with a gating like approach, where the beam is disabled, when one of the characteristic prostate spikes is occurring. Good correlations between the mean prostate displacement and the deviations in all dosimetric endpoints studied here give rise to the assumption that these motion management procedures will reduce the dose effects remarkable. More complex methods of couch or MLC based prostate tracking may also considerably reduce these dose perturbations as was demonstrated experimentally, see (Menten et al., 2012; Pommer et al., 2013).

Lung

In general there are two motion components of lung tumors, the periodic breathing motion around a mean position (called midline) and the change of this midline over time. The lung cancer patients studied here show intrafractional midline motion of the same size as the breathing amplitude. This intrafractional midline motion compromises the use of margins based on the motion information in the 4D CT, because it means that the mean tumor position around which the margin is defined is not stable over time. As the midline motion is not necessarily periodic or predictable prior to the fraction, a real-time motion monitoring enabling patient specific motion management seems to be essential.

The analysis of transponder centroid motion during adjacent time intervals shows that the quality of motion prediction, required for tumor tracking systems with long latency time between motion detection and actual reaction on it, will highly depend on the single patient. In these cases it can be of advantage to perform a less complex tracking, like a tracking of the midline position, while the periodic breathing motion is taken into account by a margin.

Considering the results on the intra- and interfractional variations in transponder geometry (e.g. SDs of the intrafractional longitudinal inter-transponder distances of up to 3 mm), two recommendations for transponder implantation can be given from our data. First they should be arranged around the tumor regularly to ensure best representation of tumor position and second, they should be as close together as possible to reduce the probability of large intrafractional variations. Looking at interfractional changes, a continuous shrinkage of the spanned transponder triangle can be observed. Together with the finding that the corresponding inter-transponder distances are shrinking differently and some are even growing, a monitoring of the internal geometry both between transponders and between transponder centroid and tumor should be performed on a regular basis, for example by acquiring a weekly CT scan.

The correlation analysis between beacon centroid motion and changes in chest circumference leads to three findings that have to be considered, when the external signal is used as tumor surrogate motion in motion management. First, there are phase shifts between the internal and the external signal, second, the correlation slightly changes from fraction to fraction and third, even during one fraction the external/internal correlation changes. This lead to the conclusion, that a procedure of frequent control and if required an adaption of the used correlation model should be established.

Bibliography

Adamson, J., Wu, Q., and Yan, D. (2011). Dosimetric effect of intrafraction motion and residual setup error for hypofractionated prostate intensity-modulated radiotherapy with online cone beam computed tomography image guidance. *Int J Radiat Oncol Biol Phys*, 80(2):453–461.

Ahnesjö, A., Andreo, P., and Brahme, A. (1987). Calculation and application of point spread functions for treatment planning with high energy photon beams. *Acta Oncol*, 26(1):49–56.

Ahnesjö, A., Saxner, M., and Trepp, A. (1992). A pencil beam model for photon dose calculation. *Med Phys*, 19(2):263–273.

Ahnesjö, A. and Trepp, A. (1991). Acquisition of the effective lateral energy fluence distribution for photon beam dose calculations by convolution models. *Phys Med Biol*, 36(7):973–985.

Ballhausen, H., Reiner, M., Kantz, S., Belka, C., and Söhn, M. (2013). The random walk model of intrafraction movement. *Phys Med Biol*, 58(7):2413–2427.

Balter, J. M., Wright, J. N., Newell, L. J., Friemel, B., Dimmer, S., Cheng, Y., Wong, J., Vertatschitsch, E., and Mate, T. P. (2005). Accuracy of a wireless localization system for radiotherapy. *Int J Radiat Oncol Biol Phys*, 61(3):933–937.

Barrett, A., Dobbs, J., Morris, S., and Roques, T. (2009). *Practical Radiotherapy Planning*. Hodder Arnold, London, 4th edition.

Beckham, W. A., Keall, P. J., and Siebers, J. V. (2002). A fluence-convolution method to calculate radiation therapy dose distributions that incorporate random set-up error. *Phys Med Biol*, 47(19):3465–3473.

Beltran, C., Herman, M. G., and Davis, B. J. (2008). Planning target margin calculations for prostate radiotherapy based on intrafraction and interfraction motion using four localization methods. *Int J Radiat Oncol Biol Phys*, 70(1):289–295.

Berbeco, R. I., Hacker, F., Ionascu, D., and Mamon, H. J. (2007). Clinical Feasibility of Using an EPID in cine Mode for Image–Guided Verification of Stereotactic Body Radiotherapy. *Int J Radiat Oncol Biol Phys*, 69(1):258–266.

Berbeco, R. I., Jiang, S. B., Sharp, G. C., Chen, G. T. Y., Mostafavi, H., and Shirato, H. (2004). Integrated radiotherapy imaging system (IRIS): design considerations of tumour tracking with linac gantry-mounted diagnostic x-ray systems with flat-panel detectors. *Phys Med Biol*, 49(2):243–255.

Birkner, M., Yan, D., Alber, M., Liang, J., and Nüsslin, F. (2003). Adapting inverse planning to patient and organ geometrical variation: algorithm and implementation. *Med Phys*, 30(10):2822–2831.

Bissonnette, J.-P., Franks, K. N., Purdie, T. G., Moseley, D. J., Sonke, J.-J., Jaffray, D. A., Dawson, L. A., and Bezjak, A. (2009). Quantifying interfraction and intrafraction tumor motion in lung stereotactic body radiotherapy using respiration-correlated cone beam computed tomography. *Int J Radiat Oncol Biol Phys*, 75(3):688–695.

Bortfeld, T. (2006). IMRT: a review and preview. *Phys Med Biol*, 51(13):363–379.

Bortfeld, T., Jokivarsi, K., Goitein, M., Kung, J., and Jiang, S. B. (2002). Effects of intra-fraction motion on IMRT dose delivery: statistical analysis and simulation. *Phys Med Biol*, 47(13):2203–2220.

Bortfeld, T., Schlegel, W., and Rhein, B. (1993). Decomposition of pencil beam kernels for fast dose calculations in three-dimensional treatment planning. *Med Phys*, 20(2):311–318.

Bortfeld, T. and Thieke, C. (2006). Optimization of Treatment Plans, Inverse Planning. In Schlegel, W., Bortfeld, T., and Grosu, A.-L., editors, *New Technologies in Radiation Oncology*. Springer, Berlin, Heidelberg.

Britton, K. R., Starkschall, G., Tucker, S. L., Pan, T., Nelson, C., Chang, J. Y., Cox, J. D., Mohan, R., and Komaki, R. (2007). Assessment of gross tumor volume regression and motion changes during radiotherapy for non–small–cell lung cancer as measured by four-dimensional computed tomography. *Int J Radiat Oncol Biol Phys*, 68(4):1036–1046.

Calypso Medical Technologies, Inc. (2010a). *Calypso 4D Localization System - User's Manual*. Version 2.0, LBL0008-005 Rev A.

Calypso Medical Technologies, Inc. (2010b). *Investigator's Brochure - Anchored Beacon Electromagnetic Transponders*. Rev. 04 – (2011–01–06).

Chetty, I. J., Curran, B., Cygler, J. E., DeMarco, J. J., Ezzell, G., Faddegon, B. A., Kawrakow, I., Keall, P. J., Liu, H., Ma, C. M. C., Rogers, D. W. O., Seuntjens, J., Sheikh-Bagheri, D., and Siebers, J. V. (2007). Report of the AAPM Task Group No. 105: Issues associated with clinical implementation of Monte Carlo-based photon and electron external beam treatment planning. *Med Phys*, 34(12):4818–4853.

Chow, J. C. L. and Jiang, R. (2013). Prostate volumetric-modulated arc therapy: dosimetry and radiobiological model variation between the single-arc and double-arc technique. *J Appl Clin Med Phys*, 14(3):4053–4062.

Craig, T., Battista, J., and Dyk, J. V. (2003a). Limitations of a convolution method for modeling geometric uncertainties in radiation therapy. I. The effect of shift invariance. *Med Phys*, 30(8):2001–2011.

Craig, T., Battista, J., and Dyk, J. V. (2003b). Limitations of a convolution method for modeling geometric uncertainties in radiation therapy. II. The effect of a finite number of fractions. *Med Phys*, 30(8):2012–2020.

Curtis, W., Khan, M., Magnelli, A., Stephans, K., Tendulkar, R., and Xia, P. (2013). Relationship of Imaging Frequency and Planning Margin to Account for Intrafraction Prostate Motion: Analysis Based on Real–Time Monitoring Data. *Int J Radiat Oncol Biol Phys*, 85(3):700–706.

Dearnaley, D. P., Hall, E., Lawrence, D., Huddart, R. A., Eeles, R., Nutting, C. M., Gadd, J., Warrington, A., Bidmead, M., and Horwich, A. (2005). Phase III pilot study of dose escalation using conformal radiotherapy in prostate cancer: PSA control and side effects. *Br J Cancer*, 92(3):488–498.

Depuydt, T., Van Esch, A., and Huyskens, D. P. (2002). A quantitative evaluation of IMRT dose distributions: refinement and clinical assessment of the gamma evaluation. *Radiother Oncol*, 62(3):309–319.

Eisenhauer, E. A., Therasse, P., Bogaerts, J., Schwartz, L. H., Sargent, D., Ford, R., Dancey, J., Arbuck, S., Gwyther, S., Mooney, M., Rubinstein, L., Shankar, L., Dodd, L., Kaplan, R., Lacombe, D., and Verweij, J. (2009). New response evaluation criteria in solid tumours: Revised RECIST guideline (version 1.1). *European J Cancer*, 45(2):228–247.

Engelsman, M., Damen, E. M. F., De Jaeger, K., van Ingen, K. M., and Mijnheer, B. J. (2001). The effect of breathing and set-up errors on the cumulative dose to a lung tumor. *Radiother Oncol*, 60(1):95–105.

Faddegon, B., Egley, B., and Steinberg, T. (2004). Comparison of beam characteristics of a gold x-ray target and a tungsten replacement target. *Med Phys*, 31(1):91–97.

Fallone, B. G., Murray, B., Rathee, S., Stanescu, T., Steciw, S., Vidakovic, S., Blosser, E., and Tymofichuk, D. (2009). First MR images obtained during megavoltage photon irradiation from a prototype integrated linac-MR system. *Med Phys*, 36(6):2084–2088.

Fippel, M. (2006). Monte Carlo Dose Calculation for Treatment Planning. In Schlegel, W., Bortfeld, T., and Grosu, A.-L., editors, *New Technologies in Radiation Oncology*. Springer, Berlin, Heidelberg.

Franz, A. M., Schmitt, D., Seitel, A., Chatrasingh, M., Echner, G., Oelfke, U., Nill, S., Birkfellner, W., and Maier-Hein, L. (2014). Standardized accuracy assessment of the Calypso wireless transponder tracking system. *Phys Med Biol*. accepted for publication.

Fu, D. and Kuduvalli, G. (2008). A fast, accurate, and automatic 2D–3D image registration for image–guided cranial radiosurgery. *Med Phys*, 35(5):2180–2194.

Guckenberger, M., Wilbert, J., Meyer, J., Baier, K., Richter, A., and Flentje, M. (2007). Is a single respiratory correlated 4D-CT study sufficient for evaluation of breathing motion? *Int J Radiat Oncol Biol Phys*, 67(5):1352–1359.

Hanley, J., Debois, M. M., Mah, D., Mageras, G. S., Raben, A., Rosenzweig, K., Mychalczak, B., Schwartz, L. H., Gloeggler, P. J., Lutz, W., Ling, C. C., Leibel, S. A., Fuks, Z., and Kutcher, G. J. (1999). Deep inspiration breath-hold technique for lung tumors: the potential value of target immobilization and reduced lung density in dose escalation. *Int J Radiat Oncol Biol Phys*, 45(3):603–611.

Hansen, E. K. and Roach III, M., editors (2010). *Handbook of Evidence–Based Radiation Oncology*. Springer Science+Business Media, New York, Heidelberg, Dordrecht, London, second edition.

Heath, E., Unkelbach, J., and Oelfke, U. (2009). Incorporating uncertainties in respiratory motion into 4D treatment plan optimization. *Med Phys*, 36(7):3059–3071.

Hsu, A., Miller, N. R., Evans, P. M., Bamber, J. C., and Webb, S. (2005). Feasibility of using ultrasound for real-time tracking during radiotherapy. *Med Phys*, 32(6):1500–1512.

Huang, E., Dong, L., Chandra, A., Kuban, D. A., Rosen, I. I., Evans, A., and Pollack, A. (2002). Intrafraction prostate motion during IMRT for prostate cancer. *Int J Radiat Oncol Biol Phys*, 53(2):261–268.

Hurkmans, C. W., Remeijer, P., Lebesque, J. V., and Mijnheer, B. J. (2001). Set–up verification using portal imaging; review of current clinical practice. *Radiother Oncol*, 58(2):105–120.

ICRU (1993). Prescribing, Recording, and Reporting Photon Beam Therapy. Technical report, International Commission on Radiation Units and Measurements, Bethesda. ICRU–Report 50.

ICRU (1999). Prescribing, Recording, and Reporting Photon Beam Therapy, Supplement to ICRU Report 50. Technical report, International Commission on Radiation Units and Measurements, Bethesda. ICRU–Report 62.

Imura, M., Yamazaki, K., Shirato, H., Onimaru, R., Fujino, M., Shimizu, S., Harada, T., Ogura, S., Dosaka-Akita, H., Miyasaka, K., and Nishimura, M. (2005). Insertion and fixation of fiducial markers for setup and tracking of lung tumors in radiotherapy. *Int J Radiat Oncol Biol Phys*, 63(5):1442–1447.

Ionascu, D., Jiang, S. B., Nishioka, S., Shirato, H., and Berbeco, R. I. (2007). Internal-external correlation investigations of respiratory induced motion of lung tumors. *Med Phys*, 34(10):3893–3903.

Jaffray, D. A., Siewerdsen, J. H., Wong, J. W., and Martinez, A. A. (2002). Flat-panel cone-beam computed tomography for image-guided radiation therapy. *Int J Radiat Oncol Biol Phys*, 53(5):1337–1349.

Jin, J.-Y., Yin, F.-F., Tenn, S. E., Medin, P. M., and Solberg, T. D. (2008). Use of the BrainLAB ExacTrac X-Ray 6D System in Image-Guided Radiotherapy. *Med Dosim*, 33(2):124–134.

Johnston, H., Hilts, M., Beckham, W., and Berthelet, E. (2008). 3D ultrasound for prostate localization in radiation therapy: A comparison with implanted fiducial markers. *Med Phys*, 35(6):2403–2413.

Juhler Nøttrup, T., Korreman, S. S., Pedersen, A. N., Aarup, L. R., Nyström, H., Olsen, M., and Specht, L. (2007). Intra- and interfraction breathing variations during curative radiotherapy for lung cancer. *Radiother Oncol*, 84(1):40–48.

Keall, P. J., Cattell, H., Pokhrel, D., Dieterich, S., Wong, K. H., Murphy, M. J., Vedam, S. S., Wijesooriya, K., and Mohan, R. (2006). Geometric accuracy of a real-time target tracking system with dynamic multileaf collimator tracking system. *Int J Radiat Oncol Biol Phys*, 65(5):1579–1584.

Keall, P. J., Colvill, E., O'Brien, R., Ng, J. A., Poulsen, P. R., Eade, T., Kneebone, A., and Booth, J. T. (2014). The first clinical implementation of electromagnetic transponder-guided MLC tracking. *Med Phys*, 41(2):020702–1–020702–5.

Keall, P. J., Starkschall, G., Shukla, H., Forster, K. M., Ortiz, V., Stevens, C. W., Vedam, S. S., George, R., Guerrero, T., and Mohan, R. (2004). Acquiring 4D thoracic CT scans using a multislice helical method. *Phys Med Biol*, 49(10):2053–2067.

Knollmann, F. D., Kumthekar, R., Fetzer, D., and Socinski, M. A. (2014). Assessing response to treatment in non–small-cell lung cancer: Role of tumor volume evaluated by computed tomography. *Clin Lung Cancer*, 15(2):103–109.

Kong, F.-M., Ten Haken, R. K., Schipper, M. J., Sullivan, M. A., Chen, M., Lopez, C., Kalemkerian, G. P., and Hayman, J. A. (2005). High-dose radiation improved local tumor control and overall survival in patients with inoperable/unresectable non-small-cell lung cancer: Long-term results of a radiation dose escalation study. *Int J Radiat Oncol Biol Phys*, 63(2):324–333.

Korreman, S., Mostafavi, H., Le, Q.-T., and Boyer, A. (2006). Comparison of respiratory surrogates for gated lung radiotherapy without internal fiducials. *Acta Oncol*, 45(7):935–942.

Korreman, S. S., Juhler-Nøttrup, T., and Boyer, A. L. (2008). Respiratory gated beam delivery cannot facilitate margin reduction, unless combined with respiratory correlated image guidance. *Radiother Oncol*, 86(1):61–68.

Kothary, N., Heit, J. J., Louie, J. D., Kuo, W. T., Loo Jr, B. W., Koong, A., Chang, D. T., Hovsepian, D., Sze, D. Y., and Hofmann, L. V. (2009). Safety and efficacy of percutaneous fiducial marker implantation for image-guided radiation therapy. *J Vasc Interv Radiol*, 20(2):235–239.

Kotte, A. N., Hofman, P., Lagendijk, J. J., van Vulpen, M., and van der Heide, U. A. (2007). Intrafraction motion of the prostate during external-beam radiation therapy: Analysis of 427 patients with implanted fiducial markers. *Int J Radiat Oncol Biol Phys*, 69(2):419–425.

Krauss, A., Nill, S., and Oelfke, U. (2011a). The comparative performance of four respiratory motion predictors for real-time tumour tracking. *Phys Med Biol*, 56(16):5303–5317.

Krauss, A., Nill, S., Tacke, M., and Oelfke, U. (2011b). Electromagnetic real-time tumor position monitoring and dynamic multileaf collimator tracking using a siemens 160 MLC: geometric and dosimetric accuracy of an integrated system. *Int J Radiat Oncol Biol Phys*, 79(2):579–587.

Kupelian, P., Willoughby, T., Mahadevan, A., Djemil, T., Weinstein, G., Jani, S., Enke, C., Solberg, T., Flores, N., Liu, D., Beyer, D., and Levine, L. (2007). Multi-institutional clinical experience with the calypso system in localization and continuous, real-time monitoring of the prostate gland during external radiotherapy. *Int J Radiat Oncol Biol Phys*, 67(4):1088–1098.

Kupelian, P. A., Ramsey, C., Meeks, S. L., Willoughby, T. R., Forbes, A., Wagner, T. H., and Langen, K. M. (2005). Serial megavoltage CT imaging during external beam radiotherapy for non–small–cell lung cancer: Observations on tumor regression during treatment. *Int J Radiat Oncol Biol Phys*, 63(4):1024–1028.

Lagendijk, J. J., Raaymakers, B. W., Raaijmakers, A. J., Overweg, J., Brown, K. J., Kerkhof, E. M., van der Put, R. W., Hårdemark, B., van Vulpen, M., and van der Heide, U. A. (2008). MRI/linac integration. *Radiother Oncol*, 86(1):25–29.

Langen, K. M., Chauhan, B., Siebers, J. V., Moore, J., and Kupelian, P. A. (2012). The dosimetric effect of intrafraction prostate motion on step-and-shoot intensity-modulated radiation therapy plans: Magnitude, correlation with motion parameters, and comparison with helical tomotherapy plans. *Int J Radiat Oncol Biol Phys*, 84(5):1220–1225.

Langen, K. M., Lu, W., Ngwa, W., Willoughby, T. R., Chauhan, B., Meeks, S. L., Kupelian, P. A., and Olivera, G. (2008a). Correlation between dosimetric effect and intrafraction motion during prostate treatments delivered with helical tomotherapy. *Phys Med Biol*, 53(24):7073–7086.

Langen, K. M., Lu, W., Willoughby, T. R., Chauhan, B., Meeks, S. L., Kupelian, P. A., and Olivera, G. (2009). Dosimetric effect of prostate motion during helical tomotherapy. *Int J Radiat Oncol Biol Phys*, 74(4):1134–1142.

Langen, K. M., Willoughby, T. R., Meeks, S. L., Santhanam, A., Cunningham, A., Levine, L., and Kupelian, P. A. (2008b). Observations on real-time prostate gland motion using electromagnetic tracking. *Int J Radiat Oncol Biol Phys*, 71(4):1084–1090.

Langen, K. M., Zhang, Y., Andrews, R. D., Hurley, M. E., Meeks, S. L., Poole, D. O., Willoughby, T. R., and Kupelian, P. A. (2005). Initial experience with megavoltage (MV) CT guidance for daily prostate alignments. *Int J Radiat Oncol Biol Phys*, 62(5):1517–1524.

Lattanzi, J., McNeeley, S., Donnelly, S., Palacio, E., Hanlon, A., Schultheiss, T. E., and Hanks, G. E. (2000). Ultrasound-based stereotactic guidance in prostate Cancer–Quantification of organ motion and set-up errors in external beam radiation therapy. *Comput Aided Surg*, 5(4):289–295.

Leitlinienprogramm Onkologie (2011). Interdisziplinäre Leitlinie der Qualität S3 zur Früherkennung, Diagnose und Therapie der verschiedenen Stadien des Prostatakarzinoms. AWMF-Register-Nummer (034-022OL), Version 2.0 - 1. Aktualisierung 2011, Kurzversion.

Li, H. S., Chetty, I. J., Enke, C. A., Foster, R. D., Willoughby, T. R., Kupellian, P. A., and Solberg, T. D. (2008a). Dosimetric consequences of intrafraction prostate motion. *Int J Radiat Oncol Biol Phys*, 71(3):801–812.

Li, H. S., Chetty, I. J., and Solberg, T. D. (2008b). Quantifying the interplay effect in prostate IMRT delivery using a convolution-based method. *Med Phys*, 35(5):1703–1710.

Li, J. G. and Xing, L. (2000). Inverse planning incorporating organ motion. *Med Phys*, 27(7):1573–1578.

Li, J. S., Lin, M.-H., Buyyounouski, M. K., Horwitz, E. M., and Ma, C.-M. (2013). Reduction of prostate intrafractional motion from shortening the treatment time. *Phys Med Biol*, 58(14):4921–4932.

Litzenberg, D. W., Balter, J. M., Hadley, S. W., Sandler, H. M., Willoughby, T. R., Kupelian, P. A., and Levine, L. (2006). Influence of intrafraction motion on margins for prostate radiotherapy. *Int J Radiat Oncol Biol Phys*, 65(2):548–553.

Löf, J., Lind, B. K., and Brahme, A. (1995). Optimal radiation beam profiles considering the stochastic process of patient positioning in fractionated radiation therapy. *Inverse Problems*, 11(6):1189–1209.

Low, D. A., Harms, W. B., Mutic, S., and Purdy, J. A. (1998). A technique for the quantitative evaluation of dose distributions. *Med Phys*, 25(5):656–661.

Lujan, A. E., Larsen, E. W., Balter, J. M., and Haken, R. K. T. (1999). A method for incorporating organ motion due to breathing into 3D dose calculations. *Med Phys*, 26(5):715–720.

Mackie, T. R., Scrimger, J. W., and Battista, J. J. (1985). A convolution method of calculating dose for 15 MV x rays. *Med Phys*, 12(2):188–196.

Madsen, B. L., Hsi, R. A., Pham, H. T., Fowler, J. F., Esagui, L., and Corman, J. (2007). Stereotactic hypofractionated accurate radiotherapy of the prostate (SHARP), 33.5 Gy in five fractions for localized disease: First clinical trial results. *Int J Radiat Oncol Biol Phys*, 67(4):1099–1105.

Maes, F., Collognon, A., Vandermeulen, D., Marchal, G., and Suetens, P. (1997). Multimodality image registration by maximization of mutual information. *IEEE Transactions on medical imaging*, 16(2):187–198.

Manus, M. P. M., Hicks, R. J., Matthews, J. P., McKenzie, A., Rischin, D., Salminen, E. K., and Ball, D. L. (2003). Positron emission tomography is superior to computed tomography scanning for response-assessment after radical radiotherapy or chemoradiotherapy in patients with non–small-cell lung cancer. *J Clin Oncol*, 21(7):1285–1292.

McCarter, S. D. and Beckham, W. A. (2000). Evaluation of the validity of a convolution method for incorporating tumour movement and set-up variations into the radiotherapy treatment planning system. *Phys Med Biol*, 45(4):923–931.

McKenzie, A. L., van Herk, M., and Mijnheer, B. (2000). The width of margins in radiotherapy treatment plans. *Phys Med Biol*, 45(11):3331–3342.

Menten, M. J., Guckenberger, M., Herrmann, C., Krauss, A., Nill, S., Oelfke, U., and Wilbert, J. (2012). Comparison of a multileaf collimator tracking system and a robotic treatment couch tracking system for organ motion compensation during radiotherapy. *Med Phys*, 39(11):7032–7041.

Mohan, R., Chui, C., and Lidofsky, L. (1986). Differential pencil beam dose computation model for photons. *Med Phys*, 13(1):64–73.

Moorrees, J. and Bezak, E. (2012). Four dimensional radiotherapy: a review of current technologies and modalities. *Australas Phys Eng Sci Med*, 35(4):399–406.

Mutanga, T. F., de Boer, H. C., van der Wielen, G. J., Hoogeman, M. S., Incrocci, L., and Heijmen, B. J. (2011). Margin evaluation in the presence of deformation, rotation, and translation in prostate and entire seminal vesicle irradiation with daily marker-based setup corrections. *Int J Radiat Oncol Biol Phys*, 81(4):1160–1167.

Nederveen, A. J., Dehnad, H., van der Heide, U. A., van Moorselaar, R. A., Hofman, P., and Lagendijk, J. J. (2003). Comparison of megavoltage position verification for prostate irradiation based on bony anatomy and implanted fiducials. *Radiother Oncol*, 68(1):81–88.

Nederveen, A. J., van der Heide, U. A., Dehnad, H., van Moorselaar, R. J. A., Hofman, P., and Lagendijk, J. J. (2002). Measurements and clinical consequences of prostate motion during a radiotherapy fraction. *Int J Radiat Oncol Biol Phys*, 53(1):206–214.

Nelson, C., Starkschall, G., and Chang, J. Y. (2006). The potential for dose escalation in lung cancer as a result of systematically reducing margins used to generate planning target volume. *Int J Radiat Oncol Biol Phys*, 65(2):573–586.

Nevinny-Stickel, M., Sweeney, R. A., Bale, R. J., Posch, A., Auberger, T., and Lukas, P. (2004). Reproducibility of Patient Positioning for Fractionated Extracranial Stereotactic Radiotherapy Using a Double-Vacuum Technique. *Strahlenther Onkol*, 180(2):117–122.

Noel, C. E., Santanam, L., Olsen, J. R., Baker, K. W., and Parikh, P. J. (2010). An automated method for adaptive radiation therapy for prostate cancer patients using continuous fiducial-based tracking. *Phys Med Biol*, 55(1):65–82.

O'Connor, J. E. (1957). The variation of scattered x-rays with density in an irradiated body. *Phys Med Biol*, 1(4):352–369.

Oertel, S., Debus, J., Hof, H., and Bischof, P. D. M. (2010). Strahlentherapie des Bronchialkarzinoms. *Radiologe*, 50(8):669–674.

Palombarini, M., Mengoli, S., Fantazzini, P., Cadioli, C., Degli Esposti, C., and Frezza, G. P. (2012). Analysis of inter-fraction setup errors and organ motion by daily kilovoltage cone beam computed tomography in intensity modulated radiotherapy of prostate cancer. *Radiat Oncol*, 7(56):56–63.

Peeters, S. T. H., Heemsbergen, W. D., Koper, P. C. M., Putten, W. L. J. v., Slot, A., Dielwart, M. F. H., Bonfrer, J. M. G., Incrocci, L., and Lebesque, J. V. (2006). Dose-response in radiotherapy for localized prostate cancer: Results of the dutch multicenter randomized phase III trial comparing 68 Gy of radiotherapy with 78 Gy. *J Clin Oncol*, 24(13):1990–1996.

Plathow, C., Ley, S., Fink, C., Puderbach, M., Hosch, W., Schmähl, A., Debus, J., and Kauczor, H.-U. (2004). Analysis of intrathoracic tumor mobility during whole breathing cycle by dynamic MRI. *Int J Radiat Oncol Biol Phys*, 59(4):952–959.

Podgorsak, E. D. and International Atomic Energy Agency (2005). *Radiation oncology physics: a handbook for teachers and students.* International Atomic Energy Agency, Vienna.

Pommer, T., Falk, M., Poulsen, P. R., Keall, P. J., O'Brien, R. T., Petersen, P. M., and Munck af Rosenschöld, P. (2013). Dosimetric benefit of DMLC tracking for conventional and sub-volume boosted prostate intensity-modulated arc radiotherapy. *Phys Med Biol*, 58(7):2349–2361.

Pouliot, J., Bani-Hashemi, A., Josephine Chen, Svatos, M., Ghelmansarai, F., Mitschke, M., Aubin, M., Xia, P., Morin, O., Bucci, K., Roach III, M., Hernandez, P., Zheng, Z., Hristov, D., and Verhey, L. (2005). Low-dose megavoltage cone-beam CT for radiation therapy. *Int J Radiat Oncol Biol Phys*, 61(2):552–560.

Poulsen, P. R., Cho, B., Langen, K., Kupelian, P., and Keall, P. J. (2008). Three-dimensional prostate position estimation with a single x-ray imager utilizing the spatial probability density. *Phys Med Biol*, 53(16):4331–4353.

Rasch, C., Steenbakkers, R., and van Herk, M. (2005). Target definition in prostate, head, and neck. *Semin Radiat Oncol*, 15(3):136–145.

Resnick, M. J., Koyama, T., Fan, K.-H., Albertsen, P. C., Goodman, M., Hamilton, A. S., Hoffman, R. M., Potosky, A. L., Stanford, J. L., Stroup, A. M., Van Horn, R. L., and Penson, D. F. (2013). Long-term functional outcomes after treatment for localized prostate cancer. *N Engl J Med*, 368(5):436–445.

Rhein, B., Häring, P., Debus, J., and Schlegel, W. (2002). Dosimetrische Verifikation von IMRT-Gesamtplänen am Deutschen Krebsforschungszentrum Heidelberg. *Z Med Phys*, 12:122–132.

Ritter, M., Forman, J., Kupelian, P., Lawton, C., and Petereit, D. (2009). Hypofractionation for prostate cancer. *Cancer J*, 15(1):1–6.

Robert-Koch-Institut (Hrsg) und die Gesellschaft der epidemiologischen Krebsregister in Deutschland e.V. (Hrsg) (2012). Krebs in Deutschland 2007/2008. 8. Ausgabe.

Roman, N. O., Shepherd, W., Mukhopadhyay, N., Hugo, G. D., and Weiss, E. (2012). Interfractional positional variability of fiducial markers and primary tumors in locally advanced non-small-cell lung cancer during audiovisual biofeedback radiotherapy. *Int J Radiat Oncol Biol Phys*, 83(5):1566–1572.

Rosenzweig, K. E., Hanley, J., Mah, D., Mageras, G., Hunt, M., Toner, S., Burman, C., Ling, C., Mychalczak, B., Fuks, Z., and Leibel, S. A. (2000). The deep inspiration breath–hold technique in the treatment of inoperable non–small–cell lung cancer. *Int J Radiat Oncol Biol Phys*, 48(1):81–87.

Rottmann, J., Aristophanous, M., Chen, A., Court, L., and Berbeco, R. (2010). A multi-region algorithm for markerless beam's-eye view lung tumor tracking. *Phys Med Biol*, 55(18):5585–5598.

Sandler, H. M., Liu, P.-Y., Dunn, R. L., Khan, D. C., Tropper, S. E., Sanda, M. G., and Mantz, C. A. (2010). Reduction in patient-reported acute morbidity in prostate cancer patients treated with 81-Gy intensity-modulated radiotherapy using reduced planning target volume margins and electromagnetic tracking: Assessing the impact of margin reduction study. *Urology*, 75(5):1004–1008.

Sauer, R. (2010). *Strahlentherapie und Onkologie*. Elsevier, Urban & Fischer, München. 5. Auflage.

Sayeh, S., Wang, J., Main, W. T., Kilby, W., and Maurer, Jr., C. R. (2007). Respiratory motion tracking for robotic radiosurgery. In Urschel, H. C., Kresl, J. J., Luketich, J. D., Papiez, L., and Timmerman, R. D., editors, *Robotic Radiosurgery. Treating Tumors that Move with Respiration*. Springer, Berlin, Heidelberg, New York.

Schmidt, M. L., Hoffmann, L., Kandi, M., Møller, D. S., and Poulsen, P. R. (2013). Dosimetric impact of respiratory motion, interfraction baseline shifts, and anatomical changes in radiotherapy of non-small cell lung cancer. *Acta Oncol*, 52(7):1490–1496.

Schmitt, D., Nill, S., Herfarth, K., Münter, M., Pfitzenmaier, J., Zabel-du Bois, A., Röder, F., Huber, P., and Oelfke, U. (2010a). Assessment of IGRT strategies for prostate patient setup and the impact of intrafraction motion. *Radiother Oncol*, 96:452.

Schmitt, D., Nill, S., Herfarth, K., Münter, M., Pfitzenmaier, J., Zabel-du Bois, A., Röder, F., Huber, P., and Oelfke, U. (2010b). Intrafraction organ motion during prostate radiotherapy: Quantitative correlation of treatment time and margin size. *Int J Radiat Oncol Biol Phys*, 78(3):752.

Schmitt, D., Nill, S., Röder, F., Gompelmann, D., Herth, F., and Oelfke, U. (2013a). Inter- and intrafractional changes in the geometry of implanted electromagnetic transponders in the upper lung. In *Abstractband der 44. Jahrestagung der DGMP*, pages 115–118.

Schmitt, D., Nill, S., Röder, F., Herfarth, K., and Oelfke, U. (2012a). Dosimetric consequences of intrafraction prostate motion: Comparison between phantom measurements and three different calculation methods. *Med Phys*, 39(6):3686.

Schmitt, D., Nill, S., Röder, F., Herfarth, K., and Oelfke, U. (2012b). Dosimetrische Auswirkungen intrafraktioneller Prostatabewegung: Berechnung und Evaluation von Dosisverteilungen in bewegten Patientengeometrien. In *Abstractband der 43. Jahrestagung der DGMP*, pages 356–357.

Schmitt, D., Nill, S., Röder, F., Herth, F., and Oelfke, U. (2013b). Quantification of intrafractional tumor motion in the upper lung using an electromagnetic tumor tracking system. *Med Phys*, 40(6):412.

Seppenwoolde, Y., Shirato, H., Kitamura, K., Shimizu, S., van Herk, M., Lebesque, J. V., and Miyasaka, K. (2002). Precise and real-time measurement of 3D tumor motion in lung due to breathing and heartbeat, measured during radiotherapy. *Int J Radiat Oncol Biol Phys*, 53(4):822–834.

Shah, A. P., Kupelian, P. A., Waghorn, B. J., Willoughby, T. R., Rineer, J. M., Mañon, R. R., Vollenweider, M. A., and Meeks, S. L. (2013). Real-time tumor tracking in the lung using an electromagnetic tracking system. *Int J Radiat Oncol Biol Phys*, 86(3):477–483.

Shah, A. P., Kupelian, P. A., Willoughby, T. R., Langen, K. M., and Meeks, S. L. (2011a). An evaluation of intrafraction motion of the prostate in the prone and supine positions using electromagnetic tracking. *Radiother Oncol*, 99(1):37–43.

Shah, A. P., Kupelian, P. A., Willoughby, T. R., and Meeks, S. L. (2011b). Expanding the use of real-time electromagnetic tracking in radiation oncology. *J Appl Clin Med Phys*, 12(4):3590–3615.

Sheikh-Bagheri, D. and Rogers, D. W. O. (2002). Monte Carlo calculation of nine megavoltage photon beam spectra using the BEAM code. *Med Phys*, 29(3):391–402.

Shirato, H., Harada, T., Harabayashi, T., Hida, K., Endo, H., Kitamura, K., Onimaru, R., Yamazaki, K., Kurauchi, N., Shimizu, T., Shinohara, N., Matsushita, M., Dosaka-Akita, H., and Miyasaka, K. (2003). Feasibility of insertion/implantation of 2.0-mm-diameter gold internal fiducial markers for precise setup and real-time tumor tracking in radiotherapy. *Int J Radiat Oncol Biol Phys*, 56(1):240–247.

Shirato, H., Suzuki, K., Sharp, G. C., Fujita, K., Onimaru, R., Fujino, M., Kato, N., Osaka, Y., Kinoshita, R., Taguchi, H., Onodera, S., and Miyasaka, K. (2006). Speed and amplitude of lung tumor motion precisely detected in four-dimensional setup and in real-time tumor-tracking radiotherapy. *Int J Radiat Oncol Biol Phys*, 64(4):1229–1236.

Siggel, M. (2008). Entwicklung einer schnellen Dosisberechnung auf Basis eines Pencil-Kernel Algorithmus für die Strahlentherapie mit Photonen. Diplomarbeit, Ruprecht-Karls-Universität Heidelberg.

Siggel, M. (2012). Concepts for the efficient Monte Carlo-based treatment plan optimization in radiotherapy. Doktorarbeit, Ruprecht-Karls-Universität Heidelberg.

Smith, R. L., Yang, D., Lee, A., Mayse, M. L., Low, D. A., and Parikh, P. J. (2011). The correlation of tissue motion within the lung: implications on fiducial based treatments. *Med Phys*, 38(11):5992–5997.

Smitsmans, M. H., Pos, F. J., de Bois, J., Heemsbergen, W. D., Sonke, J.-J., Lebesque, J. V., and van Herk, M. (2008). The Influence of a Dietary Protocol on Cone Beam CT–Guided Radiotherapy for Prostate Cancer Patients. *Int J Radiat Oncol Biol Phys*, 71(4):1279–1286.

Sonke, J.-J., Lebesque, J., and van Herk, M. (2008). Variability of four-dimensional computed tomography patient models. *Int J Radiat Oncol Biol Phys*, 70(2):590–598.

Stevens, C. W., Munden, R. F., Forster, K. M., Kelly, J. F., Liao, Z., Starkschall, G., Tucker, S., and Komaki, R. (2001). Respiratory-driven lung tumor motion is independent of tumor size, tumor location, and pulmonary function. *Int J Radiat Oncol Biol Phys*, 51(1):62–68.

Tanyi, J. A., He, T., Summers, P. A., Mburu, R. G., Kato, C. M., Rhodes, S. M., Hung, A. Y., and Fuss, M. (2010). Assessment of planning target volume margins for intensity-modulated radiotherapy of the prostate gland: Role of daily inter- and intrafraction motion. *Int J Radiat Oncol Biol Phys*, 78(5):1579–1585.

Tehrani, J. N., O'Brien, R. T., Poulsen, P. R., and Keall, P. (2013). Real-time estimation of prostate tumor rotation and translation with a kV imaging system based on an iterative closest point algorithm. *Phys Med Biol*, 58(23):8517–8533.

Thongphiew, D., Wu, Q. J., Lee, W. R., Chankong, V., Yoo, S., McMahon, R., and Yin, F.-F. (2009). Comparison of online IGRT techniques for prostate IMRT treatment: Adaptive vs repositioning correction. *Med Phys*, 36(5):1651–1662.

Tryggestad, E., Christian, M., Ford, E., Kut, C., Le, Y., Sanguineti, G., Song, D. Y., and Kleinberg, L. (2011). Inter– and Intrafraction Patient Positioning Uncertainties for Intracranial Radiotherapy: A Study of Four Frameless, Thermoplastic Mask-Based Immobilization Strategies Using Daily Cone-Beam CT. *Int J Radiat Oncol Biol Phys*, 80(1):281–290.

Tsunashima, Y., Sakae, T., Shioyama, Y., Kagei, K., Terunuma, T., Nohtomi, A., and Akine, Y. (2004). Correlation between the respiratory waveform measured using a respiratory sensor and 3D tumor motion in gated radiotherapy. *Int J Radiat Oncol Biol Phys*, 60(3):951–958.

Unkelbach, J. and Oelfke, U. (2004). Inclusion of organ movements in IMRT treatment planning via inverse planning based on probability distributions. *Phys Med Biol*, 49(17):4005–4029.

Unkelbach, J. and Oelfke, U. (2005). Incorporating organ movements in inverse planning: assessing dose uncertainties by bayesian inference. *Phys Med Biol*, 50(1):121–139.

Van de Steene, J., Linthout, N., de Mey, J., Vinh-Hung, V., Claassens, C., Noppen, M., Bel, A., and Storme, G. (2002). Definition of gross tumor volume in lung cancer: inter-observer variability. *Radiother Oncol*, 62(1):37–49.

van der Voort van Zyp, N. C., Hoogeman, M. S., van de Water, S., Levendag, P. C., van der Holt, B., Heijmen, B. J. M., and Nuyttens, J. J. (2011). Stability of markers used for real-time tumor tracking after percutaneous intrapulmonary placement. *Int J Radiat Oncol Biol Phys*, 81(3):e75–e81.

van der Wielen, G. J., Mutanga, T. F., Incrocci, L., Kirkels, W. J., Vasquez Osorio, E. M., Hoogeman, M. S., Heijmen, B. J., and de Boer, H. C. (2008). Deformation of prostate and seminal vesicles relative to intraprostatic fiducial markers. *Int J Radiat Oncol Biol Phys*, 72(5):1604–1611.

van Herk, M. (2004). Errors and Margins in Radiotherapy. *Semin Radiat Oncol*, 14(1):52–64.

van Herk, M., Remeijer, P., Rasch, C., and Lebesque, J. V. (2000). The probability of correct target dosage: dose-population histograms for deriving treatment margins in radiotherapy. *Int. J. Radiat. Oncol. Biol. Phys.*, 47(4):1121–1135.

van Sörnsen de Koste, J. R., Lagerwaard, F. J., Nijssen-Visser, M. R., Graveland, W. J., and Senan, S. (2003). Tumor location cannot predict the mobility of lung tumors: a 3D analysis of data generated from multiple CT scans. *Int J Radiat Oncol Biol Phys*, 56(2):348–354.

Vedam, S. S., Keall, P. J., Kini, V. R., Mostafavi, H., Shukla, H. P., and Mohan, R. (2003). Acquiring a four-dimensional computed tomography dataset using an external respiratory signal. *Phys Med Biol*, 48(1):45–62.

Waghorn, B. J., Shah, A. P., Ngwa, W., Meeks, S. L., Moore, J. A., Siebers, J. V., and Langen, K. M. (2010). A computational method for estimating the dosimetric effect of intra-fraction motion on step-and-shoot IMRT and compensator plans. *Phys Med Biol*, 55(14):4187–4202.

Whyte, R. I., Crownover, R., Murphy, M. J., Martin, D. P., Rice, T. W., DeCamp, Malcolm M, J., Rodebaugh, R., Weinhous, M. S., and Le, Q.-T. (2003). Stereotactic radiosurgery for lung tumors: preliminary report of a phase I trial. *Ann Thorac Surg*, 75(4):1097–1101.

Wink, N. M., Panknin, C., and Solberg, T. D. (2006). Phase versus amplitude sorting of 4D-CT data. *J Appl Clin Med Phys*, 7(1):77–85.

Witte, M. G., Geer, J. v. d., Schneider, C., Lebesque, J. V., and Herk, M. v. (2004). The effects of target size and tissue density on the minimum margin required for random errors. *Med Phys*, 31(11):3068–3079.

Wolthaus, J. W., Schneider, C., Sonke, J.-J., van Herk, M., Belderbos, J. S., Rossi, M. M., Lebesque, J. V., and Damen, E. M. (2006). Mid-ventilation CT scan construction from four-dimensional respiration-correlated CT scans for radiotherapy planning of lung cancer patients. *Int J Radiat Oncol Biol Phys*, 65(5):1560–1571.

Wolthaus, J. W. H., Sonke, J.-J., van Herk, M., and Damen, E. M. F. (2008). Reconstruction of a time-averaged midposition CT scan for radiotherapy planning of lung cancer patients using deformable registration. *Med Phys*, 35(9):3998–4011.

Wong, J. W., Sharpe, M. B., Jaffray, D. A., Kini, V. R., Robertson, J. M., Stromberg, J. S., and Martinez, A. A. (1999). The use of active breathing control (ABC) to reduce margin for breathing motion. *Int J Radiat Oncol Biol Phys*, 44(4):911–919.

Wu, H., Zhao, Q., Berbeco, R. I., Nishioka, S., Shirato, H., and Jiang, S. B. (2008). Gating based on internal/external signals with dynamic correlation updates. *Phys Med Biol*, 53(24):7137–7150.

Yan, H., Yin, F.-F., Zhu, G.-P., Ajlouni, M., and Kim, J. H. (2006). The correlation evaluation of a tumor tracking system using multiple external markers. *Med Phys*, 33(11):4073–4084.

Zhang, T., Jeraj, R., Keller, H., Lu, W., Olivera, G. H., McNutt, T. R., Mackie, T. R., and Paliwal, B. (2004). Treatment plan optimization incorporating respiratory motion. *Med Phys*, 31(6):1576–1586.

Zhu, X., Bourland, J. D., Yuan, Y., Zhuang, T., O'Daniel, J., Thongphiew, D., Wu, Q. J., Das, S. K., Yoo, S., and Yin, F. F. (2009). Tradeoffs of integrating real-time tracking into IGRT for prostate cancer treatment. *Phys Med Biol*, 54(17):N393–N401.

Danksagung

Während meiner Arbeit am dkfz wurde ich von vielen Menschen in wissenschaftlicher, organisatorischer und persönlicher Weise unterstützt. Einigen von ihnen möchte ich ganz besonders danken.

Zuallererst gilt mein Dank Prof. Uwe Oelfke, der mir die Möglichkeit gegeben hat in seiner Arbeitsgruppe diese Arbeit anzufertigen und mich immer in jeder Hinsicht unterstützt hat. Prof. Wofgang Schlegel möchte ich dafür danken, dass er in seiner Abteilung eine sehr angenehme und wissenschaftlich anregende Arbeitsathmosphäre geschaffen und eine exzellente Ausstattung zur Verfügung gestellt hat. Ausserdem bin ich sehr dankbar für die organisatorische Unterstützung der letzten Monate meiner Arbeit sowie für die Übernahme des Zweitgutachtens.

Meine experimentellen Arbeiten wären nicht möglich gewesen ohne die Unterstützung von Gernot Echner, Armin Runz und den Mitarbeitern der Feinmechanikwerkstatt. Vielen Dank für die Konstruktion und den Bau der Bewegungsplattform sowie die schnelle Hilfe bei allen mechanischen Problemen.

Für vielfältige Unterstützung am Beschleuniger und viele Einblicke in die Patientenbehandlung möchte ich mich bei Peter Häring, Bernhard Rhein, Andrea Schwahofer und Clemens Lang sowie Annette Miltner, Elisabeth Rittinghausen, Marion Bachmann und Thomas Brechter bedanken.

Ich danke Falk Röder für viele anregende Diskussionen und seine Unterstützung bei allen medizinischen Themen.

Ich möchte mich bei allen Mitgliedern unserer Arbeitsgruppe für eine sehr schöne Zeit am dkfz bedanken. Die unzähligen Kaffepausendiskussionen werden mir genauso fehlen, wie die gemeinsamen Konferenzreisen. Für ihre besondere persönliche Unterstützung und Freundschaft danke ich vorallem Georg Altenstein, Mark Bangert, Siri Jetter und Peter Ziegenhein.

Mein besonderer Dank gilt Simeon Nill, der mich über die Jahre bei allen Belangen meiner Arbeit begleitet hat. Sei es während der ungezählten Stunden am Beschleuniger oder durch viele fruchtbare Diskussionen. Du kannst wirklich „Alles, außer Hochdeutsch“.